A Model-Based Systems Engineering approach to the conceptual design of an adaptable Small Solar System Body Lander

MSc Thesis

Jorge de Francisco

Delft University of Technology

TUDelft

A Model-Based Systems Engineering approach to the conceptual design of an adaptable Small Solar System Body Lander

MSc Thesis

by

Jorge de Francisco

to obtain the degree of Master of Science
Faculty of Aerospace Engineering - Delft University of Technology

Student number:	4352726
Supervisor:	Dr. A. (Alessandra) Menicucci
Chair:	Prof. dr. E.K.A. (Eberhard) Gill
Examiner:	Dr.ir. D. (Dominic) Dirkx
Institution:	Delft University of Technology
Place:	Faculty of Aerospace Engineering, Delft

TU Delft

Preface

This thesis project is the result of many hours of work and years of studies. Its completion took discipline and commitment, with the main driver being a burning passion for space exploration. Space is home to the largest mysteries left for mankind to uncover. If this thesis project contributes meaningfully to space exploration, that on its own, would be a sufficient reward.

Firstly, I would like to thank my supervisor, Alessandra Menicucci, who always allowed me to pursue my ideas, from the overall thesis project to individual. I will miss our weekly meetings, where you always provided me with guidance on any topic I asked. I can honestly say I could not have asked for a better supervisor.

This work would not have been possible without the support, both direct and indirect, of many people; to them I owe a debt of gratitude. I would like to thank my friends for all the good times together. While there are too many to mention by name, I would like to emphasize those who stood by my side with every turn and from the very beginning of this journey: Ángel, Ankit, and Kiko. I am sure that when we look back on these times together we will remember them as some of the best in our lives.

A mis padres Vivi y Luís, quiero agradecerles todo el apoyo y amor incondicionales que me han dado durante todos estos años. Todo lo que he conseguido es gracias a vosotros y vuestros sacrificios. Sois mis modelos a seguir, y espero que siempre estéis tan orgullosos de mí como yo lo estoy de vosotros.

Lastly, I would like to especially thank my girlfriend, Nora, for her unwavering love and support. You have stood by my side every day for every step of the way for soon-to-be five amazing years, which I hope turn into many more. You are my inspiration and the reason why I strive to become a better man.

Jorge de Francisco
Delft, June 2022

Executive Summary

Small Solar System Bodies (SSSBs) are celestial objects of significant scientific and mineralogical value, with near-Earth orbiters posing a threat to our planet. Prolonged on-surface observation generates unique data, only obtainable through landing. To date, four separate landings on SSSBs have been attempted, with mixed capabilities and success. Standardization and modularity are becoming more commonplace in space missions, aiming to increase reliability and drive down costs. Due to the relative similarities in operating environment between SSSBs, a highly-adaptable lander may be able to service a large majority of these bodies with only minor adaptations. This work therefore focuses on the conceptual design of such a lander system. In order to allow for high adaptability in the design, a suitable systems engineering methodology is required. Model-based systems engineering (MBSE) was selected due to its agile and structured concept development and iteration, as well as its heritage in the MASCOT lander mission. In order to gather further knowledge on the effective operating environment of the lander, literature on SSSBs, and the approach and landing dynamics is studied and compiled. This culminates in the identification of the key enabling subsystems required for landing across a range of SSSBs: an impact dampening and a rebound suppression subsystem. These subsystems are explored further, resulting in a number of concepts being drawn up. Following the filtering of concepts based on a killer requirement, the concepts are traded-off, with the key criteria being mass, operational range and reliability, adaptability, positional assurance, and technology readiness level. The concepts are evaluated for operational range using a database with SSSB parameters, which is later used as input data for a number of trajectory dynamics simulations using the astrodynamics software toolbox Tudat. For each SSSB in the database, simulations iterate with increasing lander deployment height until a maximum is found; with the last impact velocity of the lander being recorded. The resulting data is used for the detailed design of the key enabling subsystems. The subsystem design focuses on finding a suitable, and highly adaptable, commercial-off-the-shelf solution; with different variants servicing each specific SSSB. Furthermore, the scalability of these subsystems is analyzed. Additionally, possible scientific payloads, and the subsystems required to service them, are partially defined to provide for a complete system model. This results in the complete conceptual design of a highly-adaptable SSSB lander.

Contents

Nomenclature

Abbreviations

Abbreviation	Definition
AHP	Analytical Hierarchy Process
API	Application Programming Interface
CAD	Computer-Aided Design
CDE	Constraint-driven engineering
CFRP	Carbon-fiber reinforced plastic
CI	Consistency index
CNES	National Centre for Space Studies
COTS	Commercial-off-the-shelf
CPU	Central processing unit
CR	Consistency ratio
DLR	German Aerospace Center
ECSS	European Cooperation for Space Standardization
EOL	End-of-life
EOM	Equations of motion
ESA	European Space Agency
IMU	Inertial Measurement Unit
INCOSE	International Council on Systems Engineering
IRU	Inertial Reference Unit
ISAS	Institute of Space and Astronautical Science
ISO	International Organization for Standardization
JAXA	Japan Aerospace Exploration Agency
JPL	Jet Propulsion Laboratory
MBSE	Model-based systems engineering
MBA	Main-Belt Asteroids
MDA	Model-driven architecture
MiPS	Micro Propulsion System
MSBSE	Model- and simulation-based systems engineering
NAIF	Navigation and Ancillary Information Facility
NASA	National Aeronautics and Space Administration
NEA	Near-Earth Asteroids
NEAR	Near Earth Asteroid Rendezvous
PHO	Potentially Hazardous Objects
PMI	Progress toward mission infusion
RI	Random index
SMA	Shape memory alloys
SMASSII	Small Main-belt Asteroid Spectroscopic Survey
SSSB	Small Solar System Body
SysML	Systems Modeling Language
TNO	Trans-Neptunian objects
Tudat	TU Delft Astrodynamics Toolbox
TRL	Technology Readiness Level

List of Figures

List of Tables

1

Introduction

A Small Solar System Body (SSSB) is a category of celestial objects set by the International Astronomical Union (IAU) [1]. This category includes most asteroids, comets, centaurs, trojans, and trans-Neptunian objects (TNO). SSSBs are objects of interest for both scientific and commercial applications, with 17 past missions by several space agencies dedicated to their study. While no commercial missions to SSSBs have been deployed to date, interest is growing in this area, particularly in the space mining sector [2].

For both commercial and scientific applications, on-site observation is very valuable, as it provides enhanced quality of some payload measurements; with other data only being obtainable on the surface of SSSBs [3]. For this reason, numerous missions exploring SSSBs have been either outfitted with lander modules, included a separate lander as payload, or have attempted to land as an end-of-life (EOL) manoeuvre [4][5][6][7][8][9][10]. These missions, while having achieved various levels of success, have proved the feasibility of various types of SSSB landings, and have highlighted the difficulties and challenges for landers.

As with any dedicated space mission, these missions all incur into large costs, particularly in the design and manufacturing stages. In fact, costs have been the main driver behind the cancellation, or significant reduction in scope, of some planned missions. This phenomenon extends to all space activities, particularly those with a scientific focus rather than immediate commercial applications. Therefore, there is currently a tonal shift in space design, where an emphasis is being made on standardization and modularity in order to increase reliability and drive down costs [11]. Thus, it would be of interest to the scientific community and the private sector, if these concepts could be applied to SSSB landers.

SSSB landers are prime targets for standardization and modularity, as SSSBs have relatively similar gravitational parameters; with varying surface morphologies and compositions. The lander platform should therefore be adaptable to cover a range of operating environments. Additionally, it is often the case that the target for space missions is subject to change, due to new information being uncovered, or missed launch windows. When this happens, the hardware may have to undergo significant modifications, which would be avoided or minimized if the lander was highly adaptable. Furthermore, having a standardized lander platform, independent of any space agency, would reduce the likelihood of mission cancellations due to political incidents, as was the case with ExoMars [12]. Lastly, there are a number of Potentially Hazardous Objects (PHOs), which could potentially strike Earth. Some of these PHOs, could be detected with minimal warning times between discovery and impact. If a highly adaptable platform was already designed, previous to the discovery of a PHO, it could be used as part of the impact prevention or mitigation strategies [13].

1.1. Past missions

In order to understand the challenges and existing solutions for an adaptable SSSB lander, research must be conducted on all existing missions that have been carried out. This research will aid in narrowing down the scope of the project, as well as the definition of the operational requirements. The research will be focused on SSSB landers and exclude planetary or moon landers due to the differences in their operational environment. A summary of important data from the missions studied is summarized in Table 1.1. As of today, no future lander missions to SSSBs are planned. While numerous concepts exist in the literature, the focus of this chapter is on the specific knowledge gathered by the existing probes. Concepts from literature, with no flight heritage, will be introduced in Chapter 5, where the focus will be at the subsystem level.

For the purposes of this study, a lander is defined as an independent hardware module which, being deployed from orbit, arrives to a stable and static position on a body's surface and remains on the body. This definition excludes spacecraft such as Hayabusa which touch-down on a body for a short period of time to collect samples and take-off. However, rovers such as MINERVA are included since effectively they are landers with movement capabilities. A description of each lander's hardware and their operational history is presented below in chronological order based on their launch date.

1.1.1. NEAR Shoemaker

Near Earth Asteroid Rendezvous – Shoemaker (NEAR Shoemaker) is a 487 kg spacecraft launched by the National Aeronautics and Space Administration (NASA) with the primary goal of exploring asteroid 433 Eros. NEAR Shoemaker was designed as an orbiter; however as the mission approached its final phase, NASA decided to attempt a soft landing on EROS. During descent, NEAR Shoemaker took 70 images of unprecedented resolution, with a maximum resolution of 1 centimeter in its final photograph. As NEAR Shoemaker approached the surface of Eros, it executed four braking manoeuvres which decelerated the spacecraft's vertical motion with a total ΔV = 24 m/s. Landing was completed successfully, thus achieving the first landing on an SSSB. NEAR Shoemaker operated for a period of two weeks after touchdown, where it generated high-resolution data with its gamma-ray payload, with a considerably higher resolution than all the previously generated data during orbital observations [3].

1.1.2. MINERVA

MINERVA is a rover designed and operated by the Institute of Space and Astronautical Science (ISAS), and the Japan Aerospace Exploration Agency (JAXA). It flew on-board the JAXA Hayabusa spacecraft with the objective of landing on the asteroid 25143 Itokawa after being deployed during a rehearsal landing by Hayabusa. The planned deployment would see the rover released from an altitude of 70m with a relative speed of 5 cm/s. MINERVA weighs 591 grams, and has a hexadecagonal-prism shape with a height and diameter of 100 and 120mm respectively. MINERVA is outfitted with 8 spikes on both vertical faces of the rover such that it may land on both faces without issue. For this same reason, MINERVA has solar cells attached to all its faces. These solar cells can generate enough power at 1AU to power MINERVA's CPU; however, this is not sufficient to power the actuators or radio communications, which depend on a primary battery charged by Hayabusa. The rover is able to transit through Itokawa's surface through the use of a hopping mechanism. This motion is initiated by the combination of two actuators: a turntable and a torquer. The torquer is mounted on the turntable, which is used for directional control of the torquing motion relative to the asteroid's surface. The torquer exerts a force on the turntable, where a reaction force causes the rover to hop in a ballistic motion. A picture of MINERVA and a diagram of the hopping mechanism can be seen in Figure 1.1. While the hopping speed is dependent on the friction coefficient of Itokawa's surface, the mechanism was designed to generate a maximum hopping speed of 9 cm/s [4].

MINERVA, through no fault of its own, was unfortunately a failure. As described previously, the deployment phase was intended to be conducted very close to Itokawa's surface. However, before deploy-

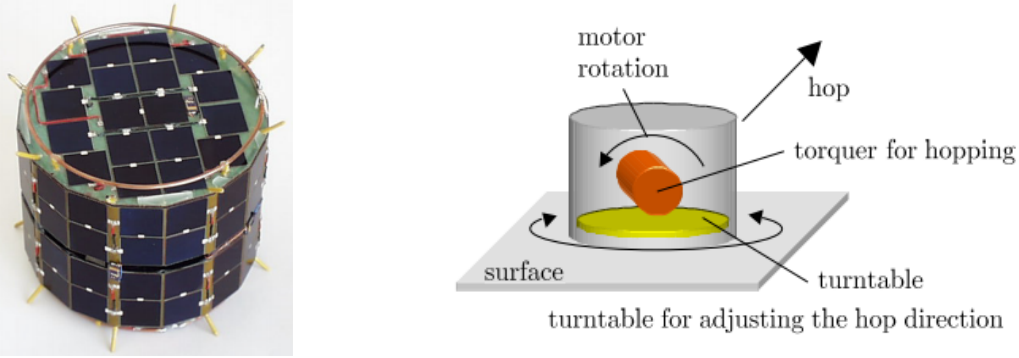

Figure 1.1: MINERVA rover (left) and turntable structure (right) (from Yoshimitsu et al. [4]).

ment, an erroneous command was sent to Hayabusa to initiate an ascent manoeuvre. This resulted in the rover being released at an altitude of 200m with a relative velocity of 15 cm/s, far exceeding the desired parameters. This resulted in MINERVA fully missing Itokawa's surface and getting launched into space where it entered a heliocentric orbit. Despite this, all systems aboard MINERVA had nominal status, with the rover managing to send a single picture of Hayabusa's solar array back to the mothership [4].

1.1.3. Philae

Philae is a lander by the European Space Agency (ESA) which flew on-board the Rosetta spacecraft and was deployed from orbit, with the mission of landing on and exploring the comet 67P/Churyumov–Gerasimenko. Philae weighs 97.9 kg, of which 26.7 kg comprise the payload; an additional 13.1 kg of deployment systems are on-board the Rosetta spacecraft, which allow the lander to be released at an adjustable speed between 0.05 and 0.52 m/s. The lander module is equipped with a single cold-gas thruster pointed towards the upwards vertical axis of the lander. This thruster was originally envisioned to accelerate the lander towards the comet; however, with a change in the target body to the more massive 67P, it was then adapted to be fired after touchdown in order to minimize the rebound. It is also equipped with a flywheel, used to stabilize Philae during descent, which provides a momentum of 6.2 Nms at a speed of 9600 rpm. Philae is a passive lander, meaning that despite being outfitted with the aforementioned hardware, no active control was exerted during the descent phase. Philae's landing gear is composed of three legs and a cardanic joint, which connects the landing gear to the main body of the lander; this allows Philae to rotate above its legs and adjust to a sloping surface. Upon landing, its kinetic energy is dissipated by a generator and converted into electric energy. Then, ice screws in each leg are drilled into the surface in order to prevent lateral sliding. Lastly, a set of two redundant harpoons attached to a tensioning motor via cables are also fired upon landing unto the surface to tether Philae to 67P's surface [5]. A schematic of Philae can be seen in Figure 1.2.

Philae's mission found mixed success; while the separation, deployment and approach phases were successful (with the corresponding scientific measurements), during touchdown both harpoons and the cold-gas thruster failed. These failures resulted in Philae entering a bouncing motion, rather than the desired tethering. Philae had repeated ground contacts for about 20 seconds, with the landing gear generator absorbing about 10% of the kinetic energy from the impact. After this, Philae hopped through 67P's surface for 2 hours, eventually coming to rest in a cavity-like environment, which hindered efforts to locate the lander and resulted in insufficient power generation. Despite these issues, Philae only suffered minimal damage and was able to carry out a large portion of its short-term scientific measurements. The largest issue was the inability to recharge the secondary batteries effectively, such that Philae had to enter hibernation, thus preemptively terminating its mission [7].

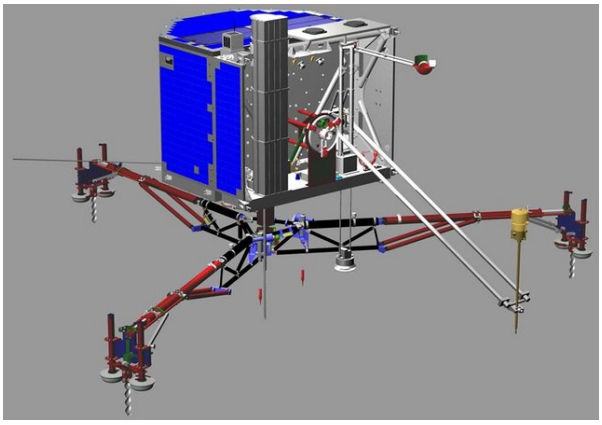

Figure 1.2: Schematic structure of Philae (from DLR Cologne [6]).

1.1.4. MINERVA-II (1 and 2)

MINERVA-II is the successor of the original MINERVA mission. Together with MASCOT, it flew on-board the Hayabusa2 mission by JAXA which targeted the exploration of 162173 Ryugu. MINERVA-II is a container package consisting of: a relay component, a helical antenna, MINERVA-II-1 and MINERVA-II-2. All the individual rovers have a mass of 1.1 kg, and share the basic construction of the original MINERVA. The main objective behind the deployment of these rovers was to demonstrate the hopping locomotion system.

MINERVA-II-1 itself contains two rovers: HIBOU and OWL; these rovers are practically identical in their construction, with slight differences in their internal sensors and thermal control systems[8]. They can be seen in Figure 1.3. The rovers use an updated hopping system based on MINERVA. The turntable was removed, thus sacrificing the control over the hopping direction to decrease the mass and volume of the subsystem [9]. The rovers were effectively deployed on the surface of Ryugu, where they became the first rovers to successfully reach the surface of an SSSB. The rover's operations involved their continuous hopping, taking pictures and temperature measurements between the hops as long as their batteries remain powered by sunlight. With the Hayabusa spacecraft leaving the orbit of Ryugu, it is unknown whether the rovers are still operational, with the last transmission received over 10 months after deployment [10].

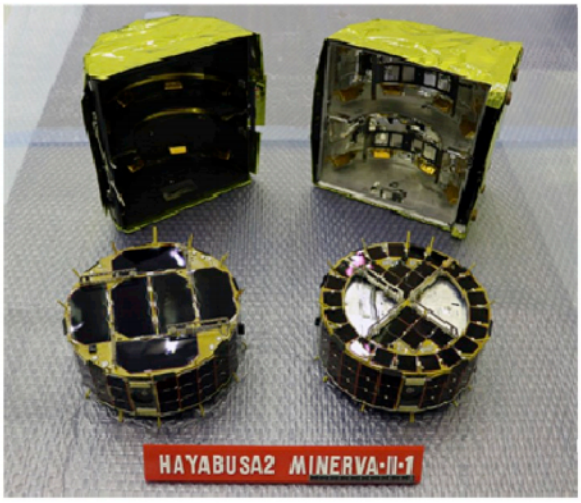

Figure 1.3: Image of the MINERVA-II-1 rovers (from JAXA [10]).

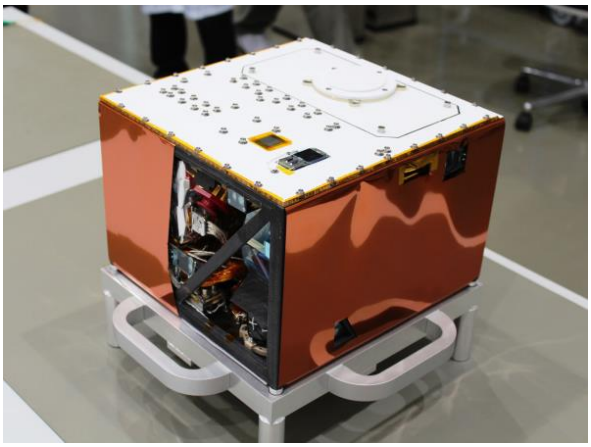

Figure 1.4: Image of the MASCOT rover (from JAXA [10]).

MINERVA-II-2, developed by a consortium of Japanese universities has a mass of 1 kg together with

its separation mechanism. it has an octagonal prim shape with spikes at its top at bottom faces. Due to its limited size it is equipped with a modest payload, including a camera, thermometer, photo-diode, and accelerometer. Additionally, it is equipped with four different types of mobility mechanisms [9]. Unfortunately, MINERVA-II-2 failed before deployment, as the rover was unresponsive to commands to turn on. MINERVA-II-2 was released regardless, and its trajectory was followed to further investigate the gravitational model of Ryugu [10].

1.1.5. MASCOT

MASCOT was a second, fully independent lander system also deployed by Hayabusa2 on the surface of Ryugu. MASCOT was developed by the German Aerospace Center (DLR) and the National Centre for Space Studies (CNES). MASCOT weighs 10 kg and carries a host of payloads, namely a wide-angle camera, spectroscopic microscope, thermal radiometer and magnetometer [9]. MASCOT is equipped with a primary battery to power all subsystems and payloads with an operational lifetime limited to around 17 hours, depending on power consumption. Its frame is built up on carbon-fiber reinforced plastic (CFRP) foam sandwich panels, which allowed the structure to deform a few millimeters after impact, thus dampening the resulting force. MASCOT is equipped with an eccentric arm with a mass concentrated at its tip; this arm is rotated and suddenly stopped using a geared DC motor. This generates an off-center reaction force following Newton's third law. This reaction sends the lander in an uncontrolled hop, with a maximum range of 20 m [10]. An image of MASCOT can be seen in Figure 1.4.

MASCOT was deployed twelve days after MINERVA-II on a different location on the surface of Ryugu. Due to its limited operational time, a 24-hour continuous monitoring network was set-up such that all the scientific experiments could be carried out. This was done with a combination of the JAXA, NASA and ESA deep-space networks. The lander operated nominally throughout the approach and landing process, bouncing a few times on Ryugu's surface before coming to rest. As the resting orientation after the rebound was undesirable, MASCOT hopped once, which successfully re-oriented it. After the completion of some payload operations, the hopping mechanism was triggered again for further scientific measurements. This second hop was also successful. After the expected 17 hours after deployment, MASCOT's battery ran out, therefore finalizing the mission [10].

Table 1.1: Summary of key lander parameters (data extracted from Yin et al. [14]).

Lander	Landing body	Landing system	Active descent control
NEAR Shoemaker	433 Eros	None	Thruster
MINERVA	25143 Itokawa	Spikes	None
Philae	67P/Churyumov–Gerasimenko	Flywheel, legs, anchor, ice screws, and thruster	Flywheel and thruster
MINERVA-II	162173 Ryugu	Spikes	None
MASCOT	162173 Ryugu	None	None

Lander	Dry mass (payload) [kg]	Deployment height [m]	Deployment speed [m/s]	Impact speed [m/s]
NEAR Shoemaker	487	36,000	1.5 - 1.8	-
MINERVA	0.59 (0.14)	200	0.15	-
Philae	97.9 (27)	22,500	0.05 - 0.52	1
MINERVA-II	1.1 (0.3)	50	-	-
MASCOT	10 (4.2)	41	0.05	-

1.2. Key takeaways

Two dedicated landers have generated significant scientific data of the SSSB they landed on, Philae and MASCOT. Philae is the largest lander, thereby being able to provide the most valuable scientific data, with a varied set of payload systems. However, its complexity also lead to its issues, where key subsystems like the harpoons and cold-gas thruster both failed. On the other hand, MASCOT uses a very robust landing methodology, which makes the lander highly reliable. However, it is severely limited in terms of payload, and its resting location on the SSSB's surface is relatively unpredictable. Furthermore, its design requires a low altitude-deployment, which is impractical for multiple deployments, consumes fuel, and endangers the mothership. Philae is a dedicated, one-off lander, and while

MASCOT's design is versatile, it is not adaptable. MASCOT's approach is significantly more low-cost, however it is severely limited in its operation, with a limited lifespan. Therefore, it seems like there is a gap in the available lander platforms for a highly adaptable lander able to operate in a wide range of SSSBs with simple adaptations, as no current lander fulfils this need. The lander should be highly reliable, thereby favouring passive technologies for landing and attachment.

1.3. Research questions

Following the investigation into the current paradigm of the state-of-the-art in SSSB landers, and in order to narrow down the scope of the thesis project, a research question is defined:

What is a suitable design for an adaptable SSSB lander platform able to deliver a surface payload in a range of different operating environments?

This main research question is broad in its span. Therefore, in order to aid in the completion of the project, it can be broken down into the following research sub-questions:

- *Which systems engineering methodology is best suited for the design of an adaptable SSSB lander?*
- *What is the range of possible operating environments for the SSSB lander?*
- *Which are the optimal key enabling subsystems for a SSSB lander?*
- *How can the key enabling systems be adapted to extend the range of operating environments?*

2

Methodology

A SSSB lander is a complex system, made up of individual subsystems which must communicate with, and complement each other. The lander can be considered a system of systems, thereby requiring a structured and well defined approach to efficiently develop its design. In order to do this, two different systems engineering methodologies are adopted.

2.1. Constraint-driven engineering (CDE)

When designing a system for a specific application, or when improving an existing system, it is common practice to set down specific requirements to constraint the design and measure its effectiveness. These requirements are derived from discussions with relevant stakeholders. As the mission progresses from the conceptual stage to final hardware integration, requirements are devolved with increasing levels of detail, while maintaining the traceability required for justification. As design reviews take place, requirements become frozen, which forms the baseline for the next design iteration [15].

In space missions the typical design process follows the initial definition of a payload of interest for a relevant target. Then, conventionally, a spacecraft bus is designed around the payload such that it may accommodate it, while also fulfilling the relevant requirements imposed by the selected launch vehicle [16]. However, there is an alternative design paradigm: CDE. This paradigm aims to address designs which may not be narrowed-down to a single reference mission scenario, such as an adaptable lander [17].

CDE has been used in the development of a lander mission, specifically MASCOT, as it is considered a more agile methodology than requirement-driven design [15]. Rather than fulfilling a set of requirements, CDE aims to produce the best possible design based on several factors, which is able to operate within its environmental constraints. For a highly adaptable lander, the main constraints are the volumetric and mass constraints imposed by a mothership. The goals for the lander design are: maximizing payload volume and mass, deployment height, and the number and types of SSSBs where the lander concept may successfully land. For the adaptable lander, a small form factor is preferred following the conclusions drawn in Section 1.2. Therefore, the volumetric and mass constraints will be set to those of MASCOT, with an assumed envelope of 6U and a mass in the order of 10 kg.

2.2. Model-based systems engineering (MBSE)

MBSE is a systems engineering tool, widely supported by the International Council on Systems Engineering (INCOSE), which promotes the development of projects as sets of interconnected models

which are continuously updated [18].

MBSE promotes iterative design, with a central system model represented using technical diagrams displaying the different connections between the engineering models [19]. Common tools to generate these models include Rational Rhapsody, and Systems Modeling Language (SysML). MBSE offers agile requirement integration and verification, varying levels of abstraction of the model, and quick iteration between design options [20].

MBSE has already been employed successfully in the context of SSSB landers, being the design methodology used for MASCOT, as detailed in the internal publication by Kretzenbacher et al. [21]. Within the DLR, MBSE has been set as the methodology to follow for future missions, following a detailed procedure published internally by Lange et al. [22]. Although neither of these publications is publicly available, Ogunshile et al. [20] published an earlier study for a general asteroid lander. Caroline Lange is a co-author for this paper which lends it credence, as she was an author for both of MASCOT's internally-published articles.

A sample system model for an asteroid lander was included in the work of Ogunshile et al., which can be seen in Figure 2.1. This model, generated using Rational Rhapsody, shows the derivation of requirements for the asteroid lander based on its functionalities, as well as the connections of the system with external elements such as the mothership. It is important to note that this is a heavily reduced model, with a high level of abstraction, for a generic mission. Therefore, it is not representative of the final product of a successfully developed MBSE model.

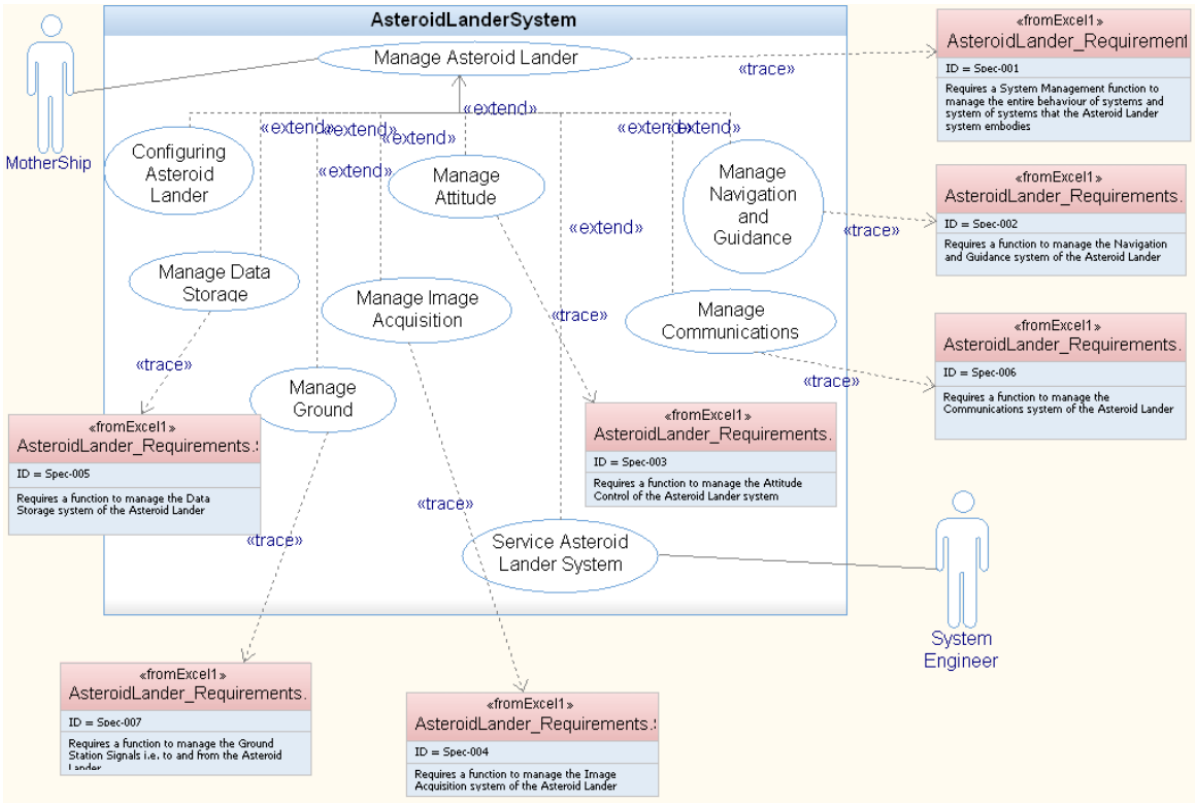

Figure 2.1: Sample MBSE model for an asteroid lander (from Ogunshile et al. [20]).

The latest development in the field of MBSE has been proposed by Gianni, D'Ambrogio and Tolk in their book: "Modeling and Simulation-Based Systems Engineering Handbook" where Model- and simulation-based systems engineering (MSBSE) is proposed as an extension of MBSE [23]. MSBSE draws inspiration from software development, and model-driven architecture (MDA) in particular. The core of MDA is to replace the single-platform (SysML) models, where the only purpose is the grouping of variables to give an overall picture, with functional models such as executables and scripts. MSBSE aims to truly

enable iterative design, allowing models to run contiguously and independently by adding simulations to the models themselves.

According to the work of Ludewig [24], engineering models must have mapping, reduction and pragmatic criteria. This means that the models must represent characteristics of a real world system (mapping), without involving all parameters defining the system (reduction). Lastly, the models should be useful enough to fully replace the original in a single area (pragmatic). In the context of the preliminary design of the lander, the main models considered are: the system model, the Computer-Aided Design (CAD) model, and the ballistic model. The ballistic model will be used to design and validate the impact absorption and anchoring subsystems. The CAD model will be used to verify that requirements such as volume and mass are met. Additionally, simpler sub-models may be implemented if this is deemed necessary such as radiation, thermal and power generation models.

A very clear advantage of MBSE is the fact that the models can easily be modified, and improved independently, thus enabling an iterative design process. Therefore, MBSE is selected as the framework to be used for the design of the lander. For the lander design, initially a number of concepts will be drawn up such that they fulfil the subsystem requirements. Their performance will then be evaluated both based on their characteristics and their output from the simplified models. This will allow for detailed trade-offs without much of the guesswork that often goes into these. Once a suitable concept has been chosen via the trade-off techniques, the models can be further refined to get more accurate results.

2.3. Preliminary system model

The MBSE framework requires a system model which captures different properties of the model. This model must follow SysML, a system architecture modeling language specifically developed for Systems Engineering [25]. The model is represented using sets of diagrams, namely behaviour, requirement, and structure diagrams, as shown in Figure 2.2.

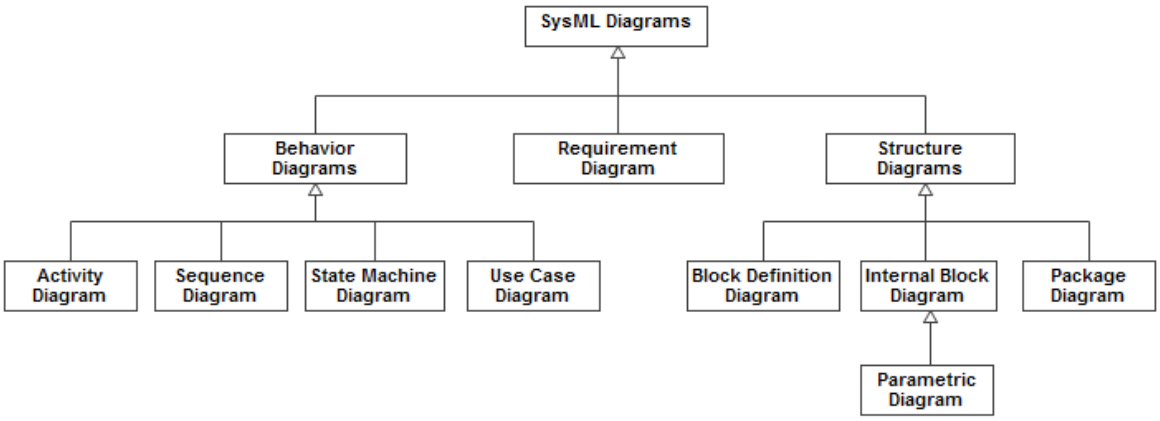

Figure 2.2: SysML diagram taxonomy.

These diagrams aim to capture different characteristics of the system. While a full implementation of each diagram will provide the most complete overview of the system, it is not required for the pre-conceptual design phase. Partial implementation of some of these diagrams, however, can aid at this stage as they can be used to derive functional requirements at the component and system level, specify the expected use cases, and set the expected architecture of all the interacting systems (mothership and lander). For this purpose, an initial analysis of the lander is performed using the Requirement, Block definition, Sequence and Use case diagrams. Some of the building blocks of these diagrams are shared, for instance the system and subsystem blocks.

2.3.1. System diagrams

Block definition diagrams are used to convey a system's components, their interfaces, and the relationships between them; thereby defining the architecture of the system [25]. Figure 2.3 and Figure 2.4 display the diagrams generated for the lander and mothership respectively. The lander is the main system evaluated in this thesis project, therefore its block definition diagram is significantly more detailed.

Figure 2.3 shows two main connection types between blocks, wires and comms. Wires supply power to the different subsystems and originate in the "Electrical Power System" block. Comms are always bidirectional, as data and commands are transmitted back and forth between the relevant subsystems and the "Command, Communications, and Data Handling" subsystem block. Lastly, parent block decompositions are represented using a filled rhombus below the block, with the parent block being decomposed into smaller subsystems.

Operations are defined as actions that an individual system block must carry out. Operations may be related to both internal tasks, such as powering the lander, and external activities, such as attaching to the surface of the SSSB. Values, on the other hand, define the key parameters that determine the performance of the main functionality of each block. Additionally, a number of blocks are connected to specific external activities which they satisfy.

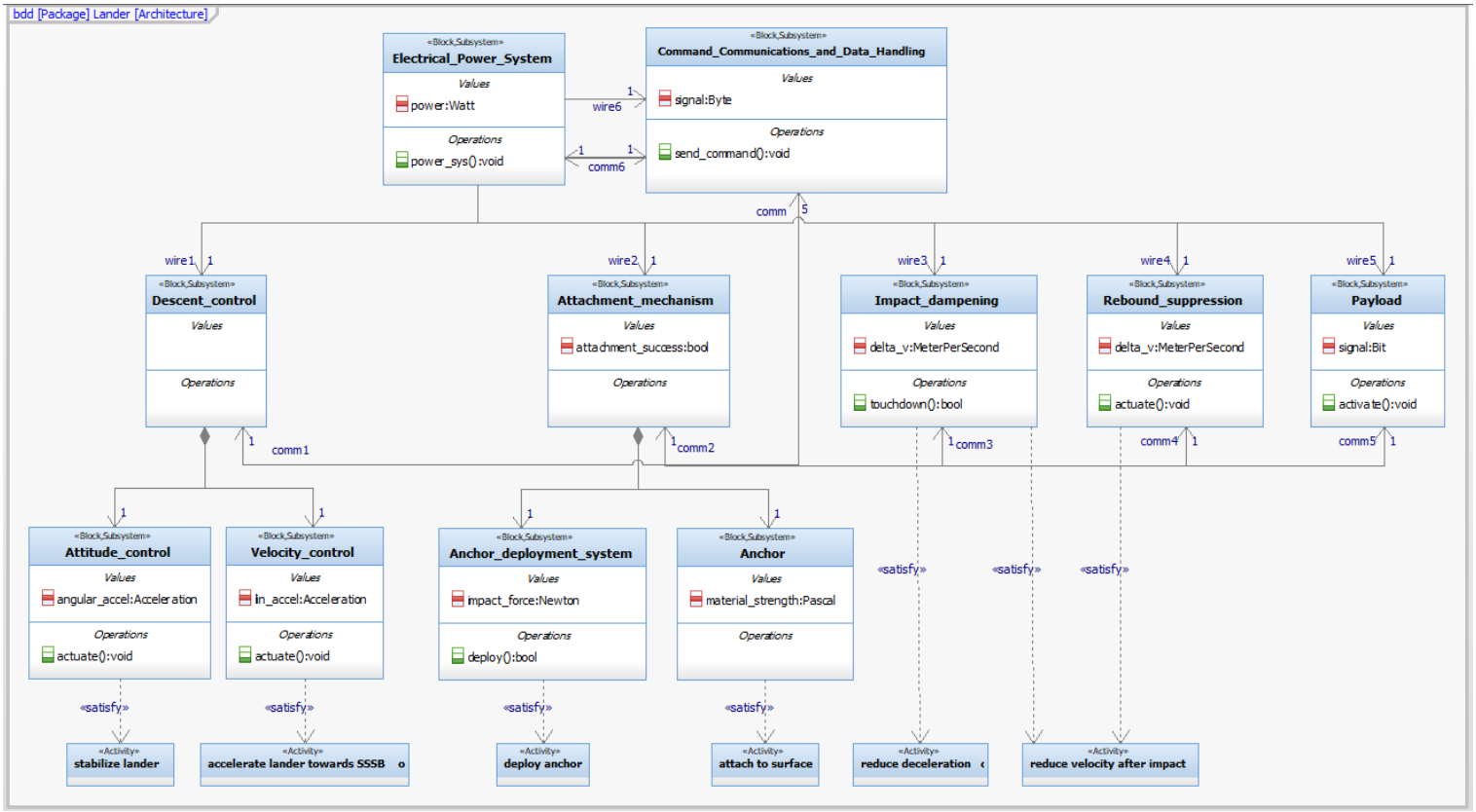

Figure 2.3: Block definition diagram Lander.

The block definition diagrams define the architectures of both lander and mothership. Consequently, the functions that each of these systems must perform are also allocated. This results in the definition of the landing-enabling subsystems as shown in Figure 2.3: the descent control, impact dampening, attachment, and rebound suppression subsystems.

If these subsystems are implemented in the lander, they must fulfil a set of system requirements. As the thesis project follows the CDE paradigm, these requirements must be either functional or high-level system requirements, with no strict numerical boundaries. The derived requirements, together with

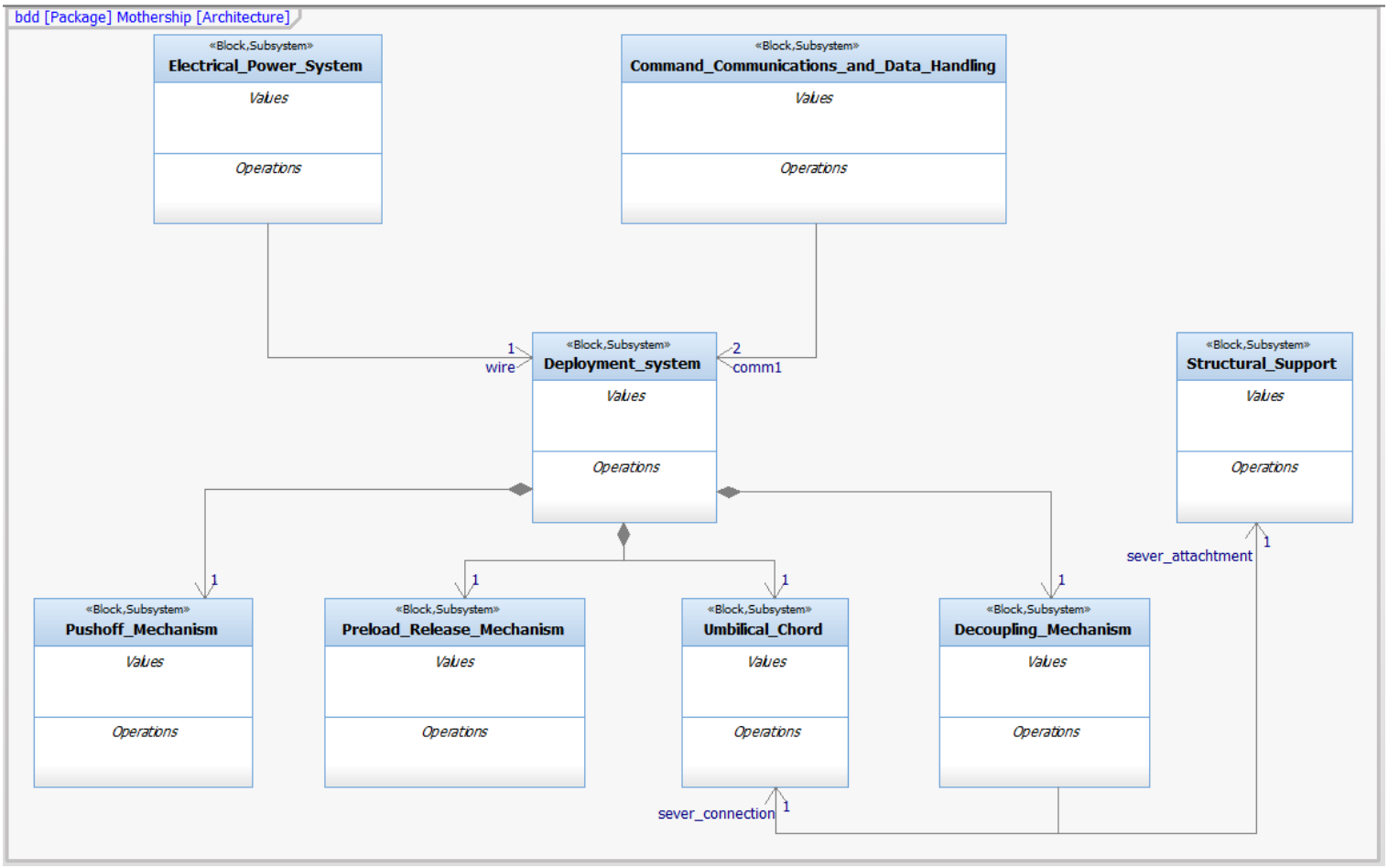

Figure 2.4: Block definition diagram Mothership.

their associated subsystems are showcased in Figure 2.5.

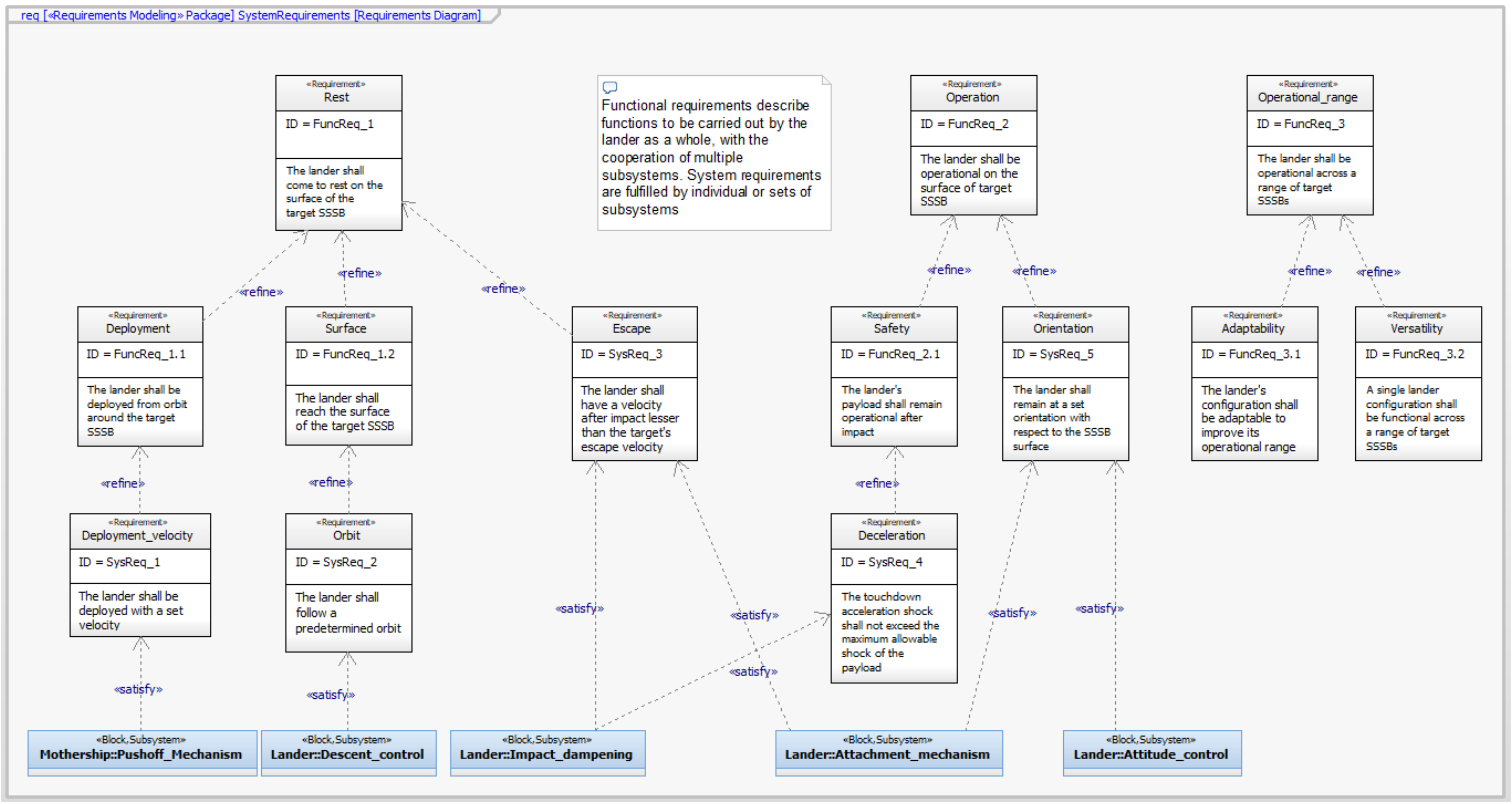

Figure 2.5: Requirement diagram.

Functional requirements are those which are fulfilled by the lander as a whole. System requirements on the other hand, are specific to one or several subsystems. The main requirements originate from the three main functions of the lander: to reach, and stay on the target's surface, to remain operational while doing so, and to be suitable for a number of SSSBs. These requirements are further refined into different levels, ultimately defining the main responsibilities for each subsystem.

The use case diagram defines the possible operations between the systems and external actors. A single use case diagram was generated, with the lander, mothership, and external actors as displayed in Figure 2.6. Due to the large delay in communications in deep space, the lander operation must be either autonomous or uncontrolled. Therefore the number of interactions with external actors during the operation phase is limited to activation and communications. System adaptations required for a specific SSSB target are also part of the use cases of the lander, and are therefore also represented in the diagram.

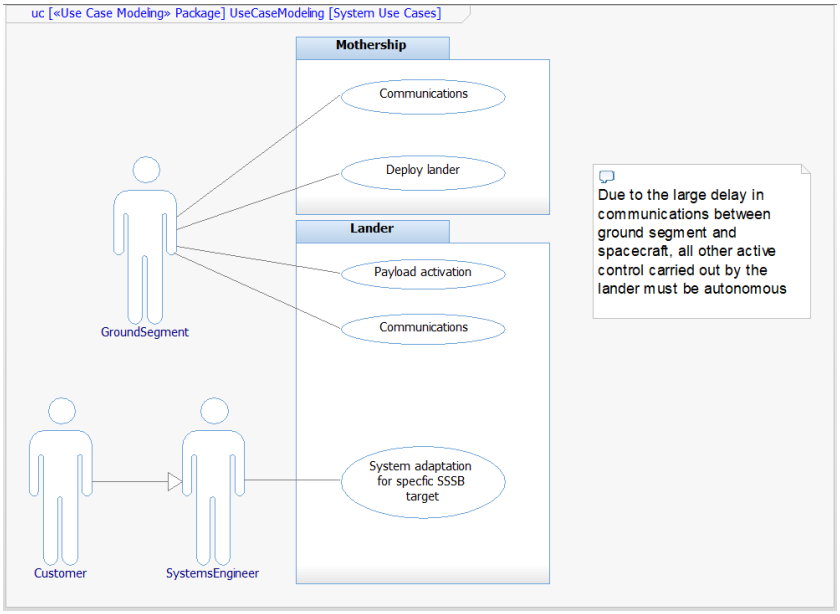

Figure 2.6: Use case diagram.

Lastly, the sequence diagram is shown in Figure 2.7. It defines the expected sequence of interactions and events carried out between the different subsystems of the mothership and lander, as well as the ground segment. This allows for the specific definition of all interactions between subsystems, and the order at which the events will take place.

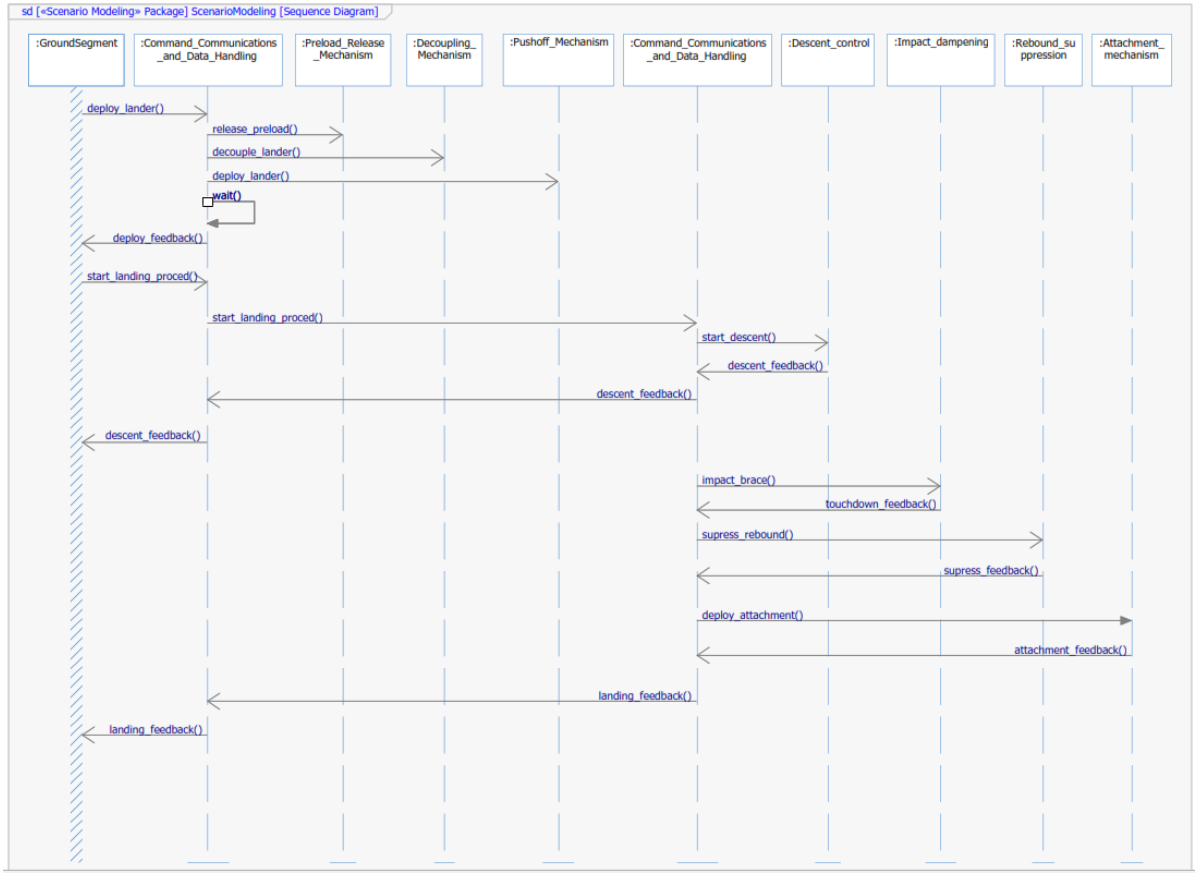

Figure 2.7: Sequence diagram.

3

Small Solar System Bodies

SSSBs are the main direct source of knowledge for the formation of the Solar System, due to their differentiation and relatively inactive surfaces [26]. Furthermore, the study of SSSBs is useful in the context of Earth endangerment, where large SSSBs in near-Earth orbits present a significant risk to our planet, and further research into non-gravitational forces such as the YORP effect is critical. Lastly, there is a fast-growing interest on the potential future industrial use for SSSBs. Possible industrial uses include supporting future space missions by extracting necessary materials such as water and bringing rare precious materials like platinum back to Earth [2].

3.1. SSSB exploration

As of today, 17 deep-space missions have been launched by a number of organizations to explore SSSBs, with 24 individual objects being surveyed; some of which having multiple missions dedicated to their study [14]. These missions have taken place in the form of fly-bys, landings, impacts, orbital flights, and sample-returns. A list compiling all the missions that have taken place can be seen in Table 3.1. Here each mission is highlighted, together with the celestial objects visited, their type, the exploration method used for research, and the time at which the mission was undertaken. These missions include those presented in Chapter 1.

3.2. SSSB types

SSSBs are characterized and categorized based on their origin, composition, and orbit. SSSBs have been classically grouped into two main categories: asteroids and comets. However, this classification in reality is better expressed as the asteroid-comet continuum, with most objects clearly established at ends of the spectrum but with notable exceptions sharing characteristics of both [26].

3.2.1. Asteroids

Asteroids can be sorted based on several classification methodologies. The simplest method is their orbital range, which splits them into Near-Earth Asteroids (NEA), Main-Belt Asteroids (MBA), and trojans. MBA form the large majority of the known SSSBs, totalling about 90%; NEA account for most of the remaining 10% [27]. It is important to note that these figures, while accurate, do not signify that this is the actual ratio of SSSBs, as many remain undiscovered. As mentioned previously, NEA are a potential planetary hazard and therefore, especial emphasis has been made on identification efforts.

Table 3.1: Deep-space missions to SSSBs (adapted from Yin et al. [14]).

Mission name	Object Name	SSSB type	Exploration methodology	Mission time
Galileo	951 Gaspra	MBA (S-type)	fly-by (1600 km)	1991/10
	243 Ida	MBA (S-type)	fly-by (2410 km)	1993/08
NEAR-Shoemaker	253 Mathilde	MBA (C-type)	fly-by (1212 km)	1997/06
	433 Eros	NEA (S-type)	orbit, landing	2001/02
Deep Space-1	9969 Braill1e	NEA (Q-type)	fly-by (15 km)	1999/07
	19P/Borrelly	Comet	fly-by (2171 km)	2001/ 09
Stardust	5535 Annefrank	MBA (S-type)	fly-by (3079 km)	2002/11
	81P/Wild-2	Comet	fly-by (236 km)	2004/01
			sample-return	
	9P/Tempel-1	Comet	fly-by (181 km)	2011/02
Deep Impact	9P/Tempel-1	Comet	impact-style	2005/07
	103P/Hartley	Comet	fly-by (700 km)	2010/11
New Horizons	132524 APL	MBA (S-type)	fly-by (10^4 km)	2006/06
	2014 MU69	Kuiper object	fly-by	2019/01
Dawn	4 Vesta	MBA (V-type)	orbit (210 km)	2011/07
OSIRIS-Rex	101955 Bennu	NEA (C type)	sample return	2020/1
Sakigake	lP/Halley	Comet	fly-by (10^4 km)	1986/03
Suisei/Planet-A			fly-by (699 E4 km)	
Hayabusa	25143 Itokawa	NEA (S type)	sample-return	2005/11
Hayabusa-2	162173 Ryugu	NEA (C type)	sample-return	2019
	1998 KY26	NEA (uncertain)	plans to rendezvous	2031/07
Giotto	lP/Halley	Comet	fly-by (610 km)	1986/03
	26P/G-S	Comet	fly-by (200 km)	1992/07
Rosetta	2867 Steins	MBA (E type)	fly-by (800 km)	2008/09
	21Lutetia	MBA (M type)	fly-by (3162 km)	2010/07
	67P/C-G	Comet	landing	2014/11
Vega-1	1P/Halley	Comet	fly-by (8890 km)	1986/03
Vega-2			fly-by (8030 km)	
Chang'e-2	4179 Toutatis	MBA (S type)	fly-by (3.2 km)	2012/12
ICE	21P/G·Z	Comet	fly-by (7800 km)	1985/09
	1P/Halley	Comet	fly-by (28E6 km)	1986/03
Cassini-Huygens	2685 Masursky	MBA (S type)	fly-by (16^5 km)	2000/01

NEA can be further classified into three groups based on their orbital characteristics. If the orbits of both the NEA and Earth are close, but do not intersect, it is considered an Amor asteroid. Apollo asteroids, on the other hand are those which while intersecting Earth's orbit, have highly eccentric orbits and spend most of their orbital period outside Earth's orbit. Lastly, Atens also intersect Earth's orbit while spending most of their orbital period within Earth's orbit [27]. A diagram representing the typical orbits of NEA as well as the asteroid belt is shown in Figure 3.1.

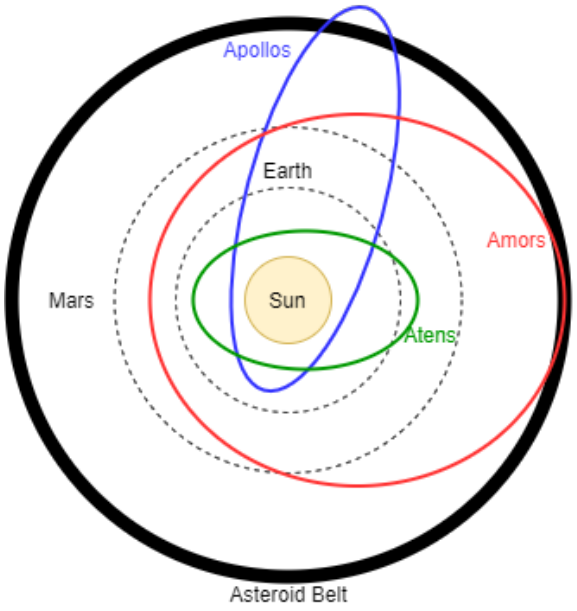

Figure 3.1: Orbital diagrams of the different types of NEA and the MBA.

The main asteroid belt is the most abundant region, in the known solar system, in SSSBs. The belt has been classically divided into three regions relative to their semi-major axis: the inner, intermediate, and outer belts. These regions are separated by the 3:1 and 5:2 Kirkwood gaps, which are sections in the semi-major axis distribution of the main-belt where no asteroids are present. These gaps originate due to the orbital resonances of Jupiter's orbit around the Sun [27].

Asteroids can be further categorized based on their spectral emissivity. Iterative efforts have been made to create and refine these categories, in a process named asteroid taxonomy. The most notable and widely accepted early work was that of Tholen, who in 1984 defined seven major classes of asteroids: A, C, D, E, M, P, and S with additional sub-classes [28].

The latest development in this field took place with the second phase of the Small Main-belt Asteroid Spectroscopic Survey (SMASSII), where spectra information was derived for 1447 asteroids. The thorough analysis of the data allowed for more detailed classification, as well as for the expansion of some groups which were previously isolated to single individual asteroids. The new taxonomy elaborated by Bus and Binzel [29], rather than replace Tholen's model, aimed to refine it. This resulted in the definition of 26 classes, 12 of which have the traditional single letter designation: A, B, C, D, K, L, O, Q, R, S, T, V, and X. Here, the L-category was a new contribution by this study. Additionally, 14 classes were elaborated for objects with intermediate spectral features, identified with a multi-letter designation: Cb, Cg, Cgh, Ch, Ld, Sa, Sk, Sl, Sq, Sr, Xc, Xe, and Xk. It is important to note that, while the classification of the major groups follows clearly defined rules, the differences between these objects may not be as significant as it seems in specific spectral characteristics as can be seen in Figure 3.2. The distribution of asteroid types of objects >20 km diameter recorded in the SMASSII can be seen in Figure 3.3. The prevalence of the C, S, and X groups is apparent, typically accounting for over 80% of the asteroid population with the individual groups exceeding 60% of the total population at times.

The C, S, and X groups of asteroids make up the majority of SSSBs in the solar system. The C and S groups, refer to carbonaceous and siliceous asteroids respectively, with the X group being com-

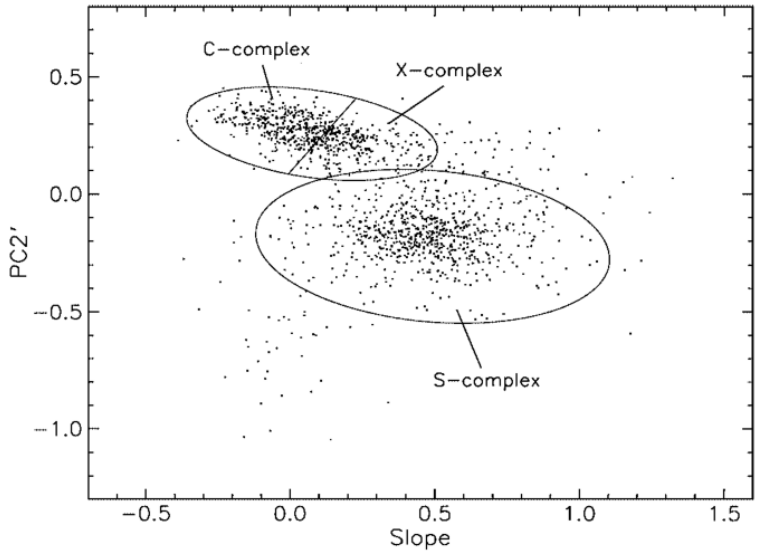

Figure 3.2: Plot of spectral components (Slope and PC2') of SMASSII sample with C-, X- and S-groupings (from Bus and Binzel [29]).

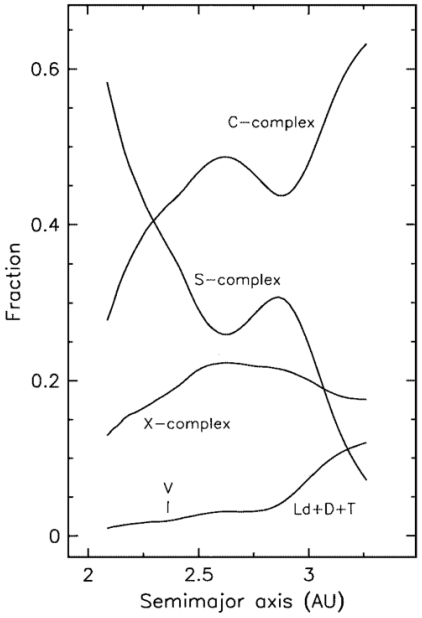

Figure 3.3: Heliocentric distribution of diameter >20 km MBA between 2.1 and 3.3 AU (from Bus and Binzel [29]).

posed mainly of metallic asteroids. These designations originate from the spectroscopic measurements, where based on the absorption spectra, surface materials can be inferred [28]. Carbonaceous asteroids are made of hydrated minerals, with a water content of up to 20% (in individual mineral concentrations). C-type asteroids make up the majority of the outer asteroid belt, accounting for up to 75% of the composition in that area. Siliceous asteroids account for approximately 17% of known asteroids and are the predominant type of NEA, accounting for 40%. The largest sub group among X-type asteroids are M-type asteroids, which are the main source of iron meteorites reaching Earth, and by themselves represent the third-largest asteroid class. The average densities of C-, S-, and M-type asteroids have been estimated to be 1.38, 5.32 and 2.71 g/cm^3 respectively [30].

3.2.2. Comets

Comets are distinguished from asteroids due to their activity and inactivity periods. As comets contain volatiles, when their eccentric orbits bring them sufficiently close to the Sun, they undergo outgassing. Due to the vacuum of space these gases expand, generating a coma, which is a very thin atmosphere around the cometary nucleus. If the solar pressure is sufficient, the coma will extend into a much larger tail. Comet nuclei have been estimated to have small densities, below 1.0 g/cm. The nucleus of the comet is best described as an aggregate of icy-conglomerate cometesimals, lacking a compact body like some asteroids and simply being bonded together by gravitational attraction, similarly to rubble piles, with little to no cohesion. This composition explains phenomena exhibited by comets, such as their recomposition after being disrupted, and the lack of comets exhibiting rotational periods shorter than 5.2 hours [31].

As comets exhaust all of their internal volatiles, they enter a flame-out state, where they become dormant and no longer outgas. The fact that a number of what today are categorized as asteroids are extinct comets is widely accepted within the scientific community [14].

3.3. Surface morphology

SSSBs are populated by boulders of different sizes. The most detailed work regarding the distribution, shape and size of these boulders is an article published by Michimaki and Hagermann. The authors, in continuation of a previous paper, where they applied a custom methodology to model the boulders of asteroid Ryugu, extended this research by applying it to the raw data from asteroids Itokawa and Eros. Their findings were focused on deriving appropriate power indices to describe the boulder distribution on the surface of these asteroids [32]. Power indices are the exponents used for mathematical expressions which make use of the power law. This law has been found to accurately represent the distributions of several natural and man-made phenomena. It follows the form:

$$p(x) \propto x^{-\alpha}, \tag{3.1}$$

where α is the aforementioned power index. According to the work of Clauset, Shalizi, and Newman, α is usually in the 2-3 range with a limited number of exceptions [33]. The magnitude of the power index can be used as a measure of how fragmented the SSSB is. Michimaki and Hagermann's paper found power indices for the boulder distribution of 3.25 ± 0.14, 3.05 ± 0.14, and 2.65 ± 0.05 for Eros, Itokawa, and Ryugu respectively. While slightly exceeding the typical index for power laws, the difference is not significant; therefore, the power-law distribution of boulders can be considered a good model for SSSBs. Michimaki and Hagermann's findings can be seen in Figure 3.4.

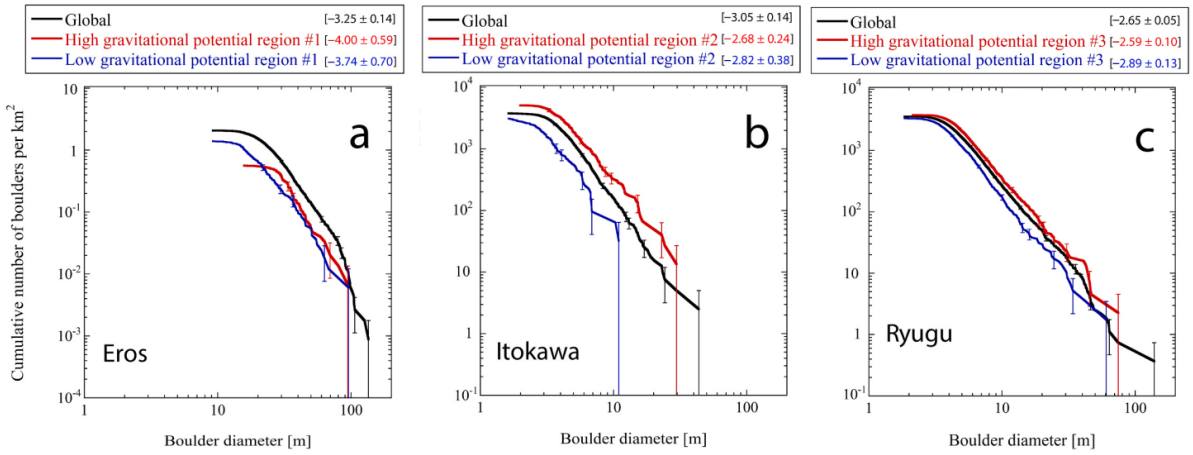

Figure 3.4: Cumulative boulder size distributions in high and low gravitational potential regions for Eros, Itokawa, and Ryugu (adapted from Michimaki and Hagermann [32]).

The surface of a SSSB is continuously evolving, with differently-sized boulders migrating throughout its surface. This migration can be caused by seismic events which originate from external impacts, only occasionally taking place due to thermal expansion as the SSSB transverses its orbit. It is logical that smaller boulders migrate more easily due to their lower friction angle. Additionally, the ratio of boulders migrating, as well as the boulder's destination will logically be determined mainly by the local gravitational acceleration. This results in regions with higher gravitational potential having less boulders, with a higher ratio of larger boulders (all other conditions being equal). Another factor that will affect the distribution and migration of boulders is the centrifugal force on the surface of the SSSB. If the rotational period is small enough, boulders will appear in high concentrations along the equator of the SSSB. Lastly, a majority of boulders in an SSSB may originate from a specific location on the SSSB's surface. This can be traced to an individual event in the history of the SSSB. Both the centrifugal and the single-event concentrations can be seen in Eros, where most of its boulders are concentrated around the Shoemaker crater, with the remainder being mostly present along the equator [32].

3.4. Surface composition

SSSBs, despite their differences, are made up of consistent sets of materials: regolith, rock, and ice. These are not specific materials but rather groups of materials sharing a general morphology.

3.4.1. Regolith

Regolith is a powder-like surface layer of rock fragments of variable thickness present in SSSBs. To date, every single airless body that has been explored had regolith on its surface. Megaregolith is another term used to describe the layers of an SSSB, encompassing surface regolith and additional material that has been affected or transported by space weathering. This includes foreign impact objects, melted material from impacts, and fractured bedrock. An schematic representation of the layers of regolith on the Moon can be seen in Figure 3.5.

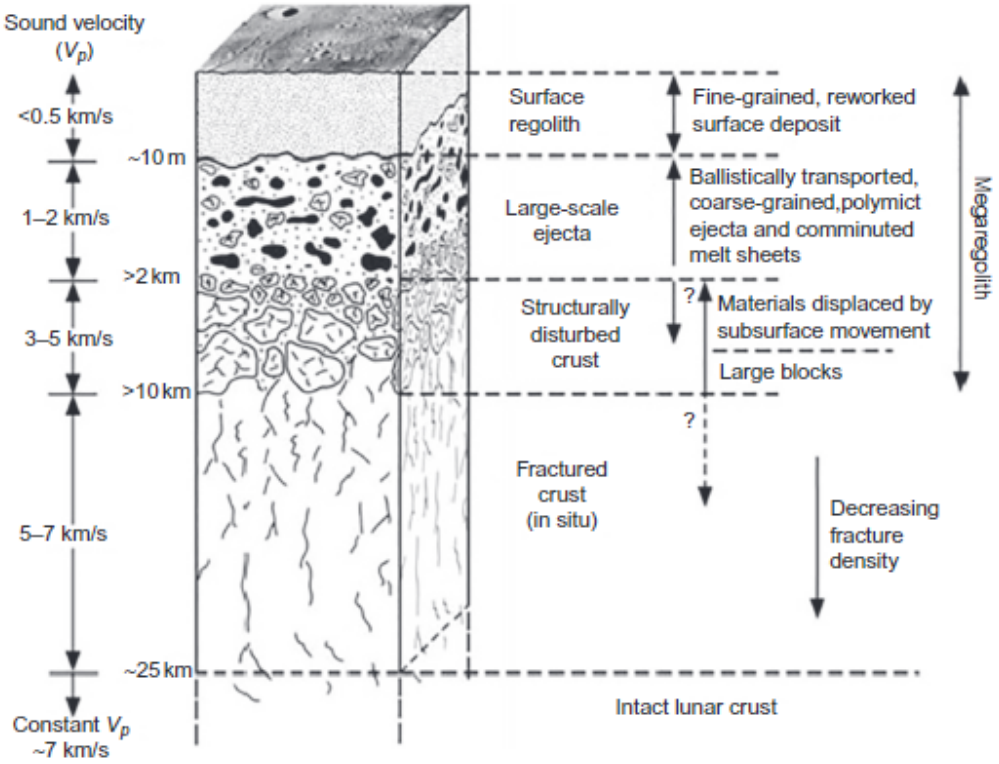

Figure 3.5: Layers of the Moon (from Grier and Rivkin [34]).

While the Moon is orders of magnitude larger than any known SSSB, the overall structure is similar for large, rocky asteroids such as Vesta. In smaller bodies the lower gravitational attraction means that material is more likely to escape the body, but the layer structure still holds. While larger bodies such as moons have a solid bedrock at their core, some SSSBs such as Eros, are thought to be fully made up of megaregolith; these are referred to as ”rubble piles” [34].

The process of formation of regolith is complex, with several mechanisms contributing to its development. The most well understood mechanism of regolith formation is impact-driven, where the energy from collisions breaks apart rocks and boulders, thereby creating regolith. These impacts may be both large- and small scale, with impacting materials ranging anywhere from micrometeoroids to other SSSBs.

Further fragmentation of asteroid material is also caused due to thermal fracturing. Due to the lack of atmosphere, temperature changes on the surface of an SSSB are large, experiencing day/night cycles as well as seasonal variations in their heliocentric orbits. SSSB rocks are made out of several different

mineral types, each with their individual coefficients of thermal expansion. Therefore, as temperatures fluctuate these minerals expand and contract at different rates, thereby generating microscopic cracks in the material. These cracks can propagate and affect the material in the macroscopic scale [34].

Direct regolith observations from the sample extracted from Itokawa show particle grains ranging from 3 - 180mm, with the large majority being < 10mm. The depth of regolith varies from one SSSB to the other, as well as across the surface. Measurements from the smooth regions of Itokawa show regolith depths of 2.5 m, while the regolith depth in Eros varies in the order of tens of meters. It is theorized the relative variance throughout Eros' surface is due to the irregularity of the ejecta from crater blankets. Measurements of Eros' regolith indicate a fine regolith, with most particles being finer than one millimeter in size. On the other hand, Itokawa's regolith was found to be mostly > 1mm in size [35].

3.4.2. Volatiles

Volatiles are a classification of elements and chemical compounds: referring to those chemicals which are prone to vaporization, which includes solids, liquids, and gases. The term "ice" is used to describe those volatiles with melting points above 100K, while the term "gas" is used for those below that threshold [36]. Volatiles are mostly present in comets, but also appear in asteroids. When volatiles are heated to a sufficient temperature, as the SSSB transverses its orbit, they start outgassing. Volatiles are very diverse, with many different types of chemical compounds present as species. A logarithmic plot of the different concentrations of volatiles in comets can be seen in Figure 3.6, where the numbers above each bar represent the number of comets that have been included in the dataset, and the bar shading represents maximum and minimum values.

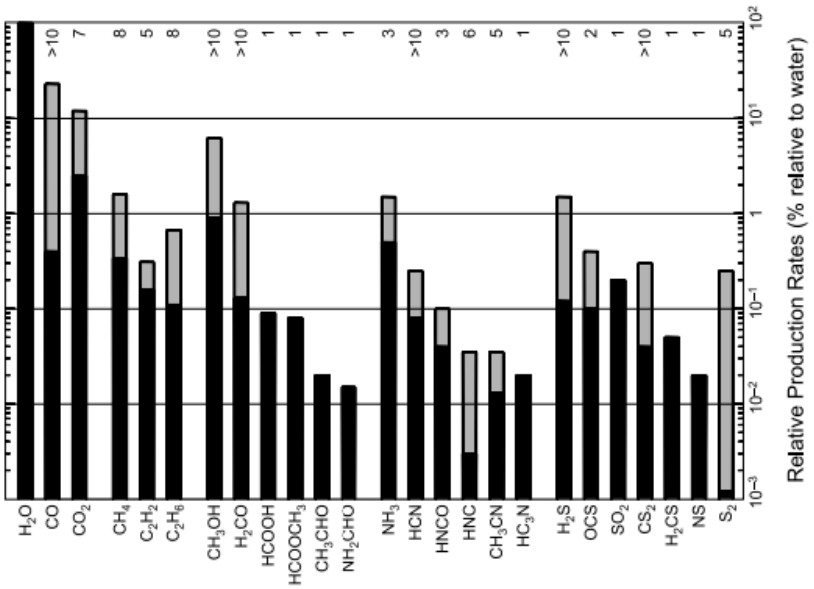

Figure 3.6: Abundance of volatiles in comets relative to H_2O (from Bockelée-Morvan et al. [34]).

Water is used as the species for comparison, as it is by far the most common chemical compound present in volatiles, accounting for over 90% of the total distribution in most comets. The remainder compounds are mainly organic compounds: oxocarbons, hydrocarbons, and some hydrogen-carbon-oxygen chains[37].

3.4.3. Mechanical properties

The mechanical properties of SSSBs are critical for the design and evaluation of the impact dampening and attachment subsystems. The strength of the material, together with the impact speed, will dictate

the deceleration experienced by the lander. Additionally, landing systems tend to be tuned for a specific material strength. For instance, for a harpoon attachment system, the anchoring material's strength must be sufficient to support the anchor but below that of the harpoon such that the material may be penetrated.

The mechanical properties of the rock granules are well understood and can be derived from laboratory testing on Earth. Wada et al. derived values for the crushing strength of different rocky materials for mm size range particles as shown in Table 3.2

Table 3.2: Crushing strength of different rocky materials (*Sandstone included as the lower threshold for Ryugu) (adapted from Wada et al. [38]).

Materials	Crushing strength (MPa)
Chondrule from Allende (CV3)	7.7 ± 5.9
Chondrule from Saratov (L4)	9.4 ± 6.0
Dunite (a few mm)	13.1 ± 2.6
Basalt (a few mm)	16.9 ± 2.6
Sandstone (a few mm) *	3.4 ± 1.1

Herstroffer et al. performed an in-depth study of rubble-pile type asteroids, where they performed simulations which indicated that the cohesive force (equivalent to the material strength) of these megaregolith asteroids varied in the order of 1-10^3 Pa [26]. Cometary measurements taken by the Deep Impact probe in comet 9P showed a material strength below 65 Pa; while the different touchdown sites of Philae provided three data-points for material strength of 1 kPa, 2 MPa, and 4 MPa respectively [39].

The coefficient of restitution can be defined as the ratio between the magnitude of the relative normal velocities before impact and after separation from the contact surface [40]. From Philae's and Hayabusa2's landings, coefficients of restitution have been derived for 67P and Itokawa. The coefficient of restitution for Philae's landing has been found to be between 0.5-0.8, while for Itokawa it was estimated at 0.83. On the opposite extreme, rocks on Eros have been found to bounce against the surface with a coefficient of restitution of 0.1 [40]. One important detail is that Itokawa's measurement was taken by Hayabusa2 as it descended unto the surface with a sample collector arm. This arm was outfitted with a spring element, which simply stores mechanical energy and releases it, thereby increasing the velocity after impact. Nonetheless, these values are still feasible as indicated by Biele et al., where 0.85 was calculated to be the coefficient of restitution of 2 granite spheres with 1 m diameter colliding at 1 m/s [40].

The coefficient of restitution is not exclusively dependent on the impact surface; instead, it also varies based on the impact speed and the damping coefficient of the lander itself. Perfectly elastic collisions will have a coefficient of restitution of 1, while perfectly inelastic contacts (where the bodies stick together after contact) have a value of 0. It is important to note that the coefficient of restitution could have values larger than 1, if an existing rotational motion of the lander is transformed into translational motion after the impact [40].

The effect of impact velocity velocity on the coefficient of restitution was derived by Thornton and Ning. The plot for this relation can be seen in Figure 3.7. The yield velocity v_y was defined by Thornton and Ning as the relative velocity below which the impact can be assumed to be fully elastic. The sticking velocity v_s is the maximum velocity at which there is no rebound, or a fully inelastic collision [41].

Porosity is defined as the ratio of void volume of an object relative to its total volume. Porosity can be measured at the individual mineral or sample level as well as at the SSSB level. Measurements from meteorites have indicated mineral porosity values of around 10%. On the other hand, SSSBs exhibit much higher porosity levels, which correlate well with their taxonomy [43]. The porosity of asteroids in particular has been found to range between 30-50% with the minimum and maximum values originating from S- and C-type asteroids respectively[42]. This mismatch indicates that there is a significant level of macroporosity in SSSBs, with a significant number of them being being rubble piles of loosely-aggregated material.

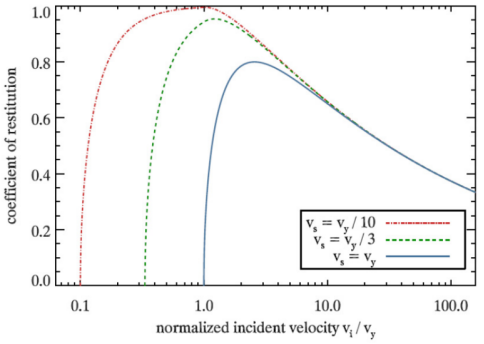

Figure 3.7: Coefficient of restitution as a function of velocity (from Biele et al. [40])).

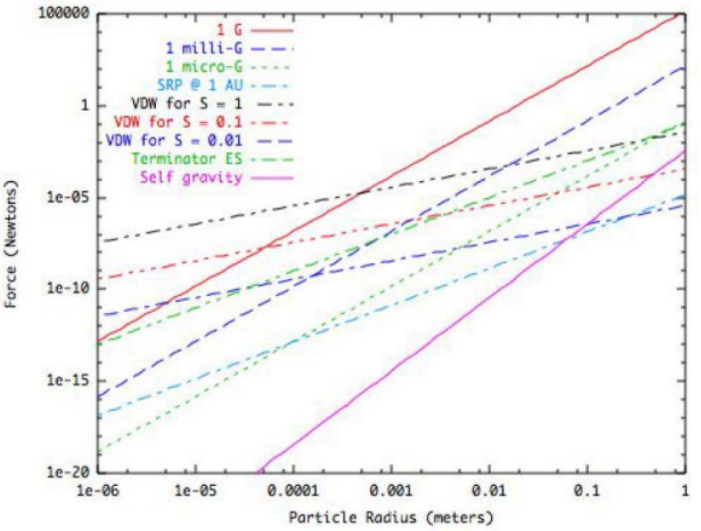

Figure 3.8: Magnitude of the different forces on the surface of an SSSB as a function of particle radius (from Scheeres et al. [42]).

The physics governing particle interactions and their cohesiveness are significantly more complex than those in the macroscopic realm, with many forces having a significant role. These include coulomb friction, interior pressures, self-gravity, electrostatic forces, solar radiation pressure, and surface contact cohesive (van der Waals) forces. These forces are all dependant on the particle radius. Therefore, Scheeres et al. carried out an analysis of the magnitude of these forces for an SSSB, which can be seen in Figure 3.8.

It can be clearly observed from Figure 3.8 that the magnitude of the forces affecting particles is heavily dependent on particle size. Data regarding the particle sizes in the surface of SSSBs is scarce; measurements from Eros show sub-milimeter particles sizes, with the thinnest dust estimated at 50 micrometers. On the other hand, Itokawa exhibits particle sizes in the millimeter to centimeter magnitude [42]. Following the work by Scheeres et al., this leads to the determination that the dominant forces at this scale are van der Waals and electrostatic forces (referred to as VDW and Terminator ES in the legend of Figure 3.8).

Electrostatic forces can be repulsive or attractive depending on the polarity of the charged particles; however, according to the work of Castellanos et al. [44], in neutrally-charged powders such as regolith, particles will tend towards the state of minimum electrostatic energy. Particles therefore orient themselves such that there is always an attractive electrostatic force between them. Rietema's [45] assessment of the electrostatic force between regolith particles poses that the electrostatic attraction is negligible, relative to the van der Waals forces.

Van der Waals forces describe intermolecular attractions which take place regardless of charge. Electric dipoles are generated by the electrons around a nucleus. An attraction between molecules begins when this dipole creates an electric field, which polarizes any nearby molecules, thereby generating a second dipole. The dipoles then are attracted to each other, leading to van der Waals forces [44]. Scheeres et al. [42], assumed that lunar regolith has consistent properties with that regolith found on SSSBs, thereby approximating that the van der Waals attractive force between two spherical particles at zero distance is obtained by:

$$F = 3.6 \times 10^{-2} S^2 r, \tag{3.2}$$

where r represents the reduced radius of the system. For equal sized grains this equals half of the particle radius, alternatively, when large particle differences are present, the radius of the smallest particle is used for r. S is defined as the surface cleanliness, which for pure particles such as those

present in SSSB surfaces approaches 1 [42].

3.5. Orbital and gravitational parameters

SSSBs vary significantly in terms of rotational period and density, the two dominant parameters dictating the dynamics at the surface of a SSSB. The gravitational attraction at the surface of an spherical, constant-density, SSSB simply follows from:

$$g = \frac{4\pi G\rho}{3}R, \tag{3.3}$$

where G is the universal gravitational constant, rho is the density of the SSSB, and R represents its radius. The rotational period will have a significant effect on the dynamics at the surface of the asteroid through the induced centripetal force which will vary as a function of its latitude δ. Assuming that the SSSB rotates uniformly about its moment of inertia at a constant rotational speed $\omega = \frac{1}{T}$, where T is the time period for a single rotation. The normal acceleration to the surface is given by $a = \omega^2 \cos^2 \delta R$ [42]. As this acceleration is by definition vectorially antiparallel to the gravitational attraction, it may be simply subtracted from Equation 3.3; leading to:

$$g_{eff} = (\frac{4\pi G\rho}{3} - \omega^2 \cos^2 \delta)R. \tag{3.4}$$

This expression shows that with a sufficiently high rotational speed, particles at the surface of the SSSB will experiment a net repulsion from the SSSB, thus setting a limit for the minimum rotational period which is only dependent on the density of the SSSB. Scheeres et al. plotted this relation for a SSSB of ρ = 2 g/cm^3, which can be seen in Figure 3.9.

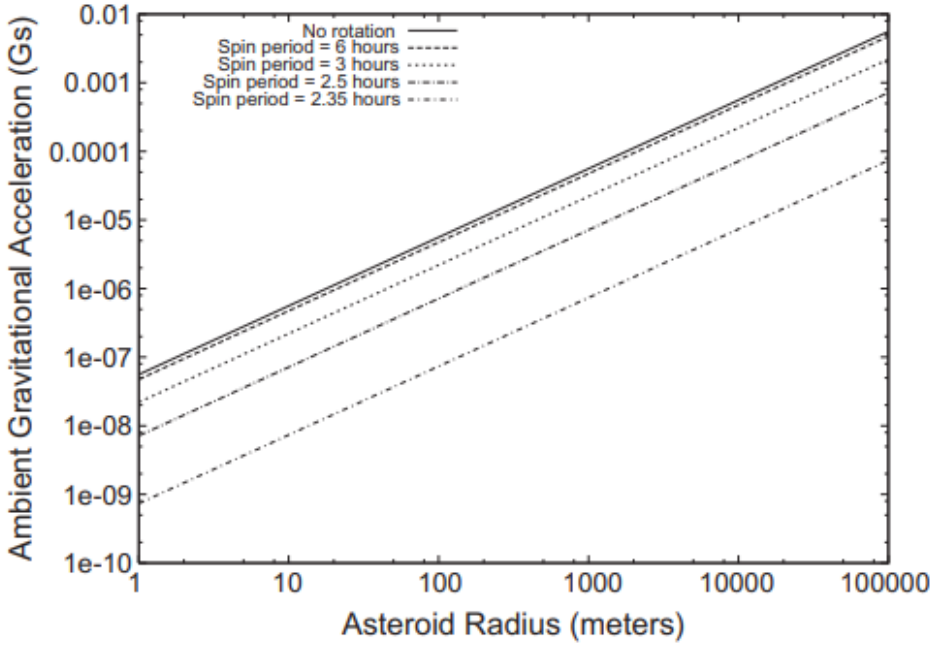

Figure 3.9: Gravitational attraction on the surface as a function of asteroid radius and rotational period (from Scheeres et al. [42]).

For this SSSB, using Equation 3.4, a minimum rotational period of 2.35 hours has been found, where the magnitude of the acceleration is then dependent on the SSSB radius. As discussed inSection 3.2, there is a correlation between the SSSB type, its orbital location, and its taxonomy in the case of

asteroids. This correlation can be seen clearly in Figure 3.10 as plotted by Lange et al., where a clear range between 0.3-4 g/cm^3 can be observed from the logarithmic plots of surface acceleration and SSSB diameter.

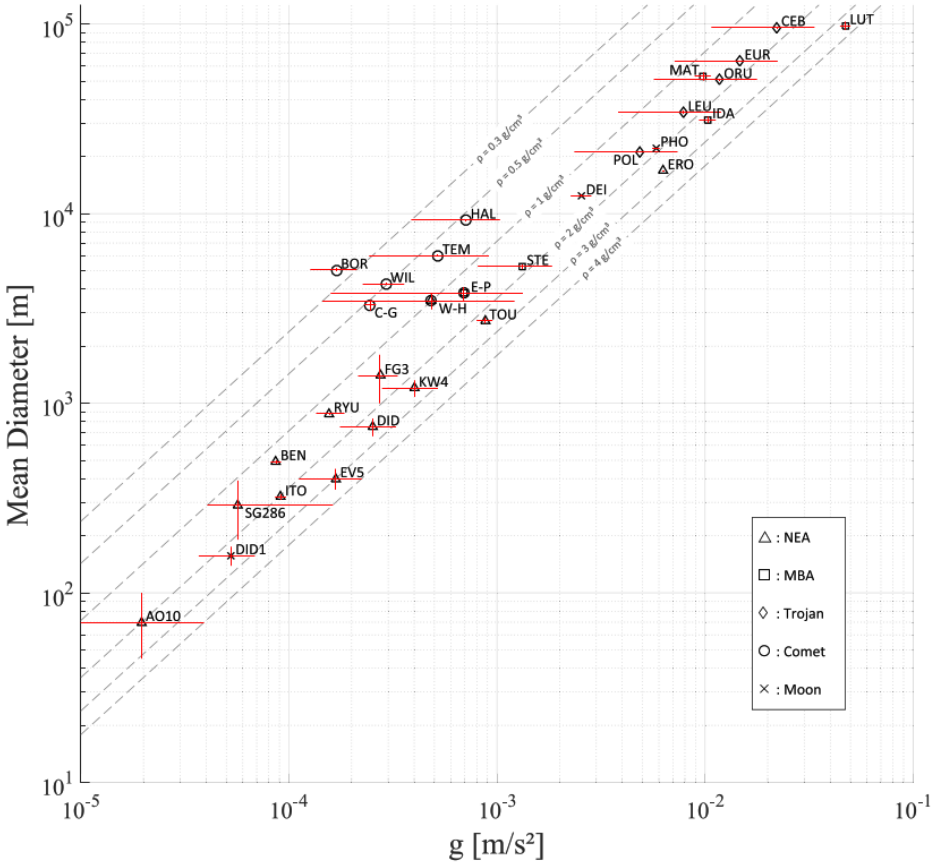

Figure 3.10: Logarithmic plots of surface acceleration vs mean diameter of different SSSBs with densities and error lines (from Lange et al. [46]).

4

Approach and landing

In order to reach the surface of a SSSB, dedicated landers are deployed from an orbiting mothership spacecraft. After deployment, which may happen from a range of orbital heights, the lander's approach ballistics will be governed by gravitational physics. As discussed in Chapter 1, some landers make use of active and passive attitude and velocity control techniques during approach. Once the lander reaches the surface of the SSSB it will most likely experience a significant rebounding motion due to the impact and the target's relatively low gravitational attraction. The magnitude of the rebounding force can also be reduced through a series of active and passive subsystems.

4.1. Orbital deployment

The lander's mission begins with its orbital deployment, after separation from the mothership. Orbital deployment is a complex and mission-critical procedure, and as demonstrated by MINERVA's failure, should not be taken for granted. Therefore, while the design of a deployment system is outside of the scope of this project, the study of this system is of value, as it will drive some of the requirements of the lander system.

The objective of the deployment system is to safely and reliably deploy the lander away from the mothership, with a predetermined speed and direction. The deployment system also comprises the securing and consequent release of the lander. This can include the severing of "umbilical connectors", wiring harnesses that transmit power and telemetry between the mothership and the lander.

As displayed in Table 1.1, landers have been deployed from a variety of deployment heights and velocities to the different targets. These heights range from tens of kilometers for Philae and NEAR Shoemaker to tens or hundreds of meters in the case of the small-scale landers like MINERVA, MINERVA-II, and MASCOT. The deployment speeds, on the other hand are consistently in the range 0.1-2 m/s.

There are several types of deployment systems with flight heritage, as detailed by Grimm et al.[47], who categorized them based on their size and standardization level. Currently, there are no standardized solutions specific to landers. However, there are significant similarities between the in-orbit deployment systems of landers and satellites, in particular CubeSats, for which standardized solutions do exist.

CubeSat deployment systems exist in a containerized form, with a rectangular container outfitted for spacecraft in the 1 to 3U size range. There are additional deployment system concepts with slightly larger form factors up to 12U; however, these have no flight heritage. Containerized systems typically operate by releasing a spring-activated plate, which pushes the spacecraft through a previously-opened hatch, while being guided by rails. The main components of P-POD, the container with most extensive flight heritage, can be seen in Figure 4.1. The kinetic energy that these systems exert on the spacecraft

is in the order of 8 J, which translates to a velocity of 1.63 m/s for a 3 kg spacecraft [48]. This is consistent with the velocities found for the lander deployments in Table 1.1.

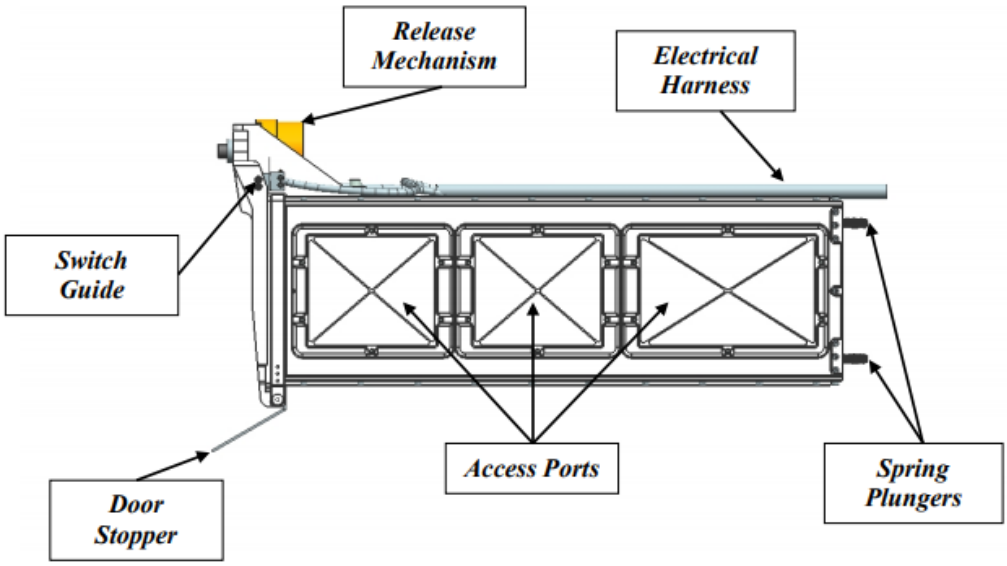

Figure 4.1: P-POD's main components (from P-POD [48]).

If the payload is larger in volume than 12U, containerized systems are no longer adequate, and spacecraft are attached to the mothership via separation rings or mounting points. These exist as standardized solutions, with notable examples being the Lightband and Kaber systems by Planetary Systems Corp and NanoRacks respectively. The Lightband separation system exists in eleven different sizes, ranging from 38.81 to 98.58 cm in diameter (of separation ring). Furthermore, its separation system can be outfitted with a variable number of separation springs, thereby being able to adapt its design for a desired deployment velocity [49].

Despite the existence of the aforementioned systems, each of the previous lander missions has made use of a customized system to deploy the lander or container vehicle. Both the MINERVA-I and MINERVA-II vehicles used the same means of deployment, which can be observed in Figure 4.2. The concept is similar to the containerized solution, with a cylindrical enclosure splitting in half, to allow the landers to be ejected by a spring-activated plate; the mass of the MINERVA deployment structure was 1.1 kg [47].

Philae, a significantly larger lander, implemented redundancies into its separation system which can be seen in Figure 4.2. The baseline system is a belt-driven spindle drive, due to its adaptable deployment speed. The backup involves a traditional spring ejection system. Philae's deployment mechanism is designed in such a way that even failures such as total motor power loss, or failure of the latch mechanism, would not stop the deployment of the lander; altogether, the deployment system weighed 7.9 kg [47].

The MASCOT lander, larger than the MINERVA rovers but significantly smaller than Philae, used a customized deployment system consisting of a container with electronic support. The system was made of an umbilical connector and three main mechanisms: a preload release, a hold-down and release, and a push-off mechanism, which can be seen in Figure 4.2. The main advantage of the MASCOT system is its low add-on system mass.

Shock is another important aspect of orbital deployment, as a measure of the acceleration the deployment system exerts on the deployed craft to reach its desired deployment velocity. Slower deployments will naturally induce a smaller shock in the lander. Depending on its severity, its effects may range from increasing uncertainties in the deployment attitude to damaging components of the landers. Therefore, a low-shock option is preferred. Grimm et al. categorized all previously described solutions as low

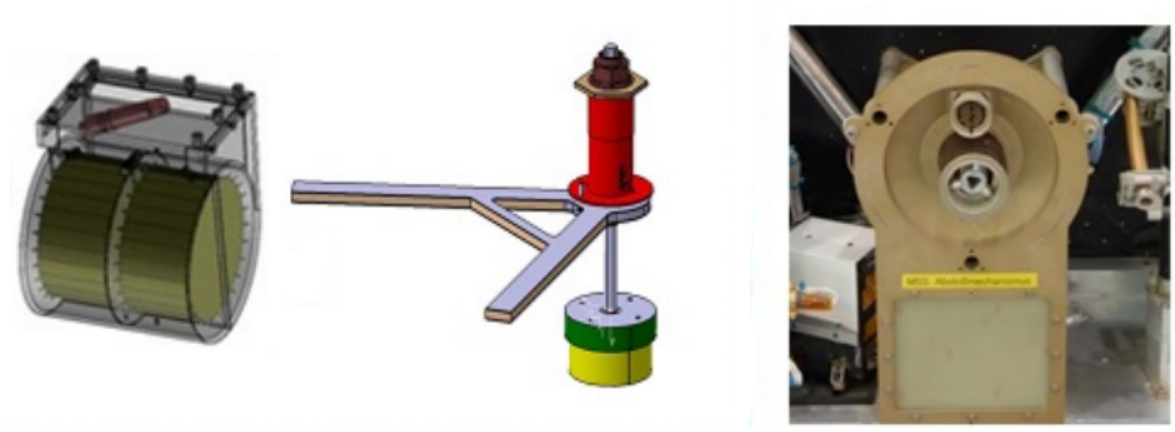

Figure 4.2: Deployment mechanisms of MINERVA (I and II) (left), MASCOT (middle) and Philae (right) (adapted from Grimm et al. [47]).

shock, except the standard CubeSat deployment unit, which was considered as having medium shock [47].

It is important to note that some deployment systems, particularly those without a rail system to guide the deployment, may introduce some unwanted motion in the lander. This might happen as the lander collides with the walls of the deployment system as was the case with MASCOT. This effect will be particularly relevant for uncontrolled landers, as they will be incapable of rectifying the undesired motion during approach. The release mechanism of MASCOT in particular induced some rotational motion and dissipated some of the push-off energy exerted by the plate. However, according to the research by Grimm et al., these contacts are predictable, and therefore can be accounted for when setting the push-off energy [47].

The deployment of the lander will have a large impact on the landing velocity, with the deployment velocity and altitude being the most dominant among the design parameters. Using the gravitational acceleration of the SSSB and the deployment height, an estimate can be made of the landing velocity. This was investigated by Lange et al. and their findings are presented in Figure 4.3. The deployment altitude was only investigated in the range of 100-1000 m. However, as shown in Table 1.1 for Philae, this may be significantly higher. For smaller bodies or low deployment altitudes, the deployment velocity is the dominant factor for determining the touchdown speed. however, this influence is reduced for more massive bodies or increased orbital heights, where the gravitational attraction plays a higher role. This is also the case for the landing uncertainty, where for low deployments the absolute error of the deployment speed can have a large influence. For MASCOT in particular, it was estimated by Lange et al. that this error could lead to an uncertainty of up to 30% on the landing zone accuracy [46].

4.2. Trajectory dynamics

The dynamics of the 2-body problem made up by the lander and the SSSB, are mainly governed by the gravitational attraction between both bodies. The initial conditions depend on the initial velocity of the mothership relative to the SSSB, and the deployment velocity exerted on the lander by the deployment system.

Muñoz et al [50], calculated the accelerations that Philae experienced during descent, as shown in Figure 4.4, accounting for 67P's central and higher order gravity spherical harmonics, coma drag, solar radiation pressure, and third-body accelerations. Only up to second-order harmonics were plotted in the figure, as higher-order terms only had a significant effect at low altitudes, therefore having little effect on the landing zone. The drag associated with 67P's coma was consistently two orders of magnitude below the gravitational attraction terms, with all remaining forces being negligible.

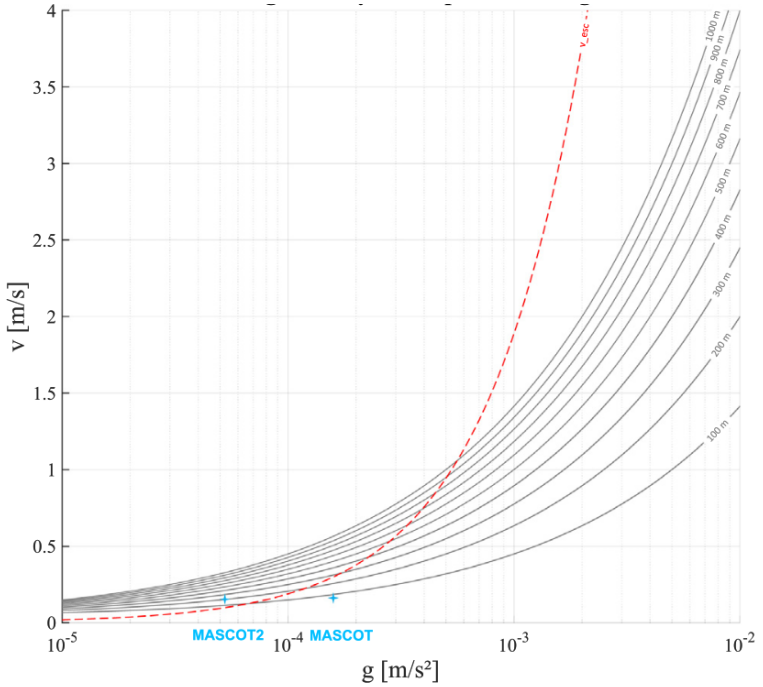

Figure 4.3: Plot of gravitational attraction (of SSSB) vs landing velocity and separation height, with escape velocity plotted in red (from Lange et al. [46]).

Dietze et al. [51] instead performed a simulation, estimating that during approach of an ellipsoidal asteroid with an equivalent-sphere diameter of 920 m, the asteroid's gravitational attraction was in the magnitude of 10^{-4} m/s^2. Solar pressure and third-body perturbations on the other hand were four and seven orders of magnitude below the asteroid's gravitational attraction respectively.

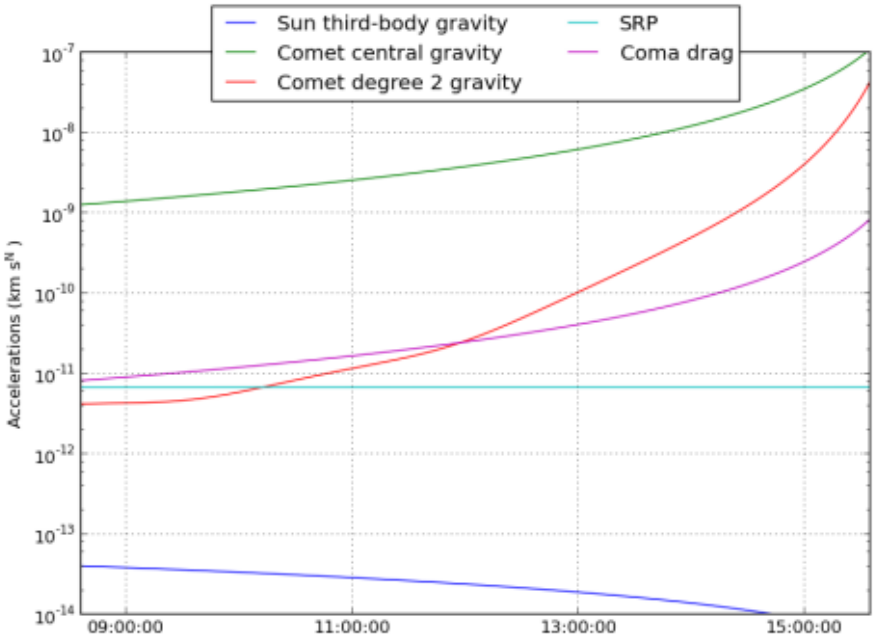

Figure 4.4: Philae's accelerations during descent (from Muñoz et al. [50]).

4.2.1. Gravitational field modelling

The SSSB's gravitational field U can be modelled using several methods: mass point cluster, spherical and ellipsoidal harmonics, and the polyhedron model. The polyhedron model was proposed by Werner and Scheeres specifically for SSSBs, as they have highly irregular shapes and consequently irregular gravitational fields. Werner and Scheeres also evaluated the polyhedron model's performance for these applications against the other classical models [52].

Mass point cluster, also known as mascon, is a direct and discrete method, which approximates the gravity of the SSSB by simulating a number of differently weighed point masses on an evenly spaced grid. The gravitation acceleration of the SSSB can the be expressed as:

$$\boldsymbol{a} = \sum_{i=1}^{N} \frac{GM_i \left(\boldsymbol{r} - \boldsymbol{d}_i\right)}{\left|\boldsymbol{r} - \boldsymbol{d}_i\right|^3}, \tag{4.1}$$

where **r** is the distance to the SSSB, $\boldsymbol{d}_i$ and M_i are the distance to the origin and the mass of individual mass concentrations respectively, with N representing the total number of mass concentrations and G the universal gravitational constant. The advantages of mascon are its simplicity, and the high degree to which the model can be adjusted, both in terms of accuracy (by increasing the number of mass concentrations), and realism (where rubble piles can be approximated with a non-uniform mascon). This model, does however have some significant drawbacks. The method's convergence is relatively slow, with increasing mass concentrations not scaling linearly with computational time. Additionally, there is no embedded collision detection within the method, which is important for landing operations, which would therefore need to be implemented. This would result in increased scripting and computational efforts [52].

Spherical, or ellipsoidal, harmonics is a modelling technique most commonly used to represent the gravitational fields of the larger objects in the solar system, such as planets. The gravitational potential is expanded into harmonic series, where the specific coefficients of each series must be determined. The gravitational field potential at a point is expressed by the following equation (from [27]):

$$U = \frac{GM_A}{r}\left\{1 + \sum_{n=1}^{\infty}\sum_{m=0}^{n}\left(\frac{r_e}{r}\right)^n P_{nm}(\sin\varphi)\left[C_{nm}\cos m\lambda + S_{nm}\sin m\lambda\right]\right\}. \tag{4.2}$$

Here r, ϕ, and λ represent the spherical coordinates of the lander, the relevant Legendre polynomials are represented by P_{nm}, with the aforementioned coefficients of the spherical harmonics portrayed by C_{nm} and S_{nm}; lastly, r_e is the radius of the reference sphere which defines the convergence domain, where the equation only converges outside this radius.

The advantages of using spherical harmonics are: they are guaranteed to converge (outside of the reference sphere radius), the expansion of the series may be truncated at any desired point to obtain a specific accuracy, and there are many examples available in literature of these methods to calculate the gravitational potential. Unfortunately, there is a series of disadvantages associated with the use of spherical harmonics. Firstly, the series coefficients cannot be derived directly, and therefore must be approximated or estimated from flight data. Additionally, as with any infinite series being modelled, it must be truncated, which means that the resulting gravitational field will always be an approximation. This truncation error grows larger the closer to the reference sphere. Furthermore, for landing applications the fact that the equations do not converge inside the reference spheroid is a significant disadvantage. Although there are techniques that can be used to mitigate this issue, they are cumbersome, as they need to be recalculated at each radius of interest. Lastly, similarly to the mascon method, there is no embedded collision detection, therefore having the same drawback of additional scripting and computational time [52].

Ellipsoidal harmonics are an attempt on improving the accuracy of the gravitational field for more ir-

regular shapes such as those that can be found on SSSBs. Ellipsoids are better at portraying the irregularities in the gravitational field, which can be calculated using the expression derived by Yu from [27] via:

$$U = GM_A \sum_{n=0}^{\infty} \sum_{m=1}^{2n+1} \alpha_{nm} \frac{F_{nm}(\lambda_1)}{F_{nm}(\lambda_e)} F_{nm}(\lambda_2) F_{nm}(\lambda_3). \tag{4.3}$$

In this equation, most terms are common with the equation for spherical harmonics, with the new terms $\lambda_{1,2,3}$ representing the orthogonal ellipsoidal coordinates, λ_e portraying the reference ellipsoid, with α_{nm} and F_{nm} showing the coefficients of ellipsoidal harmonics. Ellipsoidal harmonics share the main advantages and disadvantages of spherical harmonics but are better suited for highly irregular gravitational field; conversely, spherical harmonics will logically perform better for spheroids, providing a decreased computational time. Additionally ellipsoidal harmonics will naturally result on more tightly bounding reference volume, as shown in Figure 4.5.

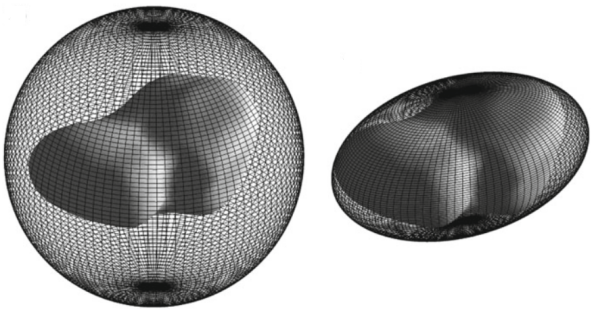

Figure 4.5: Spherical (left) vs Ellipsoidal (right) bounding areas (adapted from Yu [27]).

The polyhedron model introduced by Werner and Scheeres for use in SSSBs was initially derived for Earth geological models. This method models the asteroid as a constant density polyhedron. A polyhedron is a three-dimensional shape formed by connected two-dimensional elements (faces). The polyhedron does not have shape limitations, with craters, caves, holes, and overhangs all being valid geometries. Furthermore, the polyhedron does not have to be modelled with uniform resolution; being able to include more faces in more detailed areas without unnecessary computational expense. The expressions for the gravitational field, derived from the polyhedron method, originally derived by Werner [53] are:

$$U = \frac{1}{2} \mathsf{G}\rho \left(\sum_{e \in ES} L_e \boldsymbol{r}_e \cdot \mathbf{E}_e \cdot \boldsymbol{r}_e - \sum_{f \in FS} \theta_f \boldsymbol{r}_f \cdot \mathbf{F}_f \cdot \boldsymbol{r}_f \right), \tag{4.4}$$

$$\nabla U = -\mathsf{G}\rho \left(\sum_{e \in ES} L_e \mathbf{E}_e \cdot \boldsymbol{r}_e - \sum_{f \in FS} \theta_f \mathbf{F}_f \cdot \boldsymbol{r}_f \right), \tag{4.5}$$

and

$$\nabla\nabla U = \mathsf{G}\rho \left(\sum_{e \in ES} L_e \mathbf{E}_e - \sum_{f \in FS} \theta_f \mathbf{F}_f \right). \tag{4.6}$$

In these equations ρ represents the uniform density of the model, ES and FS are sets containing all edges and facets of the polyhedron respectively, the subscripts e and f stand for edges and facets, L_e

represents a line-integral term about an edge, r_f is the vector from r to any point of facet f, θ_f indicates the solid angle of a facet relative to the origin, and E_e and F_f are dyadics, comprised respectively of:

$$\mathbf{E}_e = \hat{\boldsymbol{n}}_{f_1}\hat{\boldsymbol{n}}_e^{f_1} + \hat{\boldsymbol{n}}_{f_2}\hat{\boldsymbol{n}}_e^{f_2}, \tag{4.7}$$

and

$$\mathbf{F}_f = \hat{\boldsymbol{n}}_f\hat{\boldsymbol{n}}_f. \tag{4.8}$$

These dyads are useful, as contiguous facets will naturally share an edge, which help with simplifying the equations. $\hat{\boldsymbol{n}}_f$ is used to represent an outwards pointing unit vector of facet f, while $\hat{\boldsymbol{n}}_e^f$ is used to represent an outwards pointing unit vector of edge e which lies on the plane of facet f. These variables are depicted in Figure 4.6 for the benefit of the reader.

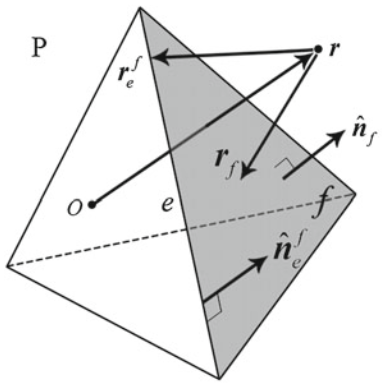

Figure 4.6: Diagram showing the variables for the polyhedron method (from Yu [27]).

One of the main benefits of using the polyhedron model is the lack of truncation errors, as the model is expressed as a finite sum. This implies that any errors will originate from the derivation of the SSSB's shape. Additionally, the model's accuracy is highly adjustable by adapting the number of facets. One other advantage is that the model is guaranteed to converge anywhere, unlike the spherical and harmonic models. Lastly, this model has an embedded methodology for collision detection, unlike the previously considered models. By definition, a spacecraft with position **r** will have entered the polyhedron when $\Omega = 4\pi$, otherwise $\Omega = 0$; where Ω represents the sum of all solid angles θ_f:

$$\Omega = \sum \theta_f. \tag{4.9}$$

The main disadvantages of the polyhedron model are its large computational expense relative to the previous models, and the fact that it requires relatively high-fidelity 3D models of the SSSBs [52].

4.2.2. Equations of motion (EOM)

The gravitational attraction that an SSSB will exert on an approaching lander will depend on the lander's three-dimensional position relative to the asteroid's inertial frame of reference. SSSBs commonly rotate about their own axes, and the lander's mothership orbit is not stationary with respect to the SSSBs frame. As discussed in Section 4.2, perturbing forces can be considered negligible, accounting for less than a hundredth of the magnitude in a worst-case scenario of a comet's coma.

The EOM for the lander acceleration due to gravity were derived by Yu [27], initially the classical expression for gravitational acceleration is introduced:

$$\frac{\mathrm{d}^2}{\mathrm{d}t^2}\boldsymbol{r} = -\nabla U. \tag{4.10}$$

Here **r** stands for the three-dimensional position of the lander relative to the SSSB's frame. $\frac{\mathrm{d}^2}{\mathrm{d}t^2}\boldsymbol{r}$ can be expressed as a relative derivative, a coordinate transformation of scales which removes units from expressions, thus making them more suitable for computer simulations [54]. Using the relative derivative, the radial acceleration term can be expressed as:

$$\ddot{r} + 2\omega \times \dot{\boldsymbol{r}} + \omega \times (\omega \times \boldsymbol{r}) + \boldsymbol{\alpha} \times \boldsymbol{r} = -\nabla U, \tag{4.11}$$

where ω and α represent the angular velocity, and acceleration of the lander respectively. Assuming that there is no variation of the angular velocity of the SSSB i.e. $\boldsymbol{\alpha} = 0$, leads to the equation of motion:

$$\ddot{r} + 2\omega \times \dot{\boldsymbol{r}} + \omega \times (\omega \times \boldsymbol{r}) = -\nabla U. \tag{4.12}$$

By defining the potential of a rotating body as V:

$$V \equiv -\frac{1}{2}(\boldsymbol{\omega} \times \boldsymbol{r}) \cdot (\boldsymbol{\omega} \times \boldsymbol{r}) + U. \tag{4.13}$$

A simplified form of Equation 4.12 can be reached:

$$\ddot{\boldsymbol{r}} + 2\boldsymbol{\omega} \times \dot{\boldsymbol{r}} = -\nabla V. \tag{4.14}$$

Equation 4.12 can be further simplified by introducing dimensionless coefficients for time and length as scalar quantities. The time scalar $[T]$, is simply defined as the rotational period:

$$[T] \equiv T_{\mathsf{A}}. \tag{4.15}$$

The length scalar $[L]$, on the other hand, uses the equivalent radius, which is the theoretical radius of a sphere with the same volume V_{A}as the SSSB:

$$[L] \equiv \sqrt[3]{\frac{3V_{\mathsf{A}}}{4\pi}}. \tag{4.16}$$

The time can then be further scaled by introducing:

$$\tau \equiv \frac{t}{[T]}. \tag{4.17}$$

Combining the scalar parameters with Equation 4.12 and Equation 4.5 leads to:

$$\tilde{\boldsymbol{r}}'' + 4\pi\hat{\boldsymbol{\omega}} \times \tilde{\boldsymbol{r}} + 4\pi^2\hat{\boldsymbol{\omega}} \times (\hat{\boldsymbol{\omega}} \times \tilde{\boldsymbol{r}}) = \kappa \left(\sum L_e \mathbf{E}_e \cdot \tilde{\boldsymbol{r}}_e - \sum \theta_f \mathbf{F}_f \cdot \tilde{\boldsymbol{r}}_f \right). \tag{4.18}$$

Here the " $'$ " and " $\sim$ " superscripts are used for the relative derivative over the newly scaled time τ, and the scaled length vectors respectively.

4.3. Active descent control

The EOM presented in Section 4.2.2 accurately reflect the dynamics of an uncontrolled lander-SSSB system. However, as described in Chapter 1, the design for Philae included both attitude and velocity control during the approach phase. Philae's attitude was passively controlled via the use of a flywheel, with an original plan to use a thruster to accelerate Philae towards the target, thus reducing the approach time. In the work of AlandiHallaj and Assadian, who modelled the dynamics of a controlled landing, the control forces and additional disturbances were simply added to the gradient of the gravitational field for a full representation of the dynamics of the EOM [55]. Combining this with the EOM derived in Equation 4.18 leads to a slightly different set of EOM:

$$\tilde{\boldsymbol{r}}'' + 4\pi\hat{\boldsymbol{\omega}} \times \tilde{\boldsymbol{r}} + 4\pi^2\hat{\boldsymbol{\omega}} \times (\hat{\boldsymbol{\omega}} \times \tilde{\boldsymbol{r}}) = \kappa \left(\sum L_e \mathbf{E}_e \cdot \tilde{\boldsymbol{r}}_e - \sum \theta_f \mathbf{F}_f \cdot \tilde{\boldsymbol{r}}_f \right) + \boldsymbol{F} + \delta\boldsymbol{u}. \tag{4.19}$$

Where **F** represents the control forces exerted on the lander and $\delta\boldsymbol{u}$ stands for the disturbances. As discussed in Section 4.2, the disturbances are several orders of magnitude below the gravitational acceleration even for a comet's coma. Therefore, assuming $\delta\boldsymbol{u} = 0$ the full EOM for a controlled lander can be expressed as:

$$\tilde{\boldsymbol{r}}'' + 4\pi\hat{\boldsymbol{\omega}} \times \tilde{\boldsymbol{r}} + 4\pi^2\hat{\boldsymbol{\omega}} \times (\hat{\boldsymbol{\omega}} \times \tilde{\boldsymbol{r}}) = \kappa \left(\sum L_e \mathbf{E}_e \cdot \tilde{\boldsymbol{r}}_e - \sum \theta_f \mathbf{F}_f \cdot \tilde{\boldsymbol{r}}_f \right) + \boldsymbol{F}. \tag{4.20}$$

The thruster onboard Philae is a cold gas thruster, fueled with nitrogen. Philae's original target (comet Wirtanen) is significantly less massive than 67P, thus presenting a much longer descent time at the same deployment altitude. The thruster is therefore pointed in the landers positive z-axis (upwards) [7]. While the thruster was not used during descent, its firing was planned to mitigate the rebounding motion, this however, failed as the gas tank never opened.

A flywheel is a mechanical system used to store rotational kinetic energy. In the context of descent control, they are used to stabilize the lander during the descent phase by rotating continuously, thus imparting a gyroscopic effect on the lander. While this will cause the lander to slowly spin along the axis of rotation of the flywheel, it is a necessary sacrifice for any lander with an orientation-dependent landing system, such as Philae's legs.

Philae's flywheel proved to be highly effective in stabilizing the lander during its descent. While no dedicated sensors for rotation frequency were onboard Philae, its rotation rate was reconstructed by Heinish et al. using measurements from CONSERT (radio experiment), ROMAP (magnetometer experiment) and the solar array power generation. Their findings can be found displayed in Figure 4.7, where the measurements from the different sensors can be found together with the inferred rotation.

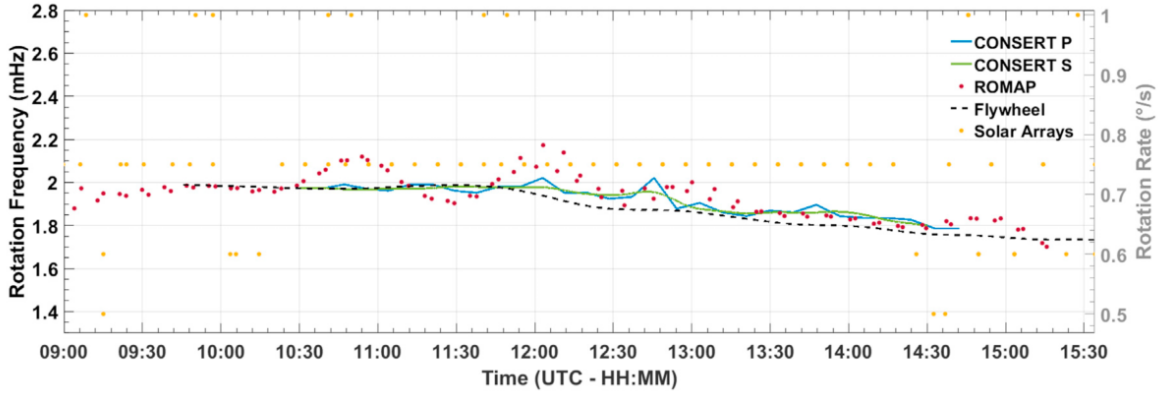

Figure 4.7: Philae's flywheel rotation rate as inferred from (non-dedicated) instruments (from Heinish et al. [56]).

Once Philae's sensors correctly determined that it impacted against 67P's surface, its flywheel was turned off. However, due to internal friction between Philae and its flywheel, some of the flywheel's momentum was transferred to the lander. This started a spin up motion which had a significant effect on Philae's trajectory after touchdown (at 15:34 UTC). This motion could be monitored by using the aforementioned procedure, for which the results are shown in Figure 4.8.

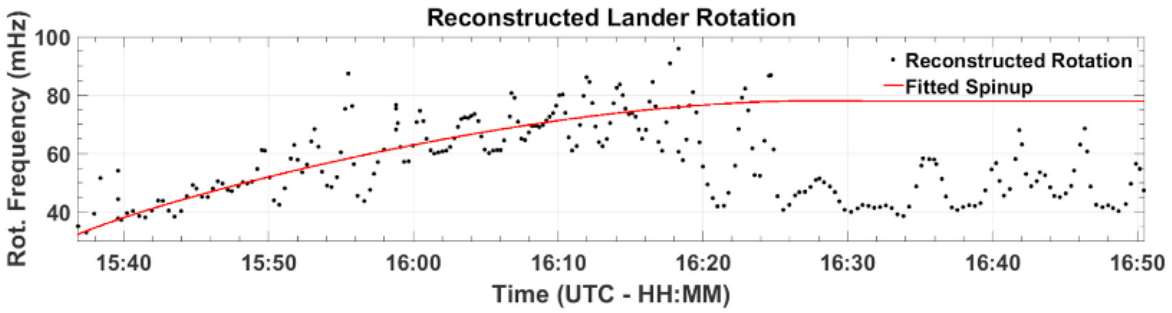

Figure 4.8: Philae's rotation rate as inferred from ROMAP and its predicted spin up (from Heinish et al. [56]).

The motion of Philae until 16:20 UTC matches its predicted rotation almost exactly. It was predicted that after the flywheel was switched off, Philae's rotational acceleration would decrease until its rotational frequency stabilized around 77 mHz. Instead, Philae's rotational frequency immediately dropped at 16:20 UTC. This, coupled with the fact that its vertical velocity stayed constant according to sensor measurements, suggests that Philae suffered a collision (and not a touchdown) against 67P. This lead to a significant attitude change and consequently meant that Philae was lost to its operators until attitude data was derived.

4.4. Landing site accuracy and selection

The dynamics of the approach trajectory have been thoroughly discussed through the chapter. The landing zone accuracy is dependent on many of the aforementioned factors, resulting from the cumulative effect of all the uncertainties and approximations of the events from deployment to landing. As these factors have an cumulative effect, those deviations happening earlier in the approach phase will have a larger influence. Therefore, an assessment of both the magnitude and timing of these uncertainties must be made.

The most significant among these is the uncertainty in the release velocity of the deployment mechanism, as it typically has a relatively large magnitude and takes place at the earliest stage. Other significant effects will be the perturbing accelerations displayed in Figure 4.4 (in order of significance): the coma drag (where relevant), the radiation pressure from the Sun, and the third-body gravity disturbances. Additionally, the inclusion of any active descent control subsystems will consequently introduce additional uncertainties associated with the hardware itself. Uncertainties in the estimation of the gravitational field will be significant when designing the mission from Earth. However, during the mission, as the mothership will orbit the SSSB, a high-fidelity model will be obtainable.

The standard technique for evaluating the landing site begins with an estimation of the uncertainties' effects, plotting a two-dimensional Gaussian probability function. This probability function can then be projected onto the surface map of the target SSSB. This results in ellipses centered around the mean landing site. The contours of the ellipses are determined using the values for three standard deviations from the center of the probability function. The value for an autonomous, hazard-avoiding lander is given by Rodgers et al. as $R_{3\sigma}$ = 10 m. An example of landing ellipses overlaid on a surface map can be seen in Figure 4.9. Here, the surface map is populated with boulders of different sizes, where the color scale in the figure indicates the dimensions of the boulder.

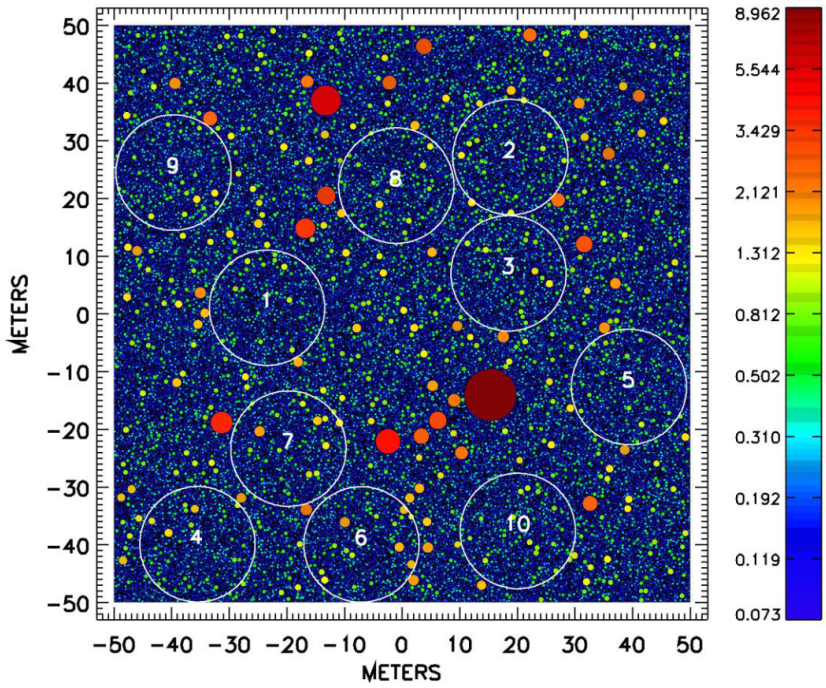

Figure 4.9: The set of the best ten landing ellipses, with the numbers representing increasing boulder cover (from Rodgers et al. [57]).

4.5. Impact velocity estimation

It is possible to quickly estimate touchdown velocities of uncontrolled landers for different bodies via a simple calculation. It can be derived starting from the law of conservation of energy:

$$E_k = E_p. \tag{4.21}$$

With the classical dynamics definitions for kinetic and potential energy:

$$E_k = \frac{1}{2}mv^2, \tag{4.22}$$

and

$$E_p = mgh. \tag{4.23}$$

Combining Equations 4.21, 4.22, and 4.23 and rearranging leads to the straightforward:

$$v = \sqrt{2gh}. \tag{4.24}$$

Where it is assumed that no mass losses are incurred during the conversion of potential to kinetic energy. However, the gravitational acceleration g is not constant, varying with the distance between the centers of gravity of the lander and SSSB:

$$g = \frac{GM}{r^2}. \tag{4.25}$$

Here G is used for the universal gravitational constant, and M for the SSSB mass. This leads to an expression for an equation for the total energy:

$$E_{\text{tot}} = E_{\text{k}} + E_{\text{imp}} = \frac{1}{2}v^2 + \frac{GM}{r}. \tag{4.26}$$

Which then leads to expressions for the energy of the lander at separation and impact:

$$E_{\text{sep}} = \frac{1}{2}v_0^2 + \frac{GM}{r}. \tag{4.27}$$

and

$$E_{\text{imp}} = \frac{1}{2}v_{\text{imp}}^2 + \frac{GM}{r_0}. \tag{4.28}$$

Here, subscripts sep and imp relate to separation and impact, with subscript 0 denoting the starting value for a specific variable. Using the law of conservation of energy again $E_{sep} = E_{imp}$ and rearranging then leads to an expression for the impact velocity of:

$$v_{\text{imp}} = \sqrt{v_0^2 + 2GM\left(\frac{1}{r} - \frac{1}{r_0}\right)}. \tag{4.29}$$

Setting $v_0 = 0$ and $r_0 \rightarrow$ inf, leads to the expression of escape velocity:

$$v_{\text{esc}} = \sqrt{\frac{2GM}{r}}. \tag{4.30}$$

Furthermore, the altitude $h = r_0 - r$ can be substituted into Equation 4.29, which when rearranged leads to the following expression:

$$h_{\text{max}} = \frac{r^2\left(v_{\text{max}}^2 - v_0^2\right)}{2GM - r\left(v_{\text{max}}^2 - v_0^2\right)}. \tag{4.31}$$

Which can be used to calculate the maximum deployment height for a maximum allowable impact velocity. This can be plotted for a specific body/lander combination, as can be seen in Figure 4.3.

4.6. Irregular touchdown

One important consideration is that the impact force may not be centered on the lander's center of gravity. This will have an impact both on energy absorption and rotational acceleration of the lander. A diagram showcasing this can be seen in Figure 4.10.

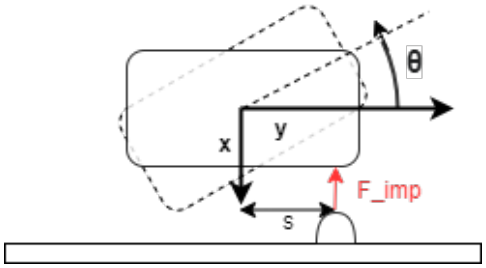

Figure 4.10: Diagram showing an uneven impact upon touchdown.

As an irregular impact may take place anywhere on the surface of the lander, the problem may be considered two-dimensional and then extrapolated for the appropriate length s. The mass distribution is a term derived by Schröder, Grimm, and Witte [58], used to describe how forces are distributed

during impact as a function of the distance between the center of gravity and the impact force, s. The overall acceleration is consistent across different impacts regardless of s. The mass distribution can be derived from simple dynamics, beginning with the initial conditions at impact where:

$$F_{\mathsf{imp}} = m \cdot a = m \cdot \ddot{x}, \tag{4.32}$$

and

$$F_{\mathsf{imp}} \cdot s = J \cdot \ddot{\theta}, \tag{4.33}$$

where J is the moment of inertia, θ is the angle between the SSSB surface and lander after impact, and the $\dot{\theta}$ and $\ddot{\theta}$ superscripts denote a derivative about time. Integrating with respect to time t and rearranging Equations 4.32 and 4.33 leads to:

$$\dot{x}(t) = \frac{F_{\mathsf{imp}}}{m} t + v_{\mathsf{x}}, \tag{4.34}$$

and

$$\dot{\theta}(t) = \frac{F_{\mathsf{imp}} \cdot s}{J} t. \tag{4.35}$$

As the lander will rotate opposite to the product of the velocity vector and distance s, an assumption can be made that $\dot{\theta}(t) = \frac{-\dot{x}(t)}{s}$. With a substitution of the expressions for linear and rotational speed obtained in Equations 4.34 and 4.35:

$$\frac{F_{\mathsf{imp}} \cdot s}{J} t = \frac{-\left(\frac{F_{\mathsf{imp}}}{m} t + v_x\right)}{s}. \tag{4.36}$$

Which can be rearranged to obtain an expression for the impact force:

$$F_{\mathsf{imp}} = \frac{-v_x}{t} \cdot \frac{1}{\frac{s^2}{J} + \frac{1}{m}}. \tag{4.37}$$

As mentioned previously, the acceleration is a constant term in this equation across impacts, and in Equation 4.37 it is represented by $\frac{-v_x}{t}$. The term for mass distribution naturally follows from Equation 4.32:

$$m(s) = \frac{1}{\frac{s^2}{J} + \frac{1}{m}}. \tag{4.38}$$

Schröder, Grimm, and Witte plotted this relation for a theoretical lander, a version of MASCOT employing an spherical shell for higher-velocity landings. Their findings can be seen plotted in Figure 4.11. Although the researchers did not provide any of the numerical values used for their calculations, the general shape of the relation $\mathsf{m(s)} \propto \frac{1}{k_1 \mathsf{s}^2 + k_2}$ can be clearly observed. The key takeaway from this mass distribution is that the highest impact forces occur when impacts go through the center of gravity of the lander. This implies that in order to optimize the impact dampening at touchdown, stronger material should be placed closer to the center of gravity, tapering-off with an increasing c-value. One consideration missing from the study is the fact that an off-center impact, with its accompanying rotation, will most likely translate to a second contact of the lander shortly after. The effects of this second contact should be further evaluated, however, this would be highly shape-dependent and therefore best estimated via direct simulation.

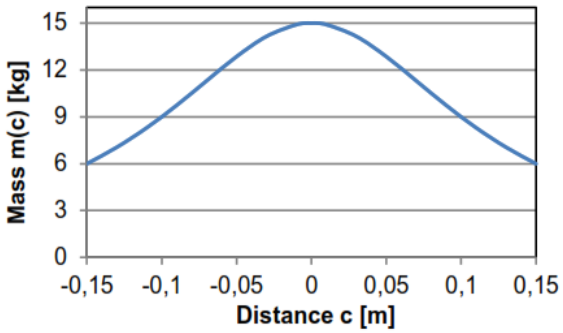

Figure 4.11: Mass distribution of a theoretical lander (from Schröder, Grimm, and Witte [58]).

4.7. Rebound

If the kinetic force of the lander multiplied by effective coefficient of restitution is larger than the gravitational force exerted by the SSSB at its surface, the lander will undergo a rebounding motion. Rebounding is an undesirable but typically inevitable motion, as the gravitational attraction at the surface of most SSSBs is low. The main concern is that the kinetic energy of the lander after the initial touchdown exceeds the escape velocity of the SSSB as given by Equation 4.30, which would result in the lander leaving the SSSB. The velocity at impact, as defined by Equation 4.29, can be controlled by adjusting the deployment velocity and altitude. Thereby ensuring that it is close or below the escape velocity, as a specific coefficient of restitution of the overall impact can not be guaranteed.

An ideal rebound on a flat surface perpendicular to the velocity vector would result in a simple parabolic trajectory of the lander post-launch, with no induced rotation of the lander. However, due to the irregular surface of SSSBs this is an unrealistic approach, where impacts will most likely be significantly irregular; thereby inducing rotational acceleration in the lander as well as multiple touchdowns in a very short time span.

In order to evaluate contact conditions against irregular surfaces covered in boulders, a multi-body simulation can be conducted. Grimm et al. conducted a series of Monte-Carlo simulations for a theoretical lander with a kinetic energy of 30.2 J using the SIMPACK tool [59]. The simulation was carried out over three previously generated $10m^2$ square areas filled with boulders following a power law boulder size distribution with varying coverage levels. Grimm et al. simulated the surface of the SSSB as a fully rigid body, with no impact absorption. This seems unnecessarily pessimistic, as even hard rock material has some degree of impact dampening, where a high coefficient of restitution could have been used instead for the surface. Their findings regarding energy after impact with a crushable impact dampening system can be seen in Figures 4.12 and 4.13.

Figure 4.12 is conclusive, with a clear trend of lower boulder coverage leading to lesser residual energy after contact. It can be seen, however that this effect is not linear, with the difference between 10 and 30% being much more significant than that between 30 and 50%. A near-linear trend can be inferred between boulder coverage and ratio of rotational over total residual energy.

Figure 4.13 clearly shows that another significant effect is the number of contacts during touchdown, which reduces the kinetic energy after impact. These contacts are only considered as being part of the same impact if the lander is simultaneously in contact with the appropriate number of surfaces; otherwise, they are categorized as separate impacts. In the figure it can be appreciated that there is a small set of single contact point impacts which result in very high residual energy values after touchdown. Grimm et al. investigated these set of simulations further, and concluded that these were the consequence of grazing shots. An example of the trajectory of such a collision can be seen in Figure 4.14.

A grazing shot takes place when the lander collides with a boulder at an large angle relative to the

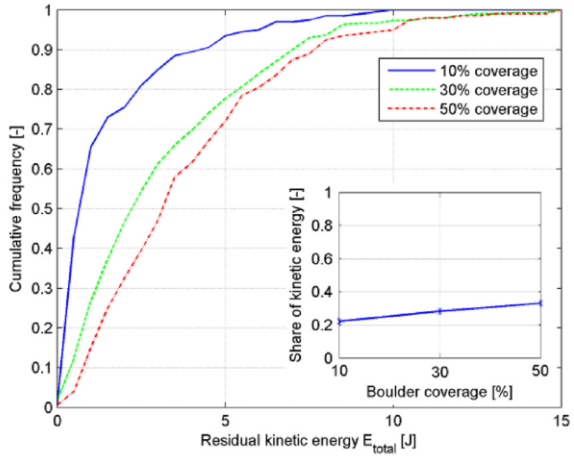

Figure 4.12: Cumulative frequency of lander energy after impact (Inlay shows the percentage of rotational energy (from Grimm et al. [59]).

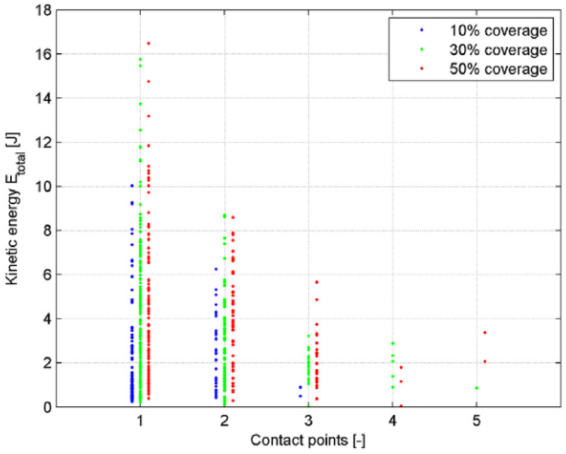

Figure 4.13: Total energy over per number of contact points (from Grimm et al. [59]).

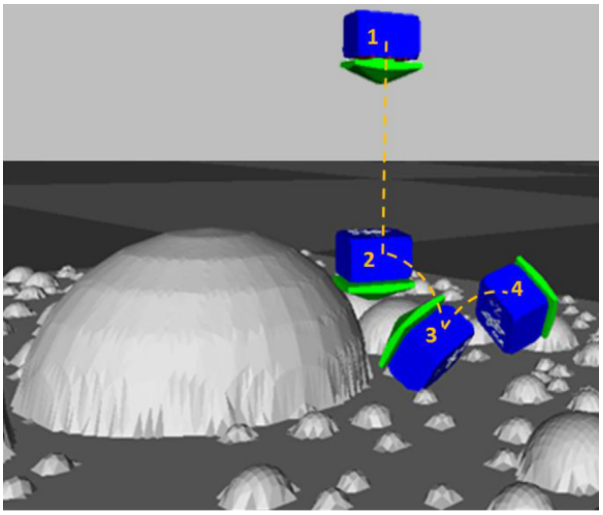

Figure 4.14: Trajectory of a grazing shot (from Grimm et al. [59]).

surface of the SSSB. This has a chance of happening when colliding against a cliff or large rock outcropping, where the surface can be at a perpendicular or even oblique angle to the surface. This is very significant for orientation-dependent dampening systems since, as displayed in Figure 4.14, it will induce large rotational velocities with only a small portion of the impact velocity being dissipated, potentially damaging the payload with a high-energy impact. Orientation independent impact dampening systems will also have an increase in rotational velocity, but the payload is omnidirectionally protected, therefore proving advantageous in this aspect. An additional mitigation strategy can be pursued by carefully selecting the landing site as detailed in Section 4.4.

The rebounding motion may be actively controlled or reduced. Active rebound control can be considered as a form of attachment subsystem, as if powerful enough, it may cancel the rebound altogether, effectively resulting in the same outcome as an attachment mechanism. Historically, the only method used for rebound mitigation has been Philae's cold gas thrusters, which were planned for firing immediately after touchdown in the direction of the SSSBs surface.

Subsequent impacts after rebounding will follow the same mechanics with a significantly lower impact speed. These impacts will most likely also have a very significant unpredictable rotational motion introduced by the initial touchdown which will hinder the performance of orientation-dependent dampening systems, and in the case for orientation-sensitive payload result in a need for an uprighting mechanism.

5

Concept generation and trade-off

Landing, for the purposes of this investigation, can be defined as coming to rest on the surface of an SSSB. It is the most critical and difficult part of the mission for the lander. Therefore, in order to fulfil its mission of delivering a payload to the surface safely, the key enabling subsystems for landing must be designed. As detailed in Section 2.3.1, there are four main functions that the landing subsystem may fulfil for SSSB missions: descent control, impact dampening, attachment, and rebound suppression. Landing on larger bodies with a significant atmosphere would additionally require heat dissipation, however, this is only the case with planets and moons which are not considered SSSBs.

From the literature studied in Chapter 1, it can be concluded that the main criterion for the landing module is reliability, as redundant hardware is non-trivial to implement. Due to this, and the inherent control delay in deep-space missions, passive systems are significantly favoured over active ones. Additionally, while some instruments, such as cameras, are orientation-independent, most scientific payloads require at least some degree of positioning. Therefore, in order to ensure versatility as a highly-adaptable lander, attitude control at rest will be a significant design consideration. Lastly, most payloads will have a maximum acceleration after which they may be irreparably damaged, therefore, effective load transfer and impact dampening are critical.

As discussed in Chapters 3 and 4, there are two significant issues when attempting to land on an SSSB: the unknown landing terrain, and the very low gravitational attraction between two small bodies. Surface properties of SSSBs vary significantly between bodies and within the SSSB itself and is the greatest unknown at the time of deployment. This, coupled with the low gravity environment makes reaching a resting position challenging due to difficulty of attachment and the low escape velocity.

In order to combat these issues, numerous landing and attachment concepts have been compiled, with varying degrees of Technology Readiness Level (TRL). The definition of TRL used for this follows the European Cooperation for Space Standardization (ECSS) International Organization for Standardization (ISO) 16290 standard which ESA uses for maturity estimation [60]. The technologies presented in this section are not exclusive to SSSB landers, where planetary and moon landers have also been taken into consideration, both due to the limited number of missions to SSSBs and the fact that their approaches may be applicable to SSSB landers. However, some concepts were discarded as they are only practical for very large impacts common to planetary landings. These include airbags, ring platform, deceleration thrusters, and the skycrane concept used for the Mars Science Laboratory. Additionally, penetrator-type landing systems such as Deep Space-2 were discarded due to the large constraints its adoption would impose on the payload; namely the huge acceleration at landing and the fact that it would have to operate below the surface [14].

5.1. Jet Propulsion Laboratory Small-Body Database

Versatility and adaptability can be very complex to estimate and measure. One possible method to effectively measure the versatility of the different concepts and adaptations is to directly calculate the operational range of a specific system. However, it is critical to measure the performance not only in terms of parameter ranges, but in terms of the complete set of SSSBs, by evaluating how many SSSBs landings a concept can achieve.

Different types of subsystems for rebound suppression, attachment, and impact dampening have been presented in Chapter 4. As discussed previously, all of these systems are versatile to some degree, and this versatility can be assessed in the context of the effective operational range. Any assessment of adaptability, on the other hand, involves a cost-to-benefit analysis, to assess whether the cost of adaptation justifies the increased versatility.

The most complete public database of SSSBs is compiled and maintained by NASA, and is available in the Jet Propulsion Laboratory (JPL) Small-Body Database Browser [61]. Here, users may search for data for specific SSSBs. Additionally, a set of APIs (Application Programming Interface) have been implemented by NASA to access and query the database with custom methods and calls. These APIs were called using a custom *Python* script, which scrapes the data and stores it to a dataframe using the *pandas* library for analysis and visualizations. The database contains data of over one million bodies; however, the degree to which information is known about each body differs. Therefore, the data must be appropriately filtered and categorized for visualization.

The integration of the database with the *Python* script allows for rapid query and evaluation of the versatility of different lander concepts. This allows for a quick evaluation of versatility for trade-offs of the different systems evaluated. The aforementioned pitfall of not focusing on certain bodies can be accounted for by specifically analysing the SSSB types which a concept could operate in. Furthermore, if the design of the lander subsystems can be scaled, and therefore parameterized, optimization algorithms can be implemented within the design process, where the script can provide a goal.

It is important to note that many important characteristics are missing from this database such as mechanical properties. Additionally, parameters such as density, gravitational attraction, and three- or two-dimensional radii are only available for a very small fraction of these bodies.

In order to assess the versatility of the different concepts at a high level of abstraction, the density of the target SSSB is useful, as it can be used as an approximation for its mechanical properties. However, this parameter is missing for several SSSBs. Due to this, the database is extended based on the spectral type of each SSSB. With the data presented in Table 5.1, a matching script iterates through the SSSB database, assigning random values for the density based on the range provided for each SSSB.

Table 5.1: Assumed densities for database (raw data from [62]).

Type	Density range [g/cm^3]	Type	Density range [g/cm^3]
S	2.01-3.39	C	0.72-2.10
X	1.00-2.98	Ch	0.60-2.80
Sq	1.97-3.59	Xc	3.87-5.39
B	1.41-2.89	Sl	2.01-3.39
V	0.85-3.00	Xk	2.61-4.97
L	2.25-4.19	Sa	0.82-1.32
K	3.33-3.75	Cb	0.69-2.19
Xe	2.26-3.56	Sk	2.01-3.39
Sr	2.01-3.39	T	0.07-5.15
A	2.33-5.13	Cgh	2.42-4.54
D	9.34-9.78	Cg	0.69-1.23
R	1.21-3.25	Comet	0.22-0.72

5.2. Impact dampening concepts

Impact dampening is one of the key functions of any lander system. As mentioned previously, the landing terrain will be unknown until the lander reaches the surface, which means that the lander must be designed for a worst-case scenario. Regarding impact dampening, the most stringent landing environment will be one where the lander impacts on a rocky surface, with a very high coefficient of restitution. Additionally, a concentrated impact over a smaller surface will be worse for any crushable structure such as a sandwich panel, which dampens impacts based on the deformation of its honeycomb mesh. If the impact takes place over a small area, only a small section of the honeycomb will deform, thus only providing limited dampening.

5.2.1. Uncontrolled impact

Despite the challenges presented by SSSB landing, some landers have relied exclusively on their structural frame to dampen the impact. This is the case, in particular, with low-altitude orbital deployments such as those carried out by MINERVA-I and -II. One major disadvantage of these low-altitude deployments is the risk that the orbiter undergoes to get close to the SSSB, where any loss of control or error could cause the total loss of the spacecraft. Furthermore, these deployments incur in significant fuel consumption and due to the endangerment of the mothership, very careful planning.

MASCOT, deployed by Hayabusa-II did not use any dedicated impact dampening systems, instead it relied on a specifically designed frame. The frame was designed as a truss, with its being providing structural support and rigidity. These beams were manufactured using CFRP foam sandwich panels, which allowed the structure to deform a few millimeters. When tested in a lab, the overall damping coefficient (the ratio between the kinetic energy after and before the impact) of the CFRP truss structure was 0.6 [46].

The main advantages of this type of impact dampening system are the reduced mass and volume and low system impact, as well as its reliability, being a fully passive system. Additionally, it is orientation-independent so not attitude control must be exerted during descent. However, this implies that unless its payload is also orientation-independent, the lander must be equipped with an uprighting mechanism. Its main drawback is the fact that its dampening effect is relatively low and can therefore only be used for low-altitude deployments.

5.2.2. Shell

This concept, with a high TRL, has been utilized on early missions to Venus and Mars. It involves the encasing of the lander inside a shell, which can be used both for impact dampening as well as heat shielding in the case of planetary landings. Typically, once the lander comes to rest on the surface of the object, the shell is ejected such that the lander can carry out payload operations. The ejection of the shell may also take place after the initial touchdown while the lander is undergoing the rebounding motion. This system was implemented in the lander probes of Venera-7 and -8, and Mars-2, -3, -6, and -7 by the CCCP. The CCCP probes had spherical shells with heat insulation material covering the exterior, while the interior was made of titanium. The Venus probes were outfitted with an internal mechanical movable damper, while the Mars probes used foam plastics which encased a spheroid made of petal-like segments. When the petals were deployed, it not only uncovered its payload, but also uprighted the probe [14].

The advantages of this system include its great impact dampening capabilities, and its orientation-independent design. However, these systems are heavy and very voluminous, and thus are better suited for large landers targeted towards large bodies. Furthermore, the ejection of the shell requires a dedicated mechanism, which negatively affects its reliability. The shell concept also has a tendency to induce a rolling motion on the lander, which can be desirable as it transforms translational into rotational motion thus reducing the rebounding motion. One drawback of the induced rolling is that it is highly unpredictable and therefore the lander may come to rest far away from the touchdown location;

therefore, introducing larger uncertainties in the final location of the lander.

5.2.3. Pallet platform

Pallet-like platforms are orientation-dependent impact landing systems. They are characterized by having a crushable structure attached to the underside of the lander. This type of system has a high TRL, as it has been used previously in the ExoMars 2016 mission, which incorporated the Schiaparreli lander. The lander made use of a combination of several of the technologies presented in this chapter, namely: a parachute, downward-pointing thrusters, and the pallet platform, as well as a detachable heat shield [63]. The pallet platform may have a wide array of shapes, which can vary from a simple prism-like extension of the lander base like the Schiaparreli lander (cylindrical) to more exotic three-dimensional convex shapes, such as those proposed by Grimm et al. which add additional thickness near the center of gravity of the lander [59]. The pallet may or may not be ejected after the initial touchdown. If it is ejected during the rebound, it may act as a hazard to the lander as they could collide.

The advantages of this system are its low mass and volume; however the requirement of an active attitude control system may offset these savings. A convex shape will induce a rolling motion on the lander, where the same advantages and disadvantages follow as from the shell concept. Additionally, the density of the honeycomb can be easily adjusted. However, there is an additional drawback, where consequent impacts can not be assumed to be dampened by the pallet as the lander's orientation will be unpredictable. As it operates as a passive system it will have high reliability, only affected by the operation and powering of the flywheel.

5.2.4. Landing legs

The most commonly used landing system are landing legs, having extensive flight heritage with planetary, moon and SSSB landers. Legs may incorporate deformable structures as feet, thereby passively dampening the impact [7]. Like the pallet platform they are orientation dependent, although due to their higher center of gravity they are less stable.

The landing leg structure is typically a truss, built using primary and secondary pillars. Primary pillars are used to withstand the main forces from the vertical impact; therefore, they are always equipped with an internal dampener. Secondary pillars, on the other hand, are used to support the lateral forces from the impact, and may or may not be equipped with a dampening system. Dampening systems within the pillars may consist of crushable structures, foam or hydraulic dampeners. Hydraulic dampeners are heavier than equivalent crushable structures, and may be affected by changes in temperature, requiring thorough sealing [14].

Typically, legged landers exist in a three- or four-legged form factor, with additional legs adding extra mass with no noticeable improvement in stability. A three-legged configuration is favoured for smaller landers due to its simplicity and reduced mass, although stability is lowered. Legs may be separated into fixed or foldable categories; with fixed legs having lower mass and increased reliability in exchange for higher volume and lowered stability. Foldable legs may be further split up into downward- and upward- deploying; where an schematic of a downward-deploying landing leg shown in Figure 5.1. Both versions employ a load limiter, which ensures that the primary pillars do not experience excessive lateral forces transmitted through the secondary pillars [14].

The advantages and disadvantages of the landing leg system depend on the specific configuration used. However, in general when compared to other systems they have high reliability while being relatively complex. Additionally they are very effective at dampening the impact while maintaining stability, due to their vertical and lateral force dampening. Relative to other systems they are highly sensitive to the angle of the impact.

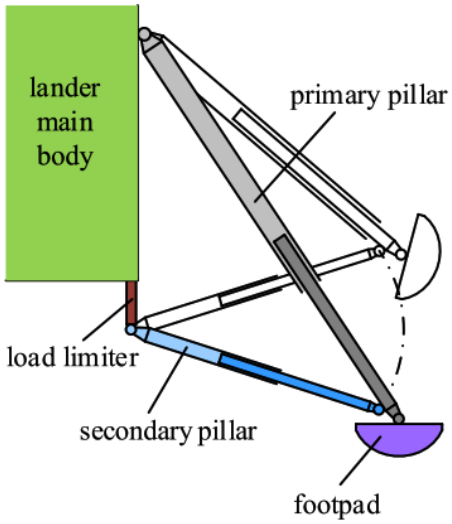

Figure 5.1: Downward-deploying landing leg structure (from Yin et al. [14]).

5.2.5. Electro-mechanical generator

Philae has been the only lander to date that has made use of a electricity generator as an impact dampening system. It is implemented as an addition to the three-legged platform and coupled to a cardanic joint to ensure that the dampening motion is fully parallel to the direction of travel, thus ensuring maximum damping. The device was the largest source of dampening during Philae's touchdown, where the honeycomb feet could have also dampened the impact sufficiently [5]. The dampener operates by having a telescopic cylinder attached to a DC brush motor through a gear set, connected via a transmission rope. When the landing platform impacts against the surface of the SSSB the telescopic cylinder undergoes compression, which turns the transmission rope, and the gear attached to the motor; which becomes a generator when attached to an appropriate resistor.

The generator concept has an advantage of transforming the impact into useful energy, and together with the cardanic joint forms a complex but robust impact dampening system. Its main drawback is that it may only be used together with a landing gear. Additionally the energy generated may not be significant when considering long term operations, with other impact dampening systems having lower mass while providing the same dampening force.

5.2.6. Granular damper

Granular dampers are containers within the lander filled with granulates. These dampen the impact via the internal collision of the granulates against the walls of the container, as well as the inter-granulate collisions, which dissipate impact energy via friction. This method has been employed in the target markers deployed by Hayabusa and Hayabusa2, used to study their deployment trajectories in order to lower the uncertainty for the deployment of the MINERVA and MASCOT spacecraft [64].

Granular dampers are both orientation-independent and fully passive systems, which are very significant advantages over other systems. However there is a very significant disadvantage to its use, where the impact dampening capabilities of the granulate are directly dependent on its mass, and therefore it is very heavy relative to other impact dampening systems.

The cushioning quilt is a multi-faceted system, oriented both towards impact dampening and attachment. A schematic of the cushioning quilt concept can be seen in Figure 5.2. It is a further development of the granular damper concept with a low TRL, as it has not been used in any lander. It uses an airbag, which forms the base for the quilt. The airbag is equipped with venting holes, where the gas within the airbag is expelled, dampening any impact. Sewn to the quilt and to each other, are sets of

granular dampers; with hooks also attached with strings to the quilt. This concept is innovative in that the quilt is deployed ahead of the lander and attached via a rope. After the quilt settles with the aid of the granular dampers, the rope is then winded to pull the quilt and the lander together. This leads to the quilt randomly grabbing unto rock cracks and irregularities on the surface with the hooks and strings, thus forming an anchor. The lander then collides against the airbag, with the impact being dampened by the expelled gases [14]. The cushioning quilt, while promising, is a relatively complex system, with many different sub-components thus lowering its reliability. Additionally, there is no guarantee that the hooks and strings attach to the surface of the SSSB or if they do, that the anchoring is of sufficient strength, particularly if the landing site is covered in regolith.

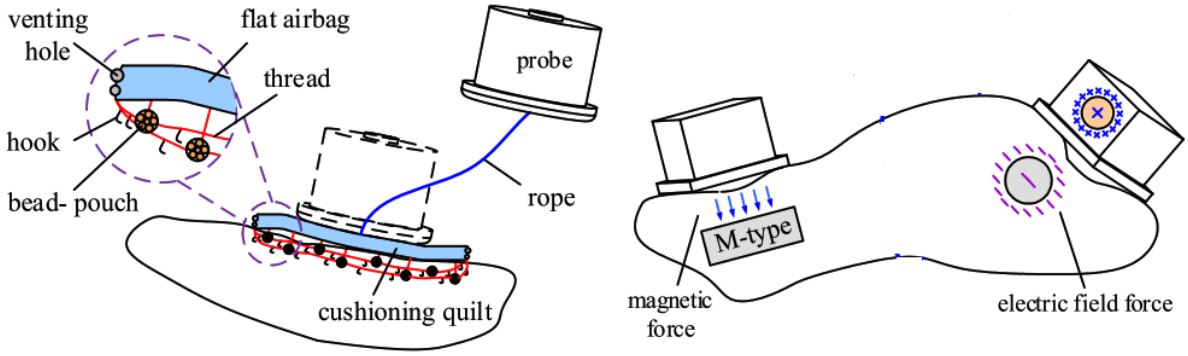

Figure 5.2: Advanced impact dampening and anchoring concepts (adapted from Yin et al. [14]).

5.3. Attachment concepts

Attachment must be completed over a wide range of surface compositions, as detailed in Section 3.4 where regolith is the most stringent, as its low mechanical strength and lack of cohesiveness makes attachment difficult. However, for penetrating concepts such as harpoons, high-strength material also must be considered, as the strength of the harpoon must be higher than the material in order to penetrate effectively. Of the missions studied in Chapter 1, only Philae planned to attach, where this failed due to the non-deployment of the harpoons.

Attaching to the surface of an SSSB is advantageous, as it minimizes the rebounding motion, severely reduces the uncertainty in the final position of the lander, and guarantees the lander's resting orientation. One drawback of attachment is that it will hinder locomotion, which if desired, will require the addition of a detachment or deployment system. Several systems can be used to attach to the surface of an SSSB, with varying degrees of TRL, and different advantages and disadvantages. These systems, and their main characteristics will be presented below.

Shape memory alloys (SMA) are materials that can be actuated using an electric charge, which increases the temperature of the SMA locally and controls its deform action. Their use has been proposed for attachment applications; however, their high temperature sensitivity makes them unsuitable for applications with large variations in temperature such as the surface of an SSSB [65]. Therefore, they are excluded from this research.

5.3.1. Ice screws

Ice screws are one of the attachment methods employed by Philae. They are located at each foot, between the two footpads as shown in Figure 5.3. The footpads are guided via a specialized mechanism unto the surface of the comet; if the material strength of the ice is low enough the ice screws may penetrate it, being drilled into the surface using a belt-transmission system. The ice screws are used in order to prevent Philae from undergoing lateral displacement as well providing frictional force for any footpad movement. Ice screws were the one attachment system that did not fail during the Philae

mission; however the limited force they could exert on the ground was not sufficient to anchor Philae [7]. Disadvantages of the ice screw system include the fact that it is an active mechanism and its performance is tailored for ice, therefore it may be suitable for some rock types but not regolith.

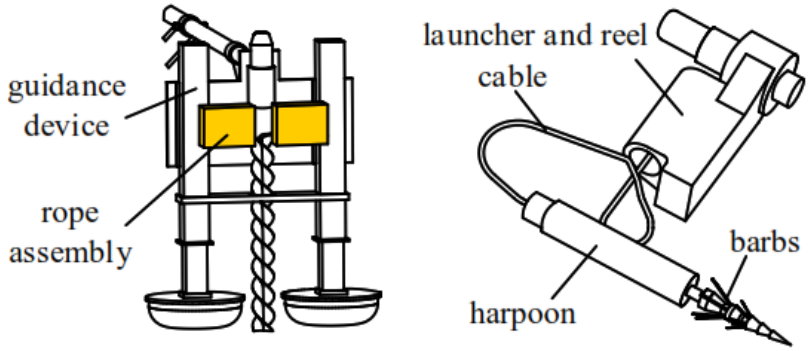

Figure 5.3: Schematics of the anchoring systems onboard Philae (adapted from Yin et al. [14]).

5.3.2. Harpoon

Harpoons are the most classical means of attachment, having flight heritage with the Phobos-Grunt and Phobos-1/2 probes by the Soviet Union as well as ESA's Philae which can be seen in Figure 5.3. They consist of a firing mechanism, a rope, and a projectile, which is usually outfitted with barbs or hooks. Harpoon assemblies may also include a reeling mechanism, equipped with a motor, which may regulate the tension in the rope.

The firing mechanism is used to accelerate the projectile towards the surface of the SSSB when it is at an appropriate distance. It may do so through the use of pyrotechnics, cold gas pressurization, spring actuation, or electromagnetic actuation. Pyrotechnics, while having high-performance, can be discarded since explosive devices can pose a risk to the mothership, and are therefore only suitable for dedicated one-off missions. Philae made use of a ignition substance (nitrocellulose) to ignite the pyrotechnics, and therefore generate enough pressure to fire its main and redundant harpoons. As detailed in Chapter 1 neither of the harpoons were successfully fired after touchdown. The company Copenhagen Suborbitals experienced a failure using the same chemical compound. Therefore, they performed tests showing that nitrocellulose did not ignite in vacuum. The danish magazine "Ingeniøren" contacted the press department of DLR, where it was confirmed that this was unknown previous to launch, but that an undisclosed solution has been found which solves the issue [66].

An important characteristic of the harpoon is that the strength of the anchoring material must be low enough for the harpoon to penetrate it, but high enough such that it offers an effective anchor. The harpoon is made to operate on rocky or icy surfaces; however it may be effective over a regolith layer. The penetration depth of the harpoon is limited by both the length of the connecting rope and the deployment energy of the projectile. Therefore, the harpoon could be effective if the layer of regolith is less deep than the penetration depth and the harpoon has still sufficient kinetic energy to penetrate the hard surface underneath.

5.3.3. Spikes

Spikes are thin elements that protrude from the structure of the lander. They aim to provide limited anchoring by penetrating soft surface material such as regolith. Once the spikes penetrate, they will resist motion through frictional forces. Additionally, spikes may be used to dampen an impact via spike deformation, following the same energy absorption mechanism as crushable structures. Spikes were included in all versions of MINERVA, as can be seen in Figure 1.1.

Spikes are fully passive elements, thereby having very high reliability. They are also relatively orientation independent, as spikes could theoretically be added on all lander edges, although this would incur in higher masses and hinder the operation of different payloads.

The main disadvantage of the spike mechanism is the low anchoring force they provide. The scalability of spikes has the issue of their large aspect ratio, where if their size is increased in order to increase the contact area, it will incur in a high volume [14]. Deployable spikes could be implemented to solve this issue, with the associated increase in mass and lowered reliability.

5.3.4. Microspine anchor

A microspine anchor was developed by JPL and presented in an article by Parness et al. [67]. The anchor was designed for robots traversing rocky surfaces, such as those seen in some planets, moons, and monolithic SSSBs. It consists of arrays of microspines (pictured in Figure 5.4) with each microspine containing its own attachment point and suspension. This enables each spine to stretch and drag such that suitable hooking points are found on the surface at the sub-millimeter level [67]. These microspines are grouped together into sets of claws, which make up the anchor. The main design goals of the anchor are to be able to resist omnidirectional forces, and be able to operate in a variety of rock surfaces. The microspines are pulled towards the center of the anchor until they are successfully hooked, therefore securing the system to the SSSB's surface.

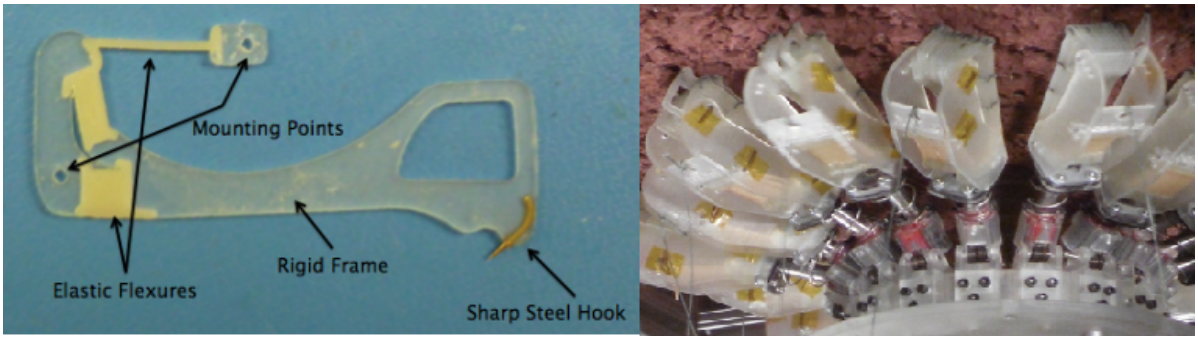

Figure 5.4: Images of the individual spine (left) and full anchor (right) (adapted from Parness et al. [67]).

The attachment capabilities of the microspine anchor on rock have been demonstrated extensively in a lab setting; however this has only been performed on rocks. As described throughout Chapter 3 regolith is present throughout different types of SSSBs, therefore the performance of this system in less cohesive materials should be evaluated. The main advantage of the microspine anchor is the lack of terrain sensitivity as the microspines can hook to any. This method, while designed for locomotion in rocky surfaces, may be adapted for a concept that can strongly anchor to rocks after impact, and perhaps provide some anchoring in regolith-covered surfaces.

5.3.5. Bio-mimetic dry adhesion

Typical adhesives are not suitable for space applications, as the extreme temperature variations on the surface of an SSSB render them unusable. Dry adhesives are bio-inspired technology from the feet of gecko which are adhere to a wide variety of surfaces regardless of surface texture and physical and chemical properties. Gecko feet have been demonstrated to reliably adhere underwater, within atmospheres of ionized air and nitrogen, as well as the vacuum of space with little to no performance degradation [68].

Gecko feet operate via two distinct adhesion mechanisms facilitated by two features: setae and scansors, which provide adhesion via van der Waals forces. Setae are long and thin micro-fibrillar structures, which are further split into nanometer-sized spatulae at the tips. The spatulae allow for surface contact

up to micron-level surface roughness. Geckos also have stiff tendon tissue in their skin which result in lamellar (radially overlapping) flaps named scansors. Scansors enable geckos to adhere to millimeter- and centimeter-scale surface roughness by draping over the surfaces, where scansors conform to surface elements without sacrificing planar stiffness [69]. Both setae- and scansor-like materials have been artificially generated in a laboratory setting via the use of carbon nanotubes, and a combination of carbon fibre fabric with an elastomer, respectively [70] [69].

Bombardelli, Broschart and Menon proposed the use of carbon nanotubes as an adhesive to successfully attach to the surface of SSSBs. This approach would cover the impact surface of the lander with thin carbon nanotube rods, which would penetrate low-strength material like regolith. The large surface contact area between the rods and the surface would translate into large van der Waals forces, and thus a high level of adhesion. Additionally, if the rods impact against a high-strength material, such as a boulder, they will buckle, behaving like a crushable structure and dampening the impact [68]. The main disadvantage of bio-mimetic dry adhesion is its low TRL, with untested performance in space applications.

5.3.6. Magnetism

As discussed in Chapter 3, some SSSBs, particularly M-class asteroids, are metallic. These asteroids are rich in iron, a strongly magnetic material. Therefore, it would be possible to outfit a lander with a permanent magnet or an electromagnet. As magnetic force follows an inverse square law with distance (like gravitational attraction), introducing a magnet is equivalent to increasing the gravitational attraction to the body, assuming that the bodies magnetic material follows the same distribution as its mass. A permanent magnet would thus accelerate the lander towards the SSSB surface during approach, increasing the impact velocity. Instead, a powered electromagnet could be triggered only after impact, thus reducing the rebounding motion, and if the magnetic force is sufficient, securely attach it to the surface of the SSSB. The electromagnet is a good attachment solution, as it is highly reliable (although it is an active solution) as well as terrain insensitive. Its main drawback is that it may only be used for M-class iron-rich asteroids. Additionally, the magnetic force may not be sufficient if the non-magnetic regolith layer is too thick, thus necessitating an additional attachment system, although the SSSB could be studied from orbit with a magnetometer previous to the deployment in order to select a suitable landing site with high ferrous content [14].

This method could be adapted for use in non-magnetic SSSBs by using electric-adsorbed landing, which involves the use of magnetically-charged projectiles fired unto the surface. The lander is then equipped with a system generating opposite charges to those on the projectiles, therefore generating an attractive force. This system presents the same disadvantages as the regular magnetic concept as the projectiles may sink too deep into the regolith layer; additionally, the targeting of the lander and projectiles are complex tasks that need to be addressed. Lastly, the inclusion of a dedicated projectile launcher will incur in mass, power, and volumetric costs, making the concept less attractive. An schematic representation of both types of landing systems can be seen in Figure 5.2.

5.3.7. Thruster

Philae made use of a cold gas thruster to try to suppress the rebounding motion. Although the thruster failed to fire, this does not mean that the idea is without merit. In fact, thrusters, should, in principle be one of the most reliable options, due to many commercial-off-the-shelf (COTS) options having extensive flight heritage. Typically, small-scale thrusters like those found in a rebound suppression manoeuvre, have been used for attitude corrections and orbital adjustments in CubeSats.

The main advantage of thrusters, when compared against the alternatives, is that they do not interact with the SSSB surface unlike drills or harpoons. Instead they operate by firing after the lander reaches the surface, therefore providing a force normal to the surface opposite to the rebounding motion. If the thrust is sufficient, this should eliminate the rebounding motion fully, although it would not fully tether the lander to the landing spot. This, however, means that the thruster is surface-agnostic, meaning

that its performance does not depend on the mechanical properties of the SSSB, an advantage which only proves more significant for a lander meant to target a wide array of SSSBs.

5.4. Surface operations

If the lander does not remain firmly anchored to its initial touchdown position, or is intended to bounce, its final attitude as it comes to rest will be unpredictable as discussed in Section 4.7. Most payloads, including critical systems such as the communications and power generation subsystems, are orientation dependent. Therefore, a self-righting mechanism should be heavily considered, either as a redundancy for an anchored lander, or as a critical system for bouncing landers. One additional advantage of the incorporation of such a system is that the self-righting mechanism may also be used for simple locomotion.

While locomotion is outside of the scope of this research, it is an important addition to the value proposition of landers, and therefore this advantage should not be discarded. Due to the low-gravitational attraction on SSSB surfaces, the normal force exerted over wheels is too low such that the friction is too low for a wheeled-drive [67]. Therefore, alternative locomotion systems have been used for SSSB operations, where the leading method is the hopping mechanism employed by MINERVA and MASCOT.

Self-righting mechanisms may be split into two main types of operation, internally and externally actuated. To date, as described in Chapter 1, two lander types for SSSBs have made use of such a system: the MINERVA rovers and MASCOT, both of which are internally actuated.

Externally actuated mechanisms follow the ”arm” concept displayed in Figure 5.5. Arms are placed on two opposing faces on the exterior of the lander, connected via a shaft, which ensures that any movement made is consistent across the arms. The shaft is driven by a motor which can run at an adjustable rpm, with slow rotational speed used for self-righting motion and faster rotation to enable hopping locomotion.

Externally actuated self-righting mechanism allows for simpler motor and controller design, which translates to increased hardware reliability. However, its operational reliability is lower, as the arms may get stuck within crevices. Furthermore, the contact points of the arms may differ significantly, where one rests on regolith and another on a boulder. If this happens, the motion of the lander will be unpredictable and highly irregular, making the hopping dynamics more difficult. Additionally, this concept is significantly more voluminous.

Examples of an internally activated mechanism can be seen in Figure 5.5, as well as previously in Figure 1.1. There are three main concepts with a very high TRL as they have been demonstrated by MASCOT and MINERVA-I and -II. These are based on the same operating principle, with a motor rotating an internal mass, which due to Newton’s third law will result in a reaction force exerted on the lander. The main advantage of this type of system is that it is independent of surface conditions, and therefore has an increased operational reliability.

MASCOT uses an eccentric arm with a mass concentrated at its tip; this arm is rotated and suddenly stopped, which generates an off-center reaction force. This sends the lander in an uncontrolled hop, with a maximum range of 20 meters. The initial MINERVA rovers used a combination of a torquer and a turntable to achieve direction-controlled hopping; however, the turntable was removed in the following iteration for MINERVA-II as the mass was found to be too large. MASCOT’s system generates a significantly larger force relative to its size than the system used by MINERVA; therefore it is the preferred option for larger landers carrying a significant payload [9].

One additional challenge affecting surface operations is the location of the lander at impact, particularly if this surface is not illuminated. This is more critical for landers that do not anchor to the surface of the SSSB as their resting position will be hard to predict. For this purpose, light-emitting diodes can be attached to the lander, such that it is more visible from orbit.

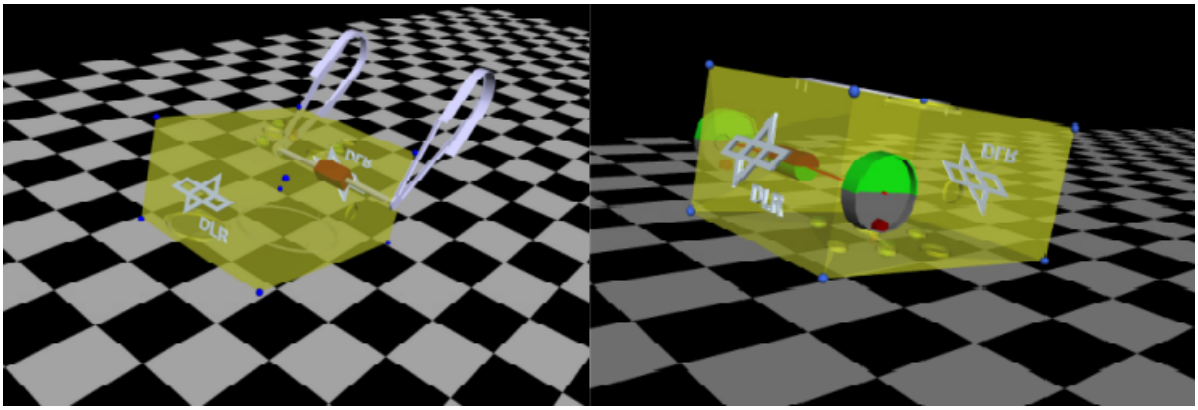

Figure 5.5: Externally and internally actuated mobility concepts for MASCOT (adapted from Dietze et al. [51]).

5.5. Concept population

The concept of a space lander has been theorized, planned, and implemented in a multitude of ways. As detailed in Chapter 1 even SSSB landers, which operate in relatively similar environments, have made use of different (or no) impact dampening and attachment technologies. In order to fulfil these functions, concepts have been drawn from literature with six impact dampening concepts and seven attachment concepts. Accounting for all possible combinations, this results in 42 different possible concepts, without taking into account systems employing a combination of subsystems for the same task to achieve redundancy, such as Philae. As each concept would require detailed research and assessment for a trade-off, the number of concepts must be reduced.

Rather than exhausting every possible combination, concepts can be created by categorizing and sorting the different subsystems, through the use of concept trees. These trees branch with the orientation-dependence of the subsystems and whether the subsystems are active or passive. The concept trees can be seen in Figure 5.6 and Figure 5.7.

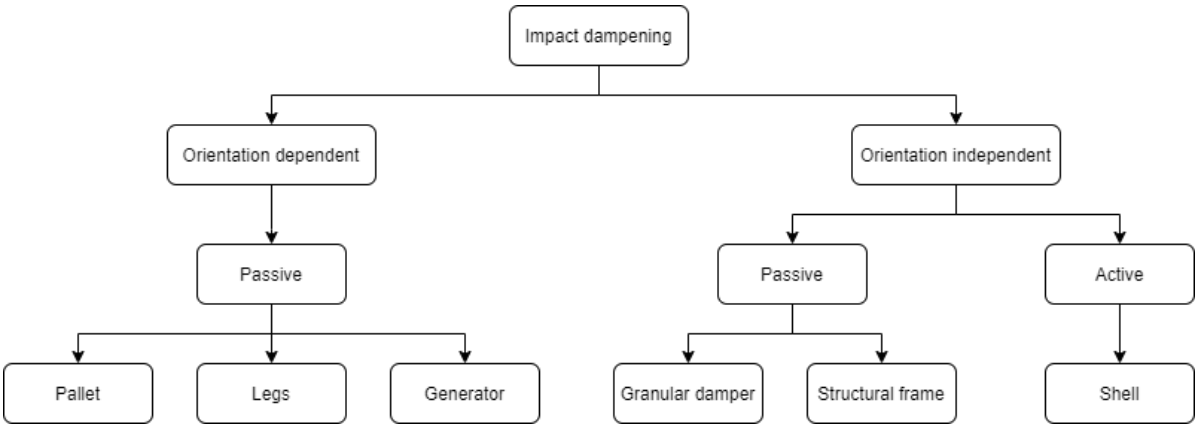

Figure 5.6: Impact dampening concept tree.

The orientation of the lander can be controlled via the use of a single flywheel or a set of reaction wheels depending on the degree of control desired. This control is necessary for some subsystems and payloads, such as a harpoon, which must fire in the direction of the target SSSB, and is a significant advantage for scientific payloads. However, this comes with a significant increase in mass and a decrease in overall reliability. Therefore, this is considered as a good separator through which the key enabling subsystems can be merged to form a concept.

Concepts then may be generated by exhausting all possible combinations of impact dampening and attachment mechanisms under the same orientation dependency branch. It is important to consider

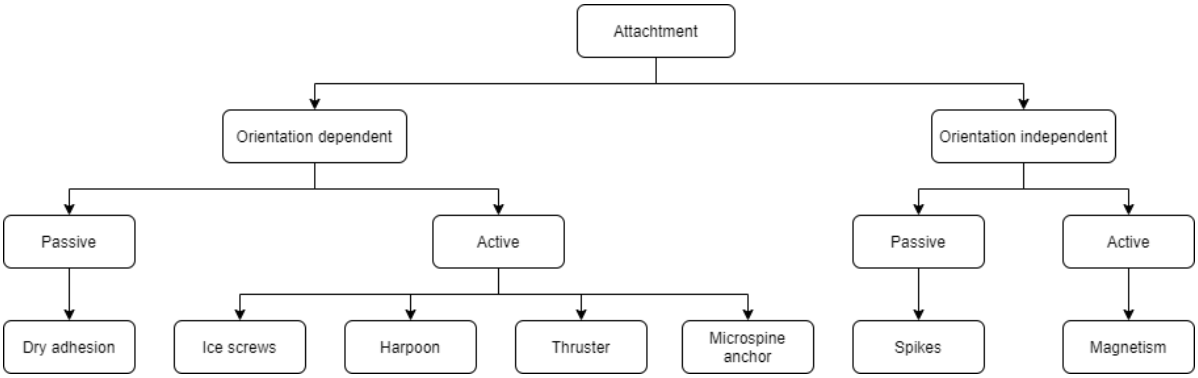

Figure 5.7: Attachment concept tree.

that the generator impact dampening system, due to its nature, must be paired with either the legs or the pallet, as there must be a joint between the lander and the landing gear for the generator to act. Consequently, a number of impact dampening concepts combine the pallet or the legs with the generator.

While concepts could be further segregated by the next level in the concept trees, active and passive systems may coexist within the same concept; with each subsystem offsetting reliability issues and performance within the concept. Furthermore, although the implementation of key enabling subsystems tends to be positive, it also comes with increased mass and lowered reliability. In fact, it could be the case that the implementation of a subsystem does not come with a justifiable performance improvement. Therefore, for both the subsystems one of the options considered is to not add one of the subsystems to the concept; resulting in the concept only having an impact dampening or an attachment subsystem. After the concept tree segregation, this procedure resulted in the generation of 32 concepts.

5.6. Killer requirement

In order to lower the number of concepts to a manageable level, a killer requirement was defined. SSSB landers have found mixed success in their operation; with varying levels of failure ranging from subsystem to total failure. Therefore, the reliability of the system is considered as an appropriate killer requirement.

The reliability of a theoretical concept cannot be assessed traditionally via the number of failures. Additionally, for those concepts which have been used, the extremely limited amount of data points would render this exercise futile. Therefore, an operational reliability parameter was developed for all concepts, aiming to assess the likelihood of the system operating according to the specifications.

The operational reliability parameter is calculated using: the TRL, whether the system is active, and the level of complexity for both the dampening and attachment systems making up each concept. These inputs are normalized to a percentage of the maximum score for complexity and TRL, while a binary score of 1/0 is given for passive/active systems respectively. These criteria are then weighted with a bias, including an additional bias for the importance of attachment over impact dampening systems. The scores each concept received for the operational reliability, together with all relevant inputs can be seen in Table 5.2. Additionally, the values used for the biases can be seen in Table 5.3.

The TRL scores and the distinction between passive and active systems are relatively trivial to evaluate, however, the complexity of the system required further assessment. This was evaluated as the mechanical complexity of the system. The only system that received a score of 0 was the lack of an attachment system. Purely rigid structural assemblies, such as the spikes, structural frame, pallet, and granular damper received scores of 1. A score of 2 was given to the legs, magnet and the cold gas thruster, as they are relatively simple mechanical assemblies. Due to the need of a driving mechanism, the generator, shell, ice screws, and harpoon were given scores of 3. The only subsystems receiving

higher scores were the microspine anchor and the dry adhesive, with scores of 4 and 5 respectively. The microspine anchor received this score due to the many different, independently-moving anchors; while the dry adhesive was given the highest score due to the issues in manufacturability.

Table 5.2: Operational reliability assessment of the 32 concepts (indexes 1 and 2 are used for the impact dampening and attachment subsystems respectively, comp. is an abbreviation for complexity).

Impact dampening (1)	Attachment(2)	TRL 1	TRL 2	Passive/Active 1	Passive/Active 2	Comp. 1	Comp. 2	Operational reliability
Pallet	None	9	9	Passive	Passive	1	0	4.30
Pallet	Dry adhesion	9	4	Passive	Passive	1	3	3.72
Pallet	Ice screws	9	9	Passive	Active	1	3	3.50
Pallet	Harpoon	9	8	Passive	Active	1	2	3.54
Pallet	Microspine anchor	9	6	Passive	Active	1	5	3.13
Pallet + Generator	None	9	9	Passive	Passive	4	0	3.70
Pallet + Generator	Dry adhesion	9	4	Passive	Passive	4	3	3.12
Pallet + Generator	Ice screws	9	9	Passive	Active	4	3	2.90
Pallet + Generator	Harpoon	9	8	Passive	Active	4	2	2.94
Pallet + Generator	Microspine anchor	9	6	Passive	Active	4	5	2.53
Legs	None	9	9	Passive	Passive	2	0	4.10
Legs	Dry adhesion	9	4	Passive	Passive	2	3	3.52
Legs	Ice screws	9	9	Passive	Active	2	3	3.30
Legs	Harpoon	9	8	Passive	Active	2	3	3.24
Legs	Microspine anchor	9	6	Passive	Active	2	5	2.93
Legs + Generator	None	9	9	Passive	Passive	5	0	3.50
Legs + Generator	Dry adhesion	9	4	Passive	Passive	5	3	2.92
Legs + Generator	Ice screws	9	9	Passive	Active	5	3	2.70
Legs + Generator	Harpoon	9	8	Passive	Active	5	2	2.74
Legs + Generator	Microspine anchor	9	6	Passive	Active	5	5	2.33
Pallet	Cold gas thruster	9	9	Passive	Active	1	2	3.60
Pallet + Generator	Cold gas thruster	9	9	Passive	Active	4	2	3.00
Legs	Cold gas thruster	9	9	Passive	Active	2	2	3.40
Legs + Generator	Cold gas thruster	9	9	Passive	Active	5	2	2.80
Granular damper	None	7	9	Passive	Passive	1	0	4.58
Granular damper	Spikes	7	9	Passive	Passive	1	1	4.48
Granular damper	Magnetism	7	7	Passive	Active	1	2	3.77
Structural frame	None	9	9	Passive	Passive	1	0	4.80
Structural frame	Spikes	9	9	Passive	Passive	1	1	4.70
Structural frame	Magnetism	9	7	Passive	Active	1	2	3.89
Shell	Spikes	9	9	Active	Passive	5	1	2.90
Shell	Magnetism	9	7	Active	Active	5	3	2.19

Table 5.3: Modifiers used for the calculation of operational reliability and variation used for sensitivity analysis.

Modifiers		Variation
Orientation bias	0.5	0-2
TRL bias	1	0.1-2
Passive bias	1	0.1-2
Complexity bias	1	0.1-2
Att:Damp bias	0.5	0.1-1
Score Threshold	70%	70-95

Following that, the maximum possible score for operational reliability is established. Then, a minimum threshold is set such that concepts below this score are filtered out. A threshold of 70% of the maximum score is established as the killer requirement. This results in a reduction in number of concepts to 15 from the original 32.

One positive sign is the fact that both the MASCOT and MINERVA concepts, as detailed in Chapter 1, are not filtered out by the killer requirement, which leads some credence to the procedure. Furthermore, while no concept truly represented Philae due to the numerous redundant systems present on-board, all of its individual components, namely legs, generator, ice screw, and harpoon, successfully cleared the threshold as part of winning concepts.

Despite this, further investigation on the reliability of the operation is merited. For this reason, a sensitivity analysis was performed in order to verify the results. Variations were introduced in the bias modifiers, as well as in the minimum score threshold as presented in Table 5.3. A script was implemented which calculated the operational reliability for each concept, using all possible combinations of the bias variations; with each bias having 10 steps between their maximum and minimum values. If

the concept surpassed the given threshold it was tallied as a win for that concept, with the win totals presented in Figure 5.8; where the concepts not meeting the killer requirement are displayed in red.

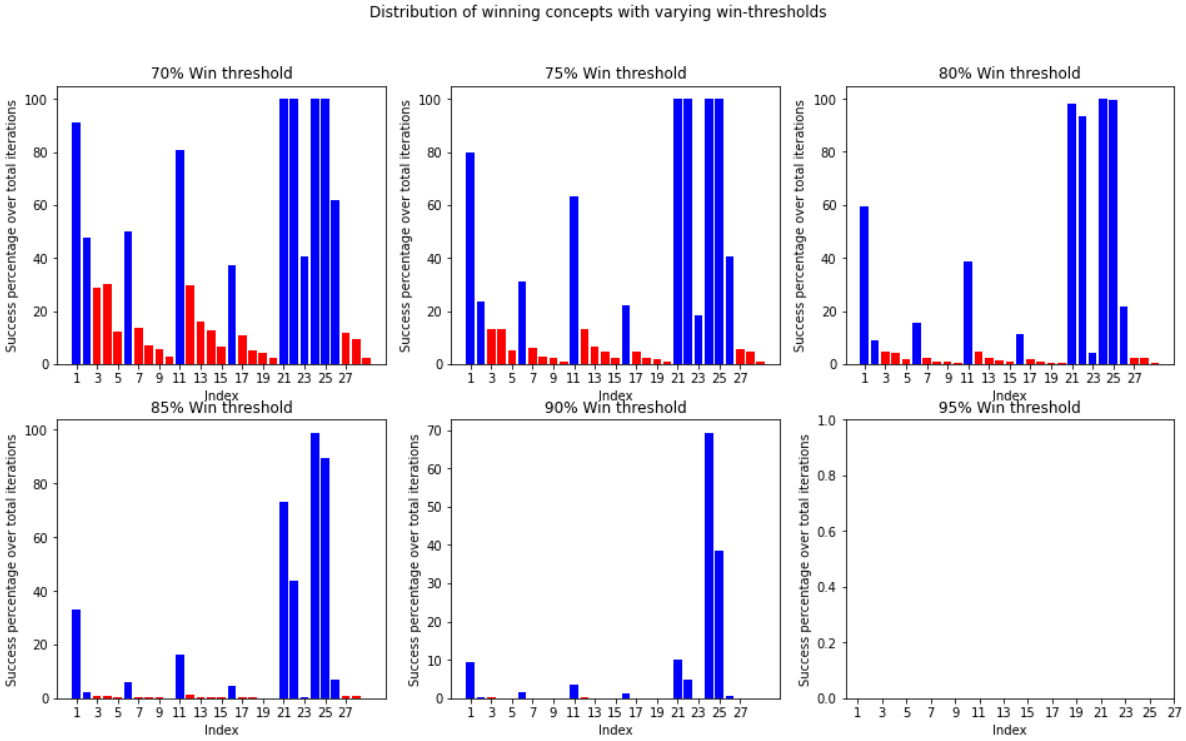

Figure 5.8: Histogram of winning concepts from sensitivity analysis, concepts not meeting the killer requirement are displayed in red.

The results are conclusive, with all the initially winning concepts having the highest scores regardless of win threshold. The difference, while not necessarily significant at a 70% win threshold, is more pronounced as the win thresholds increase.

5.7. Concept trade-off

With the number of concepts significantly reduced via the killer requirement, they may now be assessed based on a set of criteria, such that a winning concept may be selected and designed in further detail. The criteria are then weighted based on the AHP, with the winning concept receiving the highest overall score.

5.7.1. Criteria and scores

In order to evaluate these concepts, a number of criteria must be selected. It is important that these criteria both reflect the design priorities, and that they can be reasonably assessed without guesswork.

The criteria selected for the trade-off are: mass, operational range, operational reliability, adaptability, positional assurance, and TRL.

Mass is perhaps the single universal criterion used in trade-offs for space missions. Every kilogram of mass sent onboard a space mission is costly, both in terms of required fuel as well as opportunity cost, particularly for deep-space missions such as the ones required for SSSB exploration. Mass is assessed at a component level, where estimates from the literature in Section 5.2 and Section 5.3, are used for each subsystem making up the concept. It is important to note that all orientation-dependent concepts receive a penalty in this criterion, as the mass of an stabilizing flywheel is added to the design.

Operational range is key to an effective lander design, which is able to operate within a range of SSSB. It may also be understood as a measure of versatility. The operational range of the different concepts is again evaluated at a component level, where each subsystem enables the lander to operate in different SSSBs. This criterion is assessed using a custom *Python* script, embedded with the extended JPL database described in Section 5.1. The values used to evaluate the versatility of the subsystem are obtained from the literature in Section 5.2 and Section 5.3; then, the concept as a whole is given a percentage score of the number of SSSBs which can be fulfilled by this concept, over the total number of SSSBs in the database. For the impact dampening systems, the value used to estimate operational range is based on the coefficient of restitution of each subsystem. On the other hand, for the attachment subsystem the surface's mechanical properties are required. This is an issue, as these parameters are not known for any non-visited SSSBs which makes up the large majority of the database. For this reason, a false equivalence is made between SSSB bulk density and soil strength, based on equivalent percentiles. As discussed in Section 3.4, these parameters are effectively linked through the SSSB's macroporosity, thereby providing the closest estimate for this purpose.

As detailed in Section 5.6, operational reliability is a parameter aiming to assess the likelihood of the concept successfully fulfilling its purpose was created. This parameter can be further used as a criterion for the trade-off, as reliability is also a near-universal criterion in the evaluation of space systems.

One of the design philosophies used throughout the design of the lander is adaptability. Adaptability, in the context of a SSSB lander, aims to measure how easily the design of the subsystem can be adapted such that its operational range is expanded. This parameter is extremely hard to calculate effectively, therefore, instead a tiered score is given based on the highest tier that the subsystem meets. The tiers range from 0 to 5; the tiers and the description of each tier can be seen in Table 5.4. While adaptability is scored at a component level, the score for each concept is based on the highest performing subsystem making up the concept.

Table 5.4: Score tiers for adaptability criterion.

Tier	Description
0	The system cannot be adapted to expand its operational range
1	The lander must be re-designed in order to expand its operational range
2	The system must be adapted previous to launch, the adaptation is significantly harder to implement than the original solution
3	The system must be adapted previous to launch, the adaptation is as simple as the implementation of the original solution
4	The system must be adapted previous to launch, the adaptation is simpler than the original implementation
5	The system can be adapted after launch

Positional assurance is also evaluated using a tiered list varying from 0 to 5. Each tier with its corresponding descriptor may be found in Table 5.5. Positional assurance aims to capture how much control can be exerted over the final location and orientation of the concept after the landing phase, including the possible rebounding motion. Knowing the resting location of the lander can prove extremely challenging if the rebound is not suppressed. Furthermore, most scientific payloads must be oriented in a specific way or aimed towards a specific feature; if the orientation of the system can not be controlled, a self-uprighting mechanism may be required, or the range of serviceable payloads will be lowered significantly. Positional assurance is assessed at a concept level.

Table 5.5: Score tiers for positional assurance criterion.

Tier	Description
0	The system's final orientation and location are completely undetermined
1	There is some degree of control over the system's final orientation or location
2	There is some degree of control over the system's final orientation and location
3	The system's final orientation and location can be controlled
4	The system's final orientation or location can be assured
5	The system's final orientation and location can be assured

Lastly, TRL follows from the ECSS ISO 16290 standard which ESA uses for maturity estimation [60]. The different TRLs together with their descriptors may be found in Table 5.6. For the purpose of this trade-off and such that it does not overlap with the operational reliability criterion, TRL is assessed on the concept as a whole.

Table 5.6: TRL levels following ISO 16290 (from ESA [60]).

TRL	Description
1	Basic principles observed and reported
2	Technology concept and/or application formulated
3	Analytical and experimental critical function and/or characteristic proof-of-concept
4	Component and/or breadboard functional verification in laboratory environment
5	Component and/or breadboard critical function verification in relevant environment
6	Model demonstrating the critical functions of the element in a relevant environment
7	Model demonstrating the element performance for the operational environment
8	Actual system completed and accepted for flight (”flight qualified”)
9	Actual system ”flight proven” through successful mission operations

Following the classic trade-off methodology, each of the 15 concepts receives a score for each criterion. These scores are presented in Table 5.7.

Table 5.7: Concept scores for each criterion.

Concept	Mass [kg]	Operational range [%]	Operational reliability	Adaptability	Positional Assurance	TRL
Pallet	1.33	86.4	4.30	4	1	9
Pallet with Dry adhesion	1.43	88	3.72	1	3	4
Pallet with Ice screws	3.13	92	3.50	4	5	9
Pallet with Harpoon	2.03	92	3.54	4	5	8
Pallet with Cold gas thruster	3.13	93.5	3.60	5	5	8
Pallet + Generator	2.83	87.69	3.70	4	2	8
Legs	2.73	87.69	4.10	4	1	9
Legs with Dry adhesion	2.83	91.45	3.52	3	3	4
Legs + Generator	4.23	93	3.50	4	2	9
Granular damper	3	82	4.58	3	0	7
Granular damper with Spikes	3.1	84	4.48	3	1	7
Granular damper with Magnetism	3.5	82	3.77	3	5	7
Structural frame	0	81	4.80	1	0	9
Structural frame with Spikes	0.1	82.5	4.70	1	1	9
Structural frame with Magnetism	0.5	81	3.89	1	5	7

5.7.2. Criteria weights

The criteria weights were determined using the AHP. AHP involves the pair-wise comparison of each combination of criteria, where the score in each matrix row represents how many times more important the concept in the row is than the concept in the column for the purposes of the investigation. The AHP carried out for the criteria evaluated can be seen in Table 5.8, with the first six columns making up the matrix, and the last indicating the resulting criteria weights.

Table 5.8: AHP pairwise comparison and resulting criteria weights (criteria names on top row are shortened for readability).

Criteria	Mss	Rng	Rel	Adp	Pos	TRL	Criteria Weights
Mass	1	0.5	1	1	2	2	0.15
Operational range	2	1	2	2	5	2	0.32
Operational reliability	1.0	0.5	1	1.5	2	1	0.17
Adaptability	1	0.5	0.67	1	2	0.5	0.14
Positional assurance	0.5	0.2	0.5	0.5	1	1	0.07
TRL	0.5	0.5	1	2	1	1	0.15

Following the AHP as devised by Saaty, a consistency analysis must be performed in order to ensure that the prioritization values are consistent across the AHP matrix. In order to do this a consistency index (CI) value must be calculated using the following equation derived by Saaty [71]:

$$\mathrm{CI} = \frac{\lambda_{max} - n}{n}, \tag{5.1}$$

where λ_{max} represents the maximum eigenvalue of the matrix and n is the number of criteria being analyzed (or the matrix’s order). From the AHP performed for the lander, a CI of 0.0513 is obtained.

According to Saaty, for an acceptable pair-wise comparison, the consistency ratio (CR) of the AHP must not exceed 0.1, else the AHP must be repeated. CR originates from the ratio between the CI and the random index (RI). The RI is a value gathered from literature, which represents the CI for a randomly filled AHP. The RI depends on the matrix order; following Saaty's research, for an order of 6 it is equal to 1.24 [71]. This results in an overall value of CR of 0.0414 for the AHP, well below the 0.1 threshold, meaning that the AHP is indeed consistent.

With the obtained criteria weights following the AHP, the final scores for the different concepts can be obtained. These are showcased in Table 5.9.

Table 5.9: Weighted scores for each criterion and final score for each concept.

Concept	Mass	Operational range	Operational reliability	Adaptability	Positional Assurance	TRL	Final Score
Pallet	0.686	0.432	0.615	0.750	0.200	1.000	0.612
Pallet with Dry adhesion	0.662	0.560	0.171	0.000	0.600	0.000	0.353
Pallet with Ice screws	0.260	0.880	0.000	0.750	1.000	1.000	0.648
Pallet with Harpoon	0.520	0.880	0.034	0.750	1.000	0.800	0.664
Pallet with Cold gas thruster	0.260	1.000	0.077	1.000	1.000	0.800	0.705
Pallet + Generator	0.331	0.535	0.154	0.750	0.400	0.800	0.500
Legs	0.355	0.535	0.462	0.750	0.200	1.000	0.569
Legs with Dry adhesion	0.331	0.836	0.017	0.500	0.600	0.000	0.437
Legs + Generator	0.000	0.960	0.000	0.750	0.400	1.000	0.590
Granular damper	0.291	0.080	0.829	0.500	0.000	0.600	0.366
Granular damper with Spikes	0.267	0.240	0.752	0.500	0.200	0.600	0.415
Granular damper with Magnetism	0.173	0.080	0.205	0.500	1.000	0.600	0.318
Structural frame	1.000	0.000	1.000	0.000	0.000	1.000	0.464
Structural frame with Spikes	0.976	0.120	0.923	0.000	0.200	1.000	0.501
Structural frame with Magnetism	0.882	0.000	0.299	0.000	1.000	0.600	0.345

The results are conclusive, with a clear winning concept in the pallet with cold gas thruster combination. This concept is the best performer in the highest-weighted criterion, operational range, due to its effective impact dampening system and its surface agnostic attachment system. Furthermore, it is also the best performer in terms of adaptability, due to the thruster firing time being able to be modified after launch, and positional assurance, as the thrust should lock it into both position and orientation. It also performs well in the TRL scale, as both pallet and thrusters have been flight qualified for the Schiaparreli and Philae landers respectively. The concept receives a lower score with regards to mass; this is only natural, as it is being compared to systems like the structural frame, which are extremely lightweight but sacrifice operational range. Lastly, due to the relatively complexity of the system, it does not score well in the operational reliability; however, this is relative to fully passive systems like the structural frame. Overall this should not be a concern, as it cleared the initial killer requirement for this criterion.

Despite there being a clear and logical winner, it is always good practice to conduct a sensitivity analysis on the criteria weights. These were varied from the original ones obtained through the AHP using a *Python* script. The script exhausts all possible combinations of criteria weights as they vary between 50% and 150% from their original values in steps of 10%. For each possible combination, it then re-calculates the winning concept which is then tallied. The results of the full sensitivity analysis are showcased in Table 5.10.

Table 5.10: Results of sensitivity study of the winning concept with varying criteria weights.

Concept	Number of winning simulations	Percentage of winning simulations
Pallet	163,658	9.238
Pallet with Ice screws	60	0.003
Pallet with Harpoon	17,030	0.961
Pallet with Cold gas thruster	1,573,582	88.82
Structural frame	17,231	0.972

The results from the sensitivity analysis are conclusive, with only five different concepts winning across all iterations. The pallet with cold gas thruster is the winning concept in 88.82% of the iterations. This leads credence to the trade-off procedure, assuring that the concept selection is free from biases in the criteria weights.

6

Numerical astrodynamics simulation

In order to evaluate the key enabling subsystems in Chapter 5, data from the JPL Small-Body Database Browser was used together with the relevant equations to provide estimates on landing speed. This approximation, while suitable for a conceptual trade-off, is too simplistic as it assumes a simple two-body problem without any perturbing accelerations as discussed in Chapter 4. Therefore, in an effort to improve the accuracy of the data, simulations must be performed. The package chosen to implement these simulations is *Tudatpy*.

The TU Delft Astrodynamics Toolbox (*Tudat*) is a toolbox comprised of different sets of programmatic libraries, which allows researchers to implement a variety of astrodynamics simulations with relative ease. *Tudat* provides out-of-the-box, the core building blocks of any numerical astrodynamics simulation such as state propagation and estimation functionality, standard integrator types, and acceleration models. This allows for the relatively quick set-up of simulations, ranging from multi-gravity assist manoeuvres to in-orbit space debris simulations. *Tudat*'s functionality is implemented in C++, however, in order to further facilitate its implementation, *Tudat* is also provided using a *Python* wrapper as *Tudatpy* [72]. Therefore, due to the database scrapper and concept evaluation scripts being coded also in *Python Tudatpy* was selected over *Tudat* for the implementation of the simulations. This allows for quick iteration between models due to the common language they are implemented in (*Python*), as is the intention behind the implementation of MBSE.

To the best of the author's knowledge, at the time of the writing of this paper, development of simulations involving SSSBs with *Tudat* has been limited, with the majority of the use cases being planetary or natural satellite exploration, gravity assists, Earth observation and communication, and space debris. For this reason *Tudat* incorporates a number of functionalities which are not relevant to the simulation of SSSBs, such as aerodynamic models. Furthermore, the gravitational models implemented in *Tudat* are restricted to point masses and spherical harmonics; as discussed in Chapter 3 although computationally efficient, this is not optimal for SSSBs due to the lack of built-in collision detection. Despite these issues, *Tudatpy* remains a good option for the implementation of the simulation, due to the expertise in its use at the TU Delft, extensive documentation, and free licensing.

6.1. Simulation set-up

Before any simulation can be carried out in *Tudat*, it must be set-up according to the problem at hand. Depending on the computational complexity of the simulation, this is often the most time-consuming stage of carrying out the simulation as there are a multitude of options available for each setting and they must be selected carefully. As mentioned earlier in the chapter, *Tudat* has extensive documentation, complete with several examples. One of the most recent examples involves the optimization of a

satellite's orbit around the asteroid Itokawa. Therefore, this example is used as a template for the set-up of the simulation, including the target SSSB. Below, a selection of main parameters of the simulation set-up are detailed.

6.1.1. Body set-up

Tudat incorporates a number of standard celestial objects from SPICE together with a number of their orbital parameters and properties. SPICE is an information system developed by the Navigation and Ancillary Information Facility (NAIF) under NASA. It is used for a number of activities by the scientific community ranging from conceptual mission design to correlation of real instrument data [73]. For the simulation the bodies of the Sun, Earth, Mars, Jupiter, and Saturn are added from SPICE's data. The remaining bodies for the simulation, the target SSSB and the lander, are added instead as empty bodies with their characteristics being added individually, which allows for full control over the simulation.

The SSSB's Keplerian elements (eccentricity, inclination, semi-major axis, longitude of the ascending node, argument of periapsis, and true anomaly), heliocentric spherical coordinates, rotation rate, radius, and gravitational potential are provided, together with a reference Julian date for the measurement of the relevant elements.

For the lander, simply its mass, and radiation pressure coefficient and area are embedded. Before the simulation is initialized, with the SSSB as the origin for the reference frame of the simulation, its Cartesian coordinates and velocities relative to the SSSB are also defined. As the lander is meant to be deployed from a mothership after characterization of the SSSB's surface, a stable circular orbit around the SSSB is used for the initial coordinates and velocities of the lander. In order to simulate the inherent level of uncertainty of the deployment, conservative uncertainty values of 5% are implemented in the position and velocity vectors. Furthermore, a deployment velocity of 0.2 m/s is added, pointed towards the origin of the reference frame.

6.1.2. Acceleration model set-up

One of the advantages of using a thruster as the rebound suppression subsystem, is the possibility of additionally using the thruster for active descent control, which would improve the accuracy of the landing site as well as increase the maximum deployment altitude from the target. *Tudat* has thrust models integrated within its standard acceleration models, where the mass of the spacecraft is set as a variable, which decreases based on the selected thrust and specific impulse levels of the thruster. Implementation of this feature was attempted, but was unsuccessful, due to *Tudat* being limited to either a constant or a time-dependent thrust vector setting. *Tudat* is highly customizable, thereby allowing for the implementation of an algorithm which simulates the lander orientation. However, due to its complexity, it was deemed outside of the scope of the thesis. Instead, an uncontrolled approach and landing was simulated.

The remaining accelerations exerted on the lander, as detailed in Section 4.2.1, originate from gravitational sources and Solar radiation pressure. The gravitational potential of the SSSB is derived using spherical harmonics expanded up to order 4 and degree 4, and using point masses for the main Solar system bodies. For the purposes of simulating radiation pressure, the lander is modelled using the cannonball model, where the shape of the lander is assumed to be spherical [74].

6.1.3. Integrator set-up

In order to solve the dynamics equations responsible for propagating the simulation from the initial conditions until the termination criteria are met, *Tudat* incorporates a number of integrator types. These integrators are based on different algorithms, where the deciding factor between different integrator types is usually a trade-off between stability and computational cost; additionally, the methods will make use of either a fixed or variable step size. The integrator selected for the simulations is a Runge-

Kutta-Fehlberg method of orders 7 and 8. Multiple order (or embedded) methods are used to achieve a variable step size without having to solve the problem twice, which naturally doubles the computational expense. Instead, embedded methods estimate the solution at each time step and compare the solutions. The comparison is then evaluated against a predetermined threshold, whereby if the difference is too large the step size is decreased, or vice versa, which results in a relatively computationally cheap and robust integrator [75].

6.2. Single SSSB simulation and deployment altitude iteration

Initially, the simulation is set-up for a single SSSB, specifically, asteroid Itokawa. The termination settings for the simulation are set for the lander reaching Itokawa's surface, or exceeding the set maximum simulation time of twelve days. During the simulation, the altitude, and positional and velocity vectors in the Cartesian frame are saved as dependent variables. These can be plotted once the simulation is completed using the pyplot library. Initial simulations at different altitudes were successful in reaching the surface of the SSSB. One such example at a deployment altitude of 8 km can be seen in Figure 6.1.

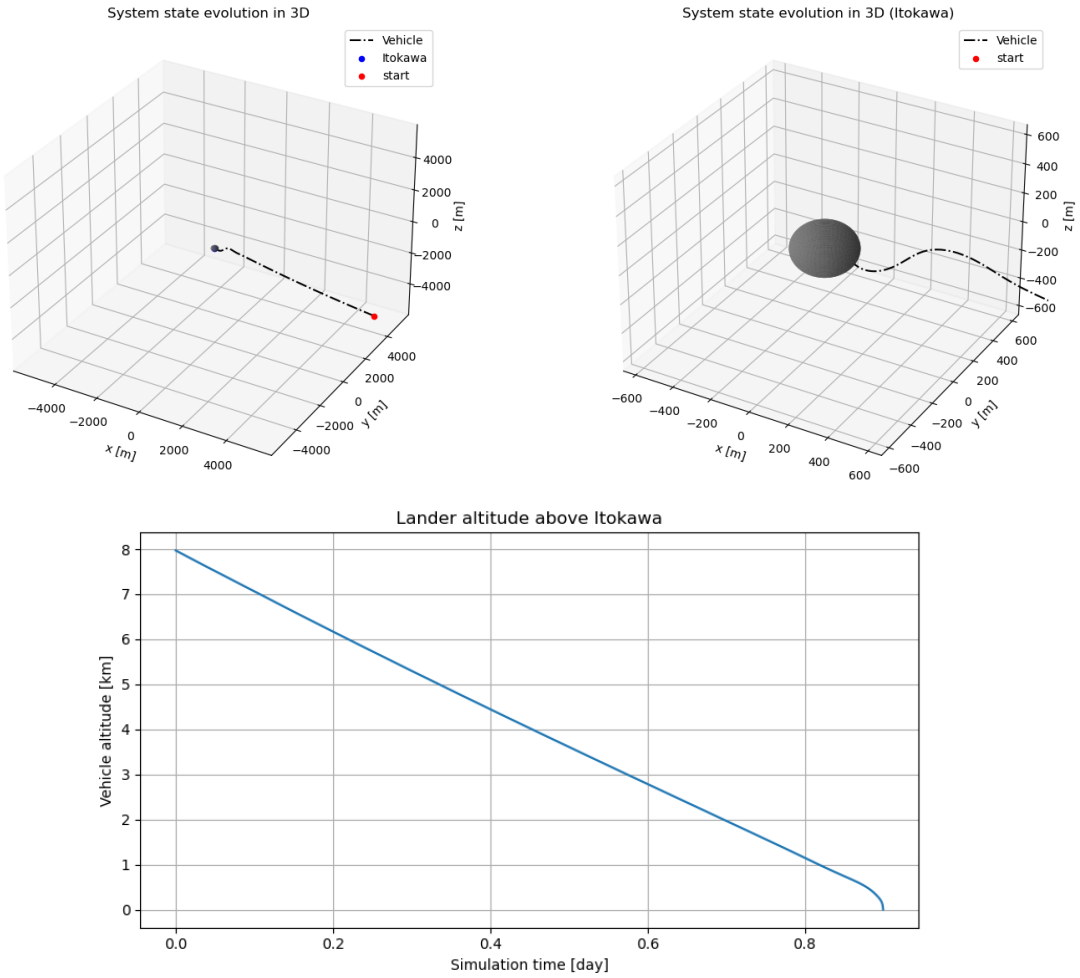

Figure 6.1: Lander trajectory plots (zoomed-in on the right) and altitude graph (below) of successful landing from 8 km altitude deployment.

However, due to the perturbing accelerations, and the uncertainties introduced in the position and velocity vectors described previously, once a certain deployment altitude is reached, the lander will miss the target. An example of this is depicted in Figure 6.2, with a deployment altitude of 9 km.

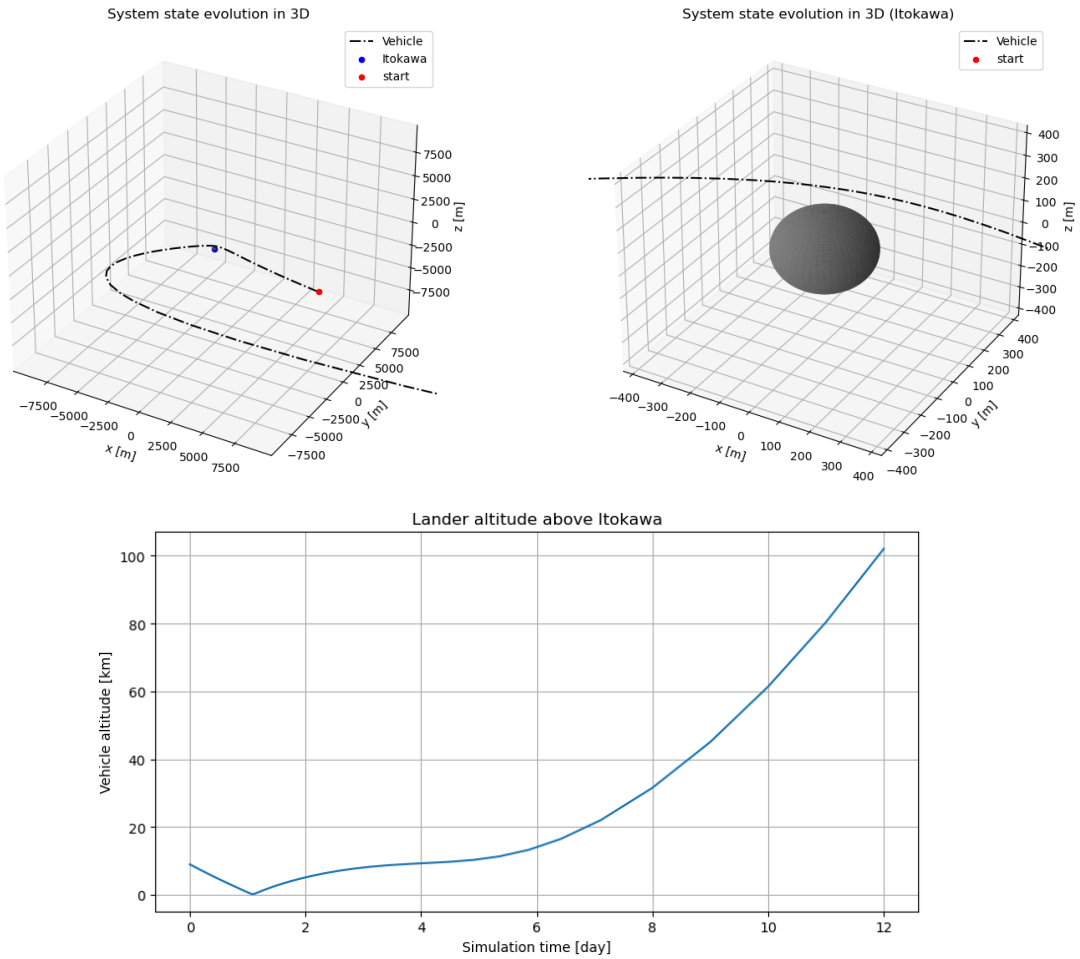

Figure 6.2: Lander trajectory plots (zoomed-in on the right) (above) and altitude graph (below) of failed landing from 9 km altitude deployment.

This means that through deployment altitude iteration, the maximum deployment altitude for an uncontrolled landing can be determined. This was implemented in the simulation via a simple for-loop, with intermediate results being stored. Once this maximum deployment altitude has been reached, the previous simulation's data where the lander reached the surface can be stored. In particular the impact velocity is of most significance, as it will allow for the sizing of the key enabling subsystems.

After iterating the simulation over multiple altitudes, it was observed that in limit cases, where the gravitational attraction due to the SSSB is roughly equal to the disturbing forces, there were noticeable differences in results across different runs with the same settings. This can be seen in Figure 6.3, where from a deployment altitude of 8.015 km and using the same settings, the trajectory of the lander is considerably altered between runs. Initially it was predicted that this effect could be caused due to the variable integrator step size present in the Runge-Kutta-Fehlberg method. However, when using a Runge-Kutta 4th order method with fixed step size, the inconsistencies persisted.

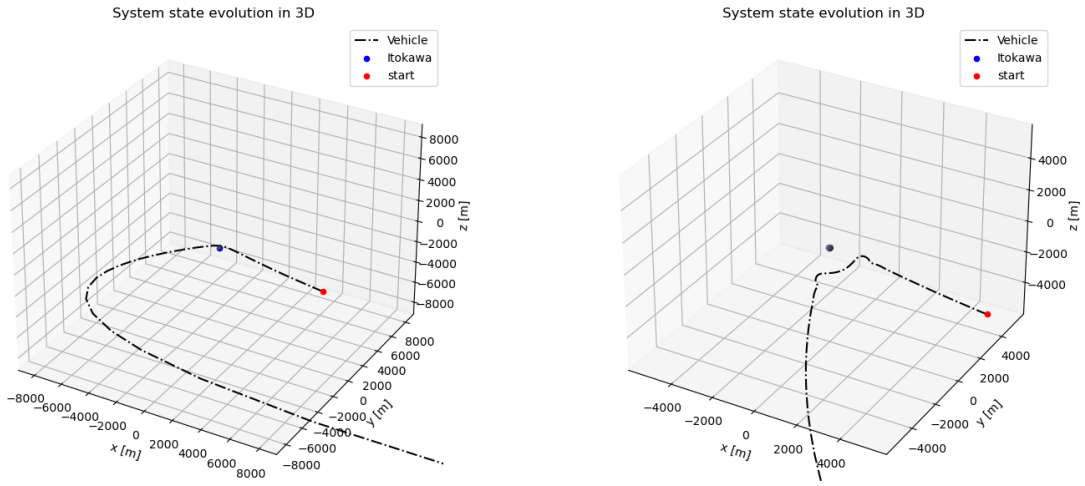

Figure 6.3: Differing lander trajectories from 8.015 km altitude deployment with identical set-up.

6.3. Iteration over SSSB database

Once the simulation script ran reliably and generated the required results for a single SSSB, it was merged with the SSSB database described in Section 5.1, following the principles of the MBSE methodology. The *pandas* library is used for the sorting, filtering, modification, and addition of data into the database. Furthermore, it has embedded file compression capabilities, useful for storing intermediate results with relatively low memory expense. This is useful in case the overall script encounters an error at some point and crashes, as the intermediate results are saved. Furthermore, it can be used in long simulations to fragment runtimes into more manageable sections, based on the user's preference.

The database was serialized for compression, and imported into the simulation script. The script then iterates over each entry in the database, corresponding to a specific SSSB. The SSSB's Keplerian elements (eccentricity, inclination, semi-major axis, longitude of the ascending node, argument of periapsis, and true anomaly), heliocentric spherical coordinates, rotation rate, radius, and gravitational potential, are imported from the database and used as inputs for the simulation script. The simulation is then carried out for increasing deployment altitude for each SSSB as described previously, resulting in a maximum deployment height and its corresponding impact velocity. These parameters are then added to the entries of the database, which is then serialized again for future use. In order to reduce the total simulation time, the termination settings were modified, with an additional termination condition being added for maximum distance from the SSSB, equal to double of the deployment distance. Once

the full database was iterated through, the same issues regarding inconsistencies in the simulation were found, as described inSection 6.2. In order to address this, the simulations were repeated tenfold. This provided for a large enough sample that outliers could be identified and removed. The results of the simulations can be seen in Figure 6.4, where the relevant distributions of deployment altitudes and velocities can be seen.

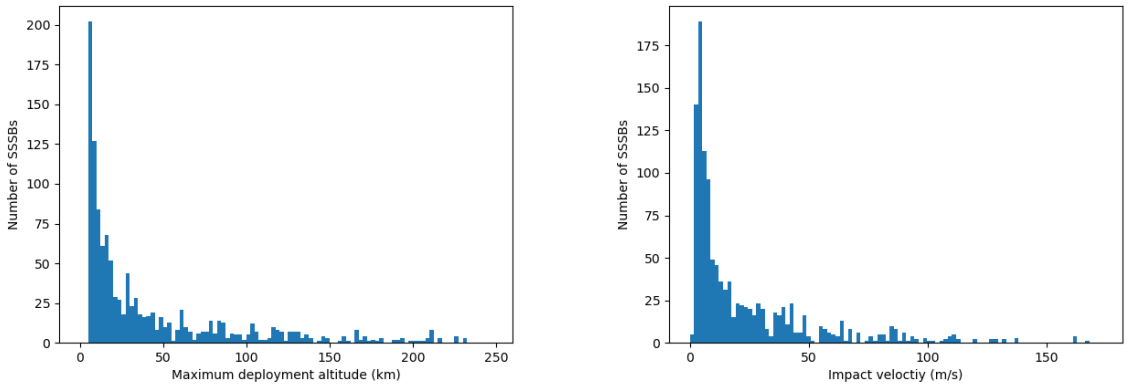

Figure 6.4: Histograms of the main simulation outputs: deployment altitude (left) and impact velocity (right).

As expected, these distributions closely resemble those of the gravitational parameter and diameter. Furthermore, as evident from Figure 6.5, these variables also have a direct correlation to each other, with SSSBs with larger gravitational pull resulting in increased maximum deployment altitude and correspondingly impact velocity. Lastly, in Figure 6.5 a comparison is made between the main simulation outputs and the relevant SSSB diameter, again highlighting the correlation between these parameters and the diameter as expected.

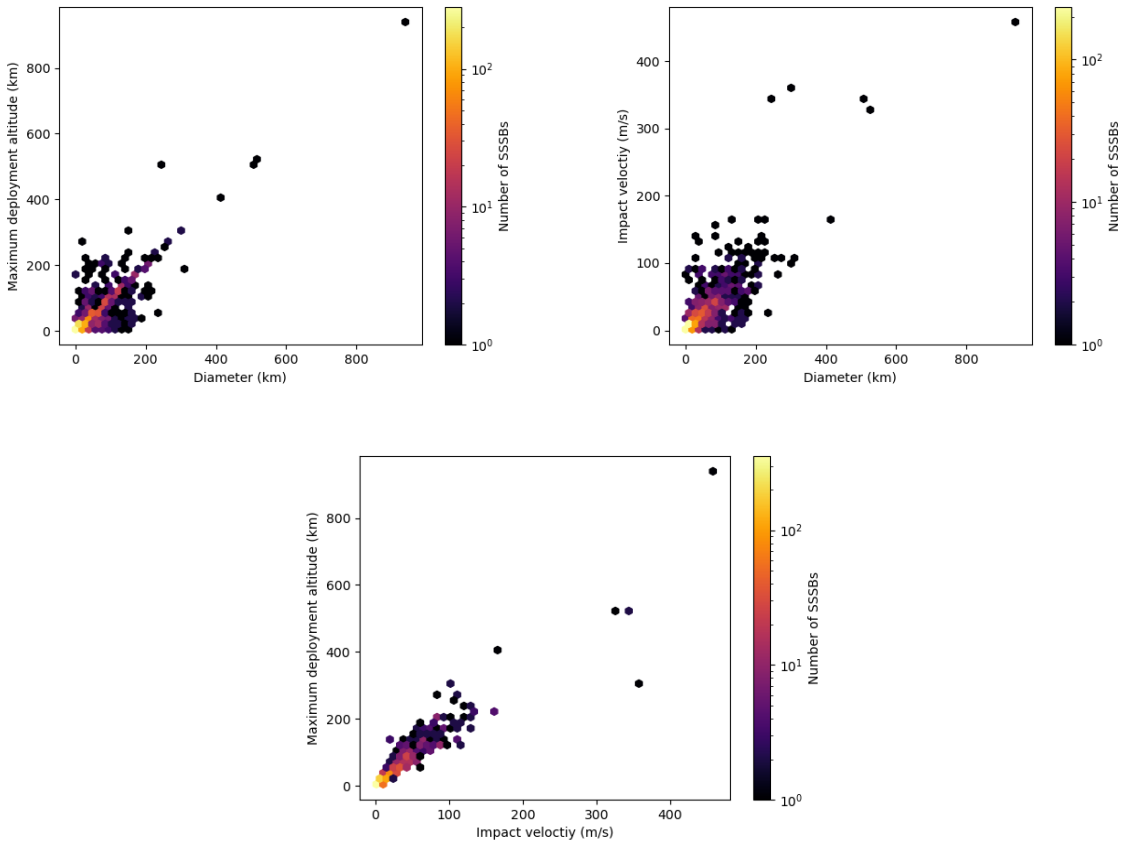

Figure 6.5: Hexbin plots of maximum deployable altitude (top left), and impact velocity (top right) vs SSSB diameter, and maximum deployable altitude vs impact velocity.

7

Detailed design

In this chapter the detailed design of the lander is presented, with a focus on its key enabling subsystems. Then the remaining subsystems are detailed, with a distinction between environment- and payload-driven subsystems.

7.1. Impact dampening subsystem

Crushable structures are implemented in most dampening systems due to their excellent dampening performance and low mass. Sandwich panels are layered structures which combine face-sheets with a core. This combination allows for very high structural rigidity at a low mass. Additionally, sandwich structures perform very well relative to their mass as impact dampeners when a metallic core is used. This is due to the plastic deformation that each cell of the honeycomb core undergoes, which transforms the impact force into the buckling and deformation of the hexagonal cell walls. The honeycomb structure is typically manufactured using aluminium where the commercially available alloys are 5052 and 5056 [76].

The mass efficiency for maximizing the touchdown δv that the honeycomb will reduce can be simply calculated, as derived by Grimm et al.:

$$E_k = E_{\text{plast}}. \tag{7.1}$$

where E_{plast} is the energy required for the honeycomb to undergo plastic deformation. With the following definitions:

$$E_k = \frac{1}{2} m_{\text{total}} \cdot v^2, \tag{7.2}$$

$$E_{\text{plast}} = F_{\text{crush}} \cdot s, \tag{7.3}$$

and

$$F_{\text{crush}} = \sigma \cdot A. \tag{7.4}$$

Here, s represents the length of the crushed honeycomb column, A its cross-sectional area and σ the crush strength. Combining Equations 7.1, 7.2, 7.3, and 7.4 leads to:

$$\frac{1}{2} m_{\text{total}} \cdot v^2 = \sigma \cdot A \cdot s. \tag{7.5}$$

Here, the product of area and length can be defined as the crush volume V_{crush}, equivalent to the mass of the honeycomb m_{crush} divided by its bulk density ρ:

$$v_{\text{crush}} \equiv A \cdot s = \frac{m_{\text{crush}}}{\rho}. \tag{7.6}$$

Grimm et al. used the data provided by Hexcel, the leading manufacturer for honeycomb structures for aerospace applications [76], to derive an approximate relation for the crush strength as a function of the bulk density of the honeycomb: $\sigma \approx k \cdot \rho^2$. From that, it then follows that:

$$v_{\text{crush}} = \sqrt{\frac{k}{\sigma}} \cdot m_{\text{crush}}. \tag{7.7}$$

Grimm et al. derived relations for aluminium alloys 5052 and 5056 of $\sigma = 0.962\rho^{1.766}$ and $\sigma = 1.399\rho^{1.666}$ respectively [76]. This shows that the derived relation is an approximation at best. Additionally, Hexcel manufactures honeycombs using different coatings, materials and cell sizes for which this approximation may not hold. Therefore, this relation and its application would require further investigation.

Combining Equations 7.5 and 7.7 leads to:

$$\frac{1}{2} m_{\text{total}} \cdot v^2 = \sigma \cdot \sqrt{\frac{k}{\sigma}} \cdot m_{\text{crush}}. \tag{7.8}$$

Rearranging leads to a mass ratio of:

$$\frac{m_{\text{crush}}}{m_{\text{sys}}} = \frac{\Delta v^2}{2\sqrt{k\sigma} - \Delta v^2}. \tag{7.9}$$

This allows for effective comparison of systems employing customized crushable structures against other systems. This evaluation was made by Grimm et al., leading to Figure 7.1, where the velocity absorption performance of honeycomb structures of varying strength is compared to that of an adapted cold-gas thruster. It is important to note, that Hexcel's standard aluminium honeycomb can achieve a crushing strength of up to 20 MPa [76], resulting in a higher mass efficiency.

The mechanical properties of the honeycomb structure can be adapted for each application by modifying the material, cell size, wall thickness, column length, and perforation. Both cell size and wall thickness can be decreased and increased respectively to increase the packing factor of the honeycomb, thus increasing its density. Increased column length will result in an increase in the ability of the structure to absorb energy at a given crush strength.

Another important consideration following the use of honeycomb structures is its performance following either a distributed or concentrated impact. Schröder, Grimm and Witte conducted impact tests to evaluate this difference in performance for a shell concept encasing the full lander. They performed impact tests on honeycomb structures using both a flat surface and a penetrator, simulating a surface and boulder contacts respectively. Additionally they investigated the effect of adding a facesheet, made up of layers of high-modulus polyethylene Dyneema®. Schröder, Grimm and Witte concluded that facesheets can be used to improve the force distribution and add compressive strength to the honeycomb structure, thereby increasing its crush strength [58].

7.1.1. Honeycomb configuration

Honeycomb manufacturers offer honeycomb in different lengths, shapes, materials and configurations. Crushable structures absorb impact energy by undergoing plastic deformation of the honeycomb cells.

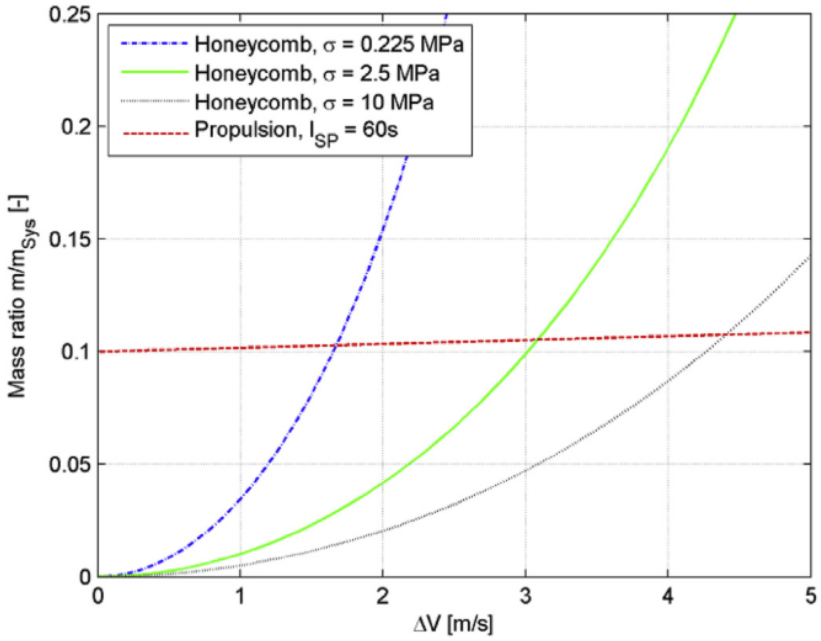

Figure 7.1: Mass ratios vs absorbed velocity of honeycomb structures with varying crush strength compared to a cold gas propulsion system (from Grimm et al. [59]).

Therefore, any suitable material for the panel should be able to plastically deform. There are three main material types which are used by the industry to manufacture structural honeycomb; these are aramid fibres, glass fibres, and aluminium [77]. Among these materials, aluminium is the only one which satisfied the aforementioned requirement of plastic deformation; therefore, it is the selected material for the honeycomb pallet. There are two main aluminium alloys manufactured for aerospace applications; alloys 5052 and 5056. The final alloy allocation will depend on the COTS availability from manufacturers, as well as its energy absorption to mass ratio.

Another aspect to the design of honeycomb is the shape of its cells. The main options available from manufacturers include Hexagonal, OX, Flex, Double-Flex, and Reinforced Hexagonal cores; these can be seen in Figure 7.2. Hexagonal cores are the most efficient in terms of compressive strength to mass ratio. OX-core honeycomb keeps an hexagonal shape, however, one of its dimensions is stretched in order to improve its shear strength properties in the direction of elongation. Both the Flex, and Double-Flex cores are designed for the same purpose, improving formability. Due to their cross-sectional shape, they can be easily bent into tight radii without buckling the honeycomb columns. Lastly, the Reinforced Hexagonal core adds a sheet of material splitting the hexagonal cells improving compressive strength. However, this reinforcement is less mass-efficient than modifying the cell size [78]. Since the honeycomb will not have to be curved, and its mechanical properties in shear are not relevant for its impact dampening capabilities, the traditional hexagonal cross-section is selected for this application.

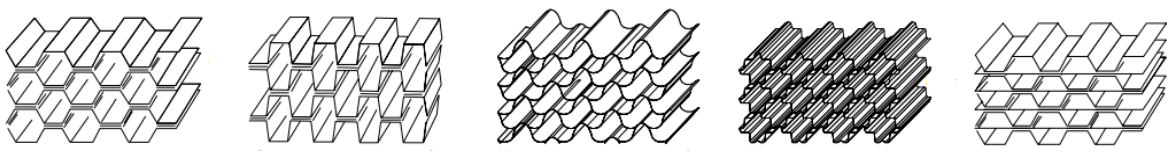

Figure 7.2: Different cell types (from left to right): Hexagonal, OX, Flex, Double-Flex, Reinforced Hexagonal (adapted from Hexcel [77]).

Pre-crushing is a technique used in the design of thin-walled aluminium honeycomb structures. Pre-crushing involves a short compressive stroke applied in the loading direction of the honeycomb, which causes slight buckling in the aluminium columns. When non-crushed honeycomb undergoes an impact,

it requires a large crush load to initiate the plastic deformation in the honeycomb columns, which then stabilizes into a uniform crush curve. However, if the honeycomb is pre-crushed, this peak is eliminated, with only the uniform crush curve remaining. These processes can be seen in the experimental results obtained by Zakrisson [79], displayed in Figure 7.3. The use of pre-crushing therefore allows for significantly lower impact shock accelerations exerted on the payload and subsystems, and thus is implemented in the design of the pallet.

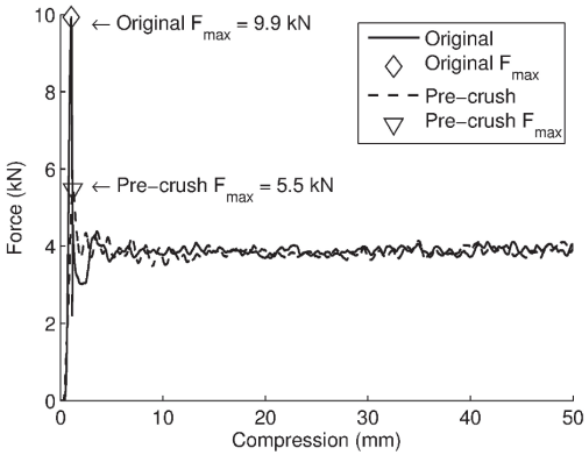

Figure 7.3: Force-displacement compression test of non-crushed and pre-crushed (from Zakrisson [79]).

Lastly, honeycomb structures are sometimes perforated along the column length. This can be done in order to improve its sound attenuation properties, allow for correct air flow in moulding, and improve the venting of adhesives. However none of these applications are relevant to its energy absorption qualities, and thus perforation is not incorporated in the design.

7.1.2. Shape and dimensions

The simplest shape that the pallet could have would be a simple extension of its base as depicted in Figure 7.4. However, following the theory described in Section 4.6, according to Schröder, Grimm, and Witte [58] during non-centered impacts, only a fraction of the total lander mass will act on impact. This effectively reduces the kinetic energy of the impact since $E_{\text{kin}} = \frac{1}{2}mv^2$ as $E_{\text{kin}} \propto m$. Equation 4.38 for the mass distribution after an off-center impact, derived in Section 4.6 can be used to optimize the pallet's shape, as shown in Figure 7.5. After volumetric calculations using *CATIAv5*, the optimization results in volume, and consequently mass, savings of 66%.

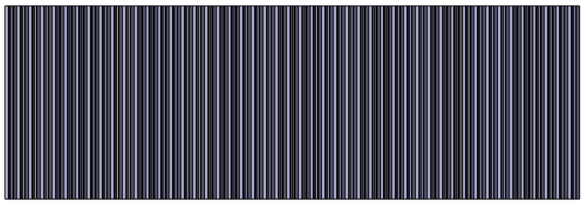

Figure 7.4: Render of the basic pallet.

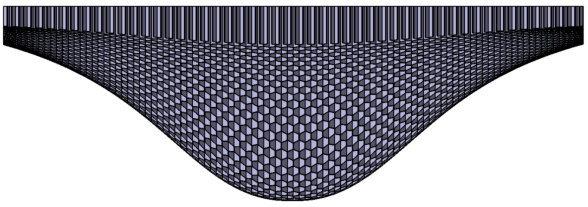

Figure 7.5: Render of the optimized pallet.

While the optimized shape is undoubtedly complex, aluminium honeycomb is relatively simple to machine, with complex surface morphologies being possible with the proper tooling [80]. A less complex alternative to the the gradual curve obtained from Equation 4.38, would be approximate this shape with circular .

Overall the pallet is attached to the base of the lander, thereby sharing those dimensions. For a lander dimension of 0.3x0.3x0.2 m (equivalent to MASCOT), a maximum column length of 0.1 m is set, thereby resulting in a maximum total lander volume of 9U.

7.1.3. Adaptability

The main focus of the thesis is to output a design which is highly adaptable, such that it may serve the maximum number of SSSBs with minimal modifications. There are three main parameters that can be adapted in order to modify the impact dampening capabilities of the honeycomb: the column length, cell size, material, and wall thickness. All factors have a direct effect on the mass of the pallet, with cell size, wall thickness, and material also affecting its crush strength. HexCel, the largest honeycomb manufacturer in Europe, provides for a selection of COTS aluminium honeycomb, with a minimum manufacturable column length of 0.25 inches. These COTS options vary in the alloy used (5052 and 5056), cell size (from 1/8th to 3/8ths of an inch), and wall thickness.

The initial step involves the analysis of which material performs better with regards to crush strength to mass ratio. In order to do this, the raw data from Hexcel was imported into Microsoft Excel. Hexcel provides for each alloy/cell size/wall thickness combination a number of parameters. These include density, crush strength, bare strength, and stabilized strength [76]. From these values, the most relevant for the lander design are density and crush strength. Therefore, a parameter which calculates the strength to density ratio was added for each combination, and used to assess the performance of the different alloys. The findings are presented in Table 7.1. Furthermore, as it is clear that alloy 5056 performed better in this regard, an additional parameter is added to express the increase in strength of going from alloy 5052 to 5056 as a percentage of the original strength.

Table 7.1: Comparison of strength/density for alloys 5052 and 5056 (raw data from Hexcel [76]).

		Strength/density [Pa kg/m^3]		
Cell Size [in]	Nominal Density [kg/m3]	Alu5052	Alu5056	% difference
0.375	1	1.81E+04	2.36E+04	31%
0.25	1.6	2.49E+04	3.06E+04	23%
0.375	1.6	3.18E+04	3.78E+04	19%
0.1875	2	3.99E+04	4.30E+04	8%
0.25	2.3	1.49E+04	1.99E+04	33%
0.375	2.3	2.10E+04	2.66E+04	27%
0.15625	2.6	2.76E+04	3.41E+04	24%
0.375	3	3.59E+04	4.05E+04	13%
0.125	3.1	1.29E+04	1.61E+04	25%
0.1875	3.1	1.81E+04	2.36E+04	31%
0.25	3.4	2.45E+04	3.03E+04	24%
0.15625	3.8	2.95E+04	3.62E+04	23%
0.25	4.3	1.08E+04	1.35E+04	25%
0.1875	4.4	1.40E+04	1.87E+04	33%
0.125	4.5	1.90E+04	2.53E+04	33%
0.25	5.2	2.30E+04	3.00E+04	30%
0.15625	5.3	2.77E+04	3.39E+04	22%
0.1875	5.7	1.08E+04	1.51E+04	40%
0.125	6.1	1.08E+04	1.35E+04	25%
0.15625	6.9	1.40E+04	1.87E+04	33%
0.125	8.1	1.72E+04	2.30E+04	33%

The data is conclusive: alloy 5056 performs better than alloy 5052 at similar density/cell size. This difference is more pronounced with increased nominal density, however this is clearly not a linear relationship. It is important to note that although alloy 5056 is stronger, Hexcel offers higher density, and thereby higher strength, honeycombs only using 5052, with increased cell wall thickness. Therefore these options will be also added to the pool of selectable honeycombs.

In order to select a suitable honeycomb for each individual SSSB landing, the available honeycomb configurations were sorted by density, in order to see how it related to crush strength, as shown in Figure 7.6. Here, cells are coloured using conditional formatting, where the colour of each cell follows

a gradient based on the maximum and minimum values in the column. In Figure 7.6 a red-yellow-green colour gradient is used, where green is used for low density and high strength. This method allows for easy graphical evaluation of the data.

Cell Size	Nominal Density	Compressive strength					Crush Strength
		Bare strength		Stabilized strength			
		typ	min	typ	min	modulus	
9.54	16.0185	3.79E+05	1.72E+05	4.14E+05	2.41E+05	1.03E+08	2.41E+05
6.36	25.6296	6.89E+05	5.17E+05	7.58E+05	5.52E+05	2.07E+08	3.45E+05
9.54	25.6296	6.89E+05	5.17E+05	7.58E+05	5.52E+05	2.07E+08	3.45E+05
4.77	32.037	1.31E+06	7.58E+05	1.38E+06	8.27E+05	3.10E+08	5.17E+05
9.54	36.84255	1.48E+06	1.07E+06	1.55E+06	1.07E+06	4.00E+08	6.89E+05
6.36	36.84255	1.65E+06	1.00E+06	1.83E+06	1.07E+06	4.00E+08	6.89E+05
3.975	41.6481	1.72E+06	1.24E+06	1.83E+06	1.28E+06	4.83E+08	8.27E+05
3.18	49.65735	2.21E+06	1.72E+06	2.41E+06	1.79E+06	6.69E+08	1.17E+06
9.54	48.0555	2.21E+06	1.65E+06	2.34E+06	1.79E+06	6.34E+08	1.10E+06
4.77	49.65735	2.62E+06	1.72E+06	2.83E+06	1.79E+06	6.69E+08	1.17E+06
6.36	54.4629	2.76E+06	2.07E+06	3.31E+06	2.17E+06	7.93E+08	1.38E+06
3.975	60.8703	3.10E+06	2.48E+06	3.45E+06	2.59E+06	9.65E+08	1.62E+06
6.36	68.87955	4.00E+06	3.03E+06	4.27E+06	3.21E+06	1.19E+09	2.07E+06
4.77	70.4814	4.27E+06	3.17E+06	4.62E+06	3.38E+06	1.24E+09	2.14E+06
3.18	72.08325	4.90E+06	3.28E+06	4.76E+06	3.45E+06	1.28E+09	2.21E+06
6.36	83.2962	5.45E+06	4.14E+06	5.65E+06	4.45E+06	1.59E+09	2.83E+06
3.975	84.89805	5.65E+06	4.24E+06	5.96E+06	4.48E+06	1.65E+09	2.90E+06
4.77	91.30545	6.34E+06	4.72E+06	6.89E+06	5.07E+06	1.86E+09	3.31E+06
3.18	97.71285	7.72E+06	5.38E+06	8.27E+06	5.69E+06	2.03E+09	3.69E+06
3.975	110.52765	8.41E+06	6.34E+06	9.24E+06	6.89E+06	2.41E+09	4.48E+06
3.18	129.74985	1.21E+07	8.27E+06	1.31E+07	8.96E+06	3.00E+09	5.58E+06
(mm)	(kg/m^3)	(Pa)					

Figure 7.6: Density-sorted list of alloy 5056 honeycomb properties (raw data from Hexcel [76]).

The result, as expected, is that crush strength increases with density, meaning that different combinations of cell size and wall thickness will lead to a tiered list of increasing strength at the cost of increased pallet mass. This relation was further explored as shown in Figure 7.7, where each honeycomb configuration's density and crush strength for alloy 5056 were plotted. A trend line using a power law was found to be the best fit for the data, with an R^2 value of 0.9983. The relation is approximated by $\sigma = 1847.4\rho^{1.6518}$. This formula could allow for the generation of theoretical, higher-density concepts; however, with smaller cell size and increasing cell wall thickness, manufacturability may be an issue.

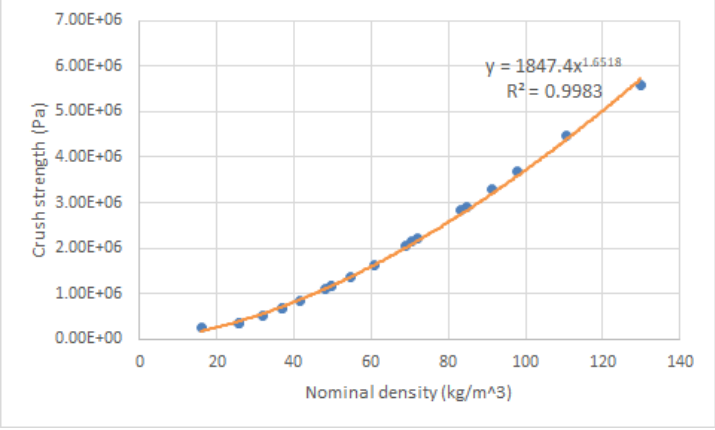

Figure 7.7: Crush strength as a function of density for alloy 5056 honeycomb.

7.1.4. Pallet sizing and allocation

In order to size the lander for each SSSB, a pallet design script was implemented in *Python*. It uses as main inputs the data obtained from the simulation as described in Chapter 6, as well as the data for all alloy 5056 honeycomb configurations as well as the densest amongst alloy 5052, as detailed previously. This data is imported into the script through serialized *Python* files, via the *pandas* library.

The script loops through each SSSB. An appropriate crush strength can be calculated for each landing by rearranging Equation 7.5, which leads to:

$$\sigma = \frac{m_{\text{total}} \cdot v^2}{2A \cdot s}. \tag{7.10}$$

Following the relationship plotted in Figure 7.7, it is obvious that the stronger honeycombs are more mass-efficient than their weaker counterparts. Therefore, a matching algorithm is used to round-up the crush strength of each SSSB impact to the closest available honeycomb crush strength. It is important to match the crush strength rather than total absorbed energy where possible. This is due to the fact that while decreasing column length with a smaller cell size may result in an equivalent total absorbed energy, it will also induce a much larger deceleration of the payload, due to the shorter crush stroke.

In the case that a specific impact exceeds the strength of the strongest available honeycomb, the necessary added column length for full impact energy absorption is calculated. As the impact's crush strength is always rounded up for the cell size/wall thickness allocation, the suitable honeycomb column length is likely overestimated for all SSSBs. Therefore, the crush length is recalculated after the honeycomb allocation for every impact, in order to have an accurate mass assessment. The minimum manufacturable column length by Hexcel is 6.35 mm [76], which is then naturally set as the minimum.

As the script iterates over the full SSSB database, all relevant parameters calculated are added as extra columns to the SSSB database. These are, honeycomb allocated, pallet volume, pallet mass, and column length. Once the script has iterated over the full database, the results are then serialized and stored using the *pandas* library. The results from the pallet allocation script are presented in Table 7.2.

Table 7.2: Results of pallet allocation.

Alloy	Density [kg/m^3]	Cell size [mm]	Number of SSSBs
5056	16.0185	0.00954	778
5056	32.037	0.00477	54
5056	36.84255	0.00636	51
5052	192.222	0.00318	43
5056	25.6296	0.00636	37
5056	54.4629	0.00636	34
5056	60.8703	0.00398	32
5056	68.87955	0.00636	29
5056	48.0555	0.00954	25
5056	41.6481	0.00398	25
5056	83.2962	0.00636	22
5052	160.185	0.00318	20
5056	129.74985	0.00318	16
5056	110.52765	0.00398	14
5056	97.71285	0.00318	14
5056	49.65735	0.00318	11
5056	91.30545	0.00477	10
5056	70.4814	0.00477	2
5056	84.89805	0.00398	2
Too large impact, requiring column length > 0.1 m			10

The results are conclusive, with the large majority of SSSBs using the weakest available honeycomb configuration. This is to be expected, as the honeycomb is quite effective at dampening impacts, and as shown in Figure 6.4, there is a large number of very low impact velocities. In fact, in 301 of the allocations, the column length reached its minimum value of 6.35 mm. These impacts may be considered weak enough that in fact, no dedicated impact dampening system is required, with the structure providing enough dampening. The distributions of both the pallet mass and the column length of the remaining allocations can be seen in Figure 7.8. The plots filter out those impacts that proved to be too large for the nominal column length of 100 mm (10 instances).

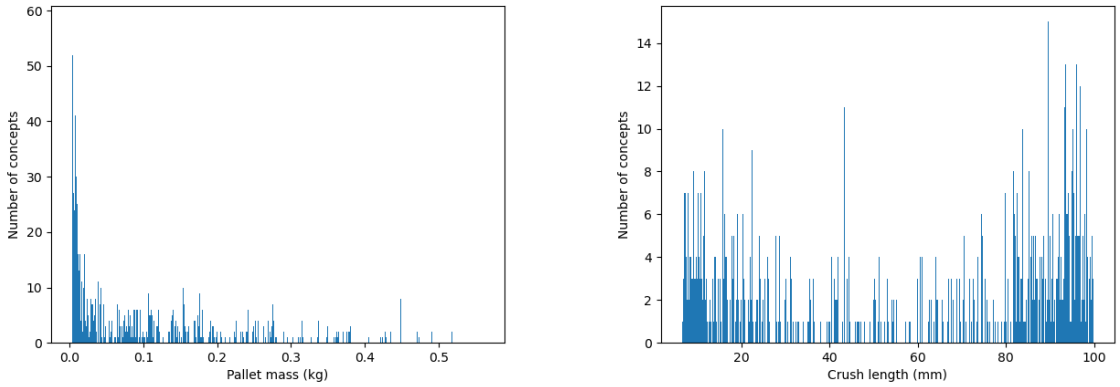

Figure 7.8: Distributions of the pallet mass (left) and crush length (right) allocations without outliers where (6.35 < crush length < 100 mm).

From the plots the data can be easily interpreted, with the large majority of pallets weighing below 0.05 kg. In the range between 0.05 to 0.3 kg there is a relatively even distribution, which drops off, with only a number of pallets exceeding 0.5 kg. Most of the pallets are well sized, with the largest concentration of pallets around the nominal size of 100 mm. There is an additional concentration between with column lengths between 0 and 10 mm; with the large majority of these impacts being very weak. Further study could determine whether these too do not require a dedicated impact dampening system. Overall, the largest pallet mass recorded (taking into account the extra length required for too large impacts) is 4.14 kg; the corresponding column length is 1077 mm.

7.2. Rebound suppression subsystem

In Section 5.3, the concepts evaluated operated mostly by physically attaching the lander to the SSSB surface. However, the winning concept uses a different approach. By eliminating the rebound altogether by the firing of a thruster opposite to the rebound motion, the lander should remain in place and in an upright orientation relative to the landing location.

7.2.1. Propulsion type

There are many types of propulsion technologies used in thrusters. There are many deciding factors when selecting the relevant working principle of a thruster, such as thrust levels and specific impulse. However, the are two main considerations when selecting the thruster for the lander's rebound suppression subsystem: safety and reliability.

In every mission to date equipped with an SSSB lander, the lander mission and deployment have been secondary payloads in the mission. This has two main consequences: the lander has less stringent redundancy requirements, and the lander design must follow a Do No Harm policy. Therefore the selected thruster type must use inert and non-toxic fuels [81].

As detailed in Chapter 5 one of the main criteria when evaluating the lander design is operational reliability. The thruster rebound suppression system is an active system, for this application its success relies on accurate timing, and an effective activation sequence, optimally equipped with redundancy. Due to the increase in mission risk introduced by a key enabling subsystem being active rather than passive, it is preferred if the subsystem is as inherently reliable as possible. The most effective ways to predict reliability in the conceptual design stage, are evaluating flight heritage and system complexity.

When accounting for safety and reliability as the main factors in the selection of a thruster type, the optimal choice is a cold gas thruster. Cold gas thrusters have extensive flight heritage, particularly in the form factor of the lander, as they are commonly used in CubeSats for orbit adjustment, and attitude control. Furthermore, in terms of complexity they are the simplest type of thrusters available and are considered a mature technology. Additionally, cold gas thrusters make use of inert gases as their fuel, ensuring that the Do No Harm policy for secondary payloads is met [82].

The main disadvantage of cold gas thrusters is that due to their low specific impulse, they are not able to perform manoeuvres requiring large amounts of delta-v [82]. However, the generally low impact velocities obtained from the simulation carried out in Chapter 6, coupled with the energy absorbed by the pallet, should result in uniformly low delta-v values required by most SSSB landings.

7.2.2. Cold gas thruster selection

Cold gas thrusters are considered the simplest propulsion system with flight heritage. However, this does not mean they are not complex systems. Furthermore, they require complex feed systems and their operating fuel must be selected. Therefore, to remain within the scope of the thesis, the optimal solution is the selection of a COTS integrated cold gas thruster.

NASA, on a yearly-basis, publishes a report: State-of-the-Art of Small Spacecraft Technology [82]. This report aims to be a complete survey of the currently available and developing small-scale spacecraft technologies and subsystems. One of the main sections of this report involves propulsion systems, and specifically lists 13 currently available cold and warm gas thrusters in the market for small spacecraft. Furthermore, a parameter specific to propulsion subsystems used to evaluate progress toward mission infusion (PMI) is included. PMI sorts propulsion systems based on the following categories: Concept (C), In-Development (D), Engineering-to-Flight (E), and Flight-Demonstrated (F). The complete table can be seen pictured in Figure 7.9.

One of the main factors in the overall selection of the rebound suppression system is reliability. Therefore it is important to choose a thruster system with a high PMI; for this reason, all non- Flight-Demonstrated (F) thrusters were excluded from the selection process, with the exception of the VACCO Standard Micro Propulsion System (MiPS). The Standard MiPS is a partial re-design of two thrusters also in the table, the MarCO-A and -B MiPS and the NEA Scout; with the MarCO variant already having flight heritage, and the NEA Scout planned launch in August 2022. Due to these factors, it is considered that the Standard MiPS is a mature technology, on par with the remaining F-status thrusters.

Out of remaining thrusters, the Standard MiPS (pictured in Figure 7.10) is the only one which is manufactured based on a modular design, which can be scaled for specific applications, with volumes ranging from 0.36 to 1.44 U. This is a very significant advantage for an adaptable lander, as each mission may have a tailored thruster without varying the design. Furthermore, the Standard MiPS is a fully integrated system, with the fuel tank and feed systems already incorporated in the design. The Standard MiPS also has redundancies implemented in its design, which increases its reliability. Equipped with four separate thrusters, redundant pressure control valves, a watchdog timer, and redundant seals and fill valves it is a very robust design. Additionally, if its flight heritage is extended from the MarCO-A and -B MiPS, it is the only thruster in the list with deep-space flight heritage, built with 18 krad Total Dose Radiation Tolerance [83]. Lastly, the Standard MiPS is one of the few thrusters with a complete data sheet, which reduces the amount of assumptions in the sizing and allocation design phase, increasing the confidence in the final design. Due to the significant advantages of the VACCO Standard MiPS over the competing thrusters, in particular its modular design, it is selected as the cold gas thruster to

Table 4-5: Cold and Warm Gas Propulsion												
Manufacturer	**Product**	**Propellant**	**Thrust (Quantity)**	**Specific Impulse**	**Total Impulse**	**Mass**	**Envelope**	**Power**	**ACS**	**Status**	**Missions**	**References**
---	---	---	[mN]	[s]	[N-s]	[kg]	[cm³ or U]	[W]	Y/N	C,D,E,F	---	---
Integrated Propulsion Systems												
Aerospace Corp.	MEPSI	R236fa	20	N/A	N/A	0.188	4 in. x 4 in. x 5in.	N/A	Y	E	STS-113 and STS-116	(44)
GomSpace / NanoSpace	Nanoprop CGP3	Butane	0.01 – 1 (x4)	60-110	40	0.3‡ 0.35†	0.5U	<2	Y	D	-	(50) (108)
GomSpace / NanoSpace	Nanoprop 6U	Butane	1 – 10 (x4)	60-110	80	0.770‡ 0.900†	200 mm x 100 mm x 50 mm	<2	Y	F	GomX-4	(50) (51) (109)
Lightsey Space Research	BioSentinel Propulsion System	R236fa	40 - 70	40.7	79.8	1.08 kg ‡ 1.28 kg †	220 mm x 100 mm x 40 mm	<1 W idle <4 W operating	Y	E	BioSentinel	(52) (53)
Marotta	MicroThruster	Nitrogen	0.05 – 2.36 N	70	N/A	N/A	N/A	<1	N/A	F	numerous	(43)
Micro Space	POPSAT-HIP1	Argon	0.083 – 1.1 (x8)	43	N/A	N/A	N/A	N/A	N/A	F	POPSAT-HIP1	(49)
SSTL	Butane Propulsion System	Butane	0.5 N							D	-	(45) (46)
ThrustMe	I2T5	Iodine	0.2		75	0.9†	0.5U	10	N	F	Xiaoxiang 1-08, Robusta-3A (2021**)	(62) (63) (64) (65)
UTIAS/SFL	CNAPS	Sulfur Hexafluoride	12.5 – 40	30	81	N/A	N/A	N/A	N	F	CanX-4/CanX-5	(110) (111)
VACCO	NEA Scout	R236fa	N/A	N/A	500	2.54†	2U	9	Y	E	NEA Scout (2021**)	(60) (61)
VACCO	MiPS Standard Cold Gas	R236fa	25 (x4)	40	98 – 489	553 – 957‡	0.4 – 1.38U	12 W (max)	Y	D	-	(57) (105)
VACCO	MarCO-A and -B MiPS	R236fa	25 (x8)	40	755	3.5	2U	15	Y	F	MarCO-A & -B	(57) (58) (59) (106)
VACCO	C-POD	R134A	25 (x8)	40	186	1.3	0.8U	5	Y	E	CPOD	(57) (107)

Note that all data is documented as provided in the references. Unless otherwise published, do not assume the data has been independently verified.
† denotes a wet mass, ‡ denotes a dry mass, N/A = Not Available, ** anticipated launch date

Figure 7.9: Cold and warm gas thruster compilation (from NASA [82]).

be used for the rebound suppression system.

Figure 7.10: VACCO's Standard MiPS (adapted from VACCO [83]).

7.2.3. Firing sequence

The only cold gas thruster used to date for an SSSB lander was the one onboard Philae, which failed to fire, due to issues with its pressure control valves [50]. While, as mentioned previously, the VACCO Standard MiPS has several redundancies implemented in its design it does not mean that it is impervious to failure. In fact, failure could originate from the triggering of the thruster firing and not from the thruster itself. Therefore, it is important for the triggering mechanism to have redundancies.

Proper triggering requires the fulfilment of a trigger condition. This can be achieved in three main ways: internal measurements, timing prediction, and external measurements. Ideally, the triggering condition has redundancy implemented in its operation, where optimal redundancy implementation would rely on different working principles to detect the landing.

A suitable trigger, based on internal measurement, is accelerometer data. The lander impacting the surface of the SSSB at a significant speed should produce an unmistakable deceleration. Furthermore,

space-qualified accelerometers are commonplace, as well as useful for operations and scientific data.

On the other hand, timing is a poor triggering mechanism, as exact prediction of landing from the time of deployment is not possible, and therefore any such estimation would most likely lead to a mistimed thruster firing. However, timing can be an excellent filter for false negatives. Despite exact landing predictions being unfeasible, relatively accurate landing timing predictions should be possible due to the lack of disturbing accelerations in the near-SSSB environment. Therefore, a timer could be easily implemented to improve system reliability.

External measurements would rely on sensing the distance to the surface of the target SSSB; this is done via altimeter readings which in space can operate via radar or laser. However, to date, no COTS altimeters are available for CubeSats [84]. While COTS cameras are commonplace, approximating distance measurements from photographs requires complex algorithms and can be unreliable. An alternative, implemented in MASCOT's design in order to verify the lander's orientation is the use of optical sensors. These sensors are made up of an infrared LED and a photo-diode couple, which, when given the command to switch on, can detect the presence of a surface via the reflected light of the LED. However, the range at which the reflection from these LEDs would be captured by the photo-diode is not known, as the system is designed for on-surface use.

Due to the aforementioned reasons, the proposed triggering mechanism would make use of redundant accelerometers coupled with a timer to avoid false positives.

7.2.4. Adaptability

As mentioned previously, the VACCO Standard MiPS is inherently adaptable due to its modular design. There are four variants offered by VACCO, the main data for which are shown in Table 7.3. Additionally, all variants share a specific impulse of 40 s, a thrust force of 0.1 N, and fixed base dimensions of 100 x 100 mm. Furthermore, an additional calculation is made in order to measure the relative mass efficiency of the different variants, in the Delta V / Wet Mass column. The relevant delta-v is calculated using Tsiolkovsky's rocket equation:

$$\Delta v = I_{sp} \cdot g_0 \cdot \ln \frac{m_{\text{wet}}}{m_{\text{dry}}}, \tag{7.11}$$

where I_{sp} represents the specific impulse of the thruster, g_0 is the standard gravity, and the wet and dry masses (m_{wet} and m_{dry}) take into account a 10 kg lander system mass. On the other hand, the wet mass used for the division that results in the Delta V / Wet Mass value, is that of the propulsion system itself. The results from this evaluation are conclusive and expected, with the propulsion system being more mass efficient in its larger variants.

Table 7.3: Performance parameters of the VACCO Standard MiPS variants (raw data from VACCO [85]).

Product	System Height [mm]	Total Impulse [N s]	Wet Mass [kg]	Envelope [U]	Dry Mass [kg]	Delta V / Wet Mass [m/s/kg]
X19039000-01	36	82	0.848	0.36	0.639	9.00
X19039000-02	70	219	1.356	0.7	0.799	14.55
X19039000-03	100	336	1.813	1.0	0.956	16.30
X19039000-04	144	515	2.458	1.44	1.114	18.22

The thruster variant is not the only parameter that can be adapted per launch. With the base dimensions of the Standard MiPS at 100 x 100 mm, in a MASCOT sized platform, theoretically up to nine sets of MiPS units could fit on the lander's body, thereby allowing for effective rebound suppression for SSSB landings where the resultant delta-v is too large for even variant X19039000-04. Furthermore, despite the maximum fuel capacity for each variant being set, the thruster can always be filled with less fuel based on the target, thus resulting in an overall lighter design.

7.2.5. Thruster sizing and allocation

Much like in Section 7.1.4, following the MBSE approach, a script was implemented using *Python* for the allocation of thrusters for each SSSB landing. The script imports, via the *pandas* library, the serialized SSSB database after the relevant parameters calculated in Section 7.1.4 have been added. The script also uses as input the data presented in Table 7.3.

In order to size the thruster, an appropriate rebound velocity must be calculated. This is dependent on the energy absorbed by the honeycomb. Grimm et al. conducted a study where the crush performance of aluminium honeycomb was assessed [59]. A segment of their findings, showcased in Figure 7.11 showed that honeycomb structures for a pallet-style impact dampener absorbed a minimum of around 60% of the impact energy. It is important to note that these honeycomb structures were not tailored to the impact energy, unlike those allocated in the database in Section 7.1.4. Therefore this estimate is quite conservative in nature and therefore underestimates the actual energy absorption capabilities of the honeycomb. In fact, Grimm et al. concluded that the absorbed energy uniquely depended on the material combination used.

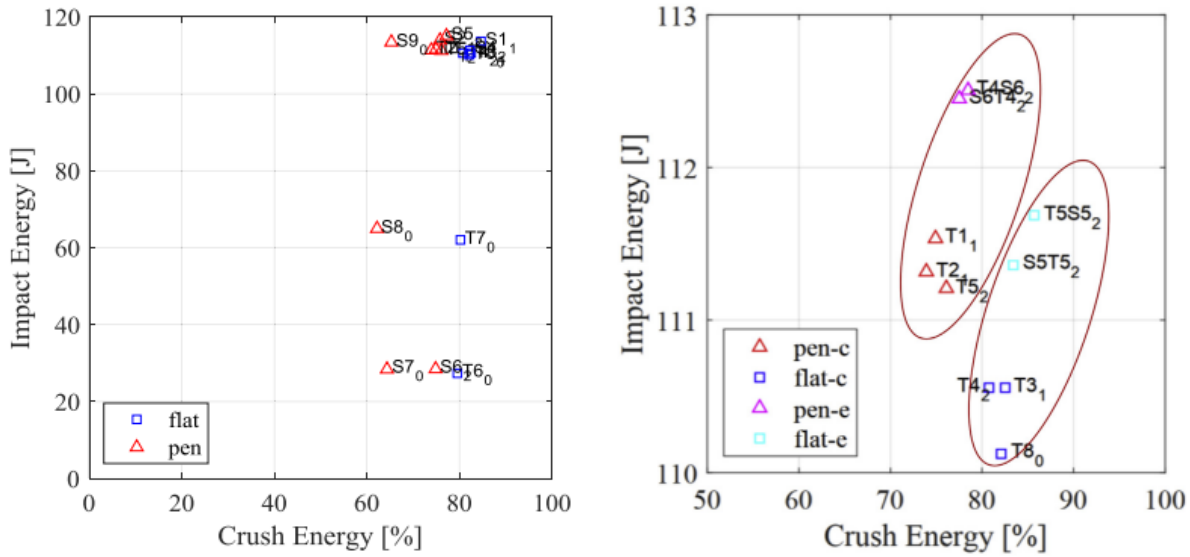

Figure 7.11: Energy absorption by different honeycomb assemblies (from Grim et al. [59]).

Nonetheless, the thruster allocation script assumes that only 65% of the impact energy is absorbed by the pallet. The remaining energy is then used to calculate the rebounding velocity; rearranging Equation 7.2 leads to:

$$v_{\text{reb}} = \sqrt{\frac{2 \cdot 0.35 \cdot E_{\text{imp}}}{m_{\text{total}}}}. \tag{7.12}$$

The script loops through each SSSB entry in the database, calculating the relevant rebounding velocity. This is the velocity that the rebound suppression system will have to equate to via a delta-v thruster firing. Since a predicted system mass is available, coupled with the pre-calculated pallet mass, Tsiolkovsky's rocket equation (Equation 7.11) can be rearranged to account for required fuel via:

$$m_{\text{fuel}} = m_{\text{wet}} - \frac{m_{\text{wet}}}{e^{v_{\text{reb}}/(I_{sp} \cdot g_0)}}. \tag{7.13}$$

As the fuel capacity of the Standard MiPS variants is known, the number of thrusters units required can be simply calculated as the rounding up to the nearest integer of the fraction of fuel required over the maximum fuel capacity (that of variant X19039000-04).

Once the number of thruster units is calculated, a sorting algorithm matches the required fuel with an appropriate thruster variant, which requires that the required fuel is round up to the closest thruster capacity. This leads to a dry thruster mass, which can be simply added to the fuel mass for a total system mass. Due to volume and mass constraints, the maximum number of thrusters onboard the lander is limited to two, effectively limiting the mass of the rebound suppression system to under 5 kg. Therefore, for large-velocity impacts, the delta-v exerted by the thruster may not be enough. For these situations, a resultant velocity is calculated by subtracting the delta-v from the rebounding velocity.

The key parameters calculated from this allocation procedure are then added to the database for each SSSB; namely the system wet mass, the number of thrusters, the specific thruster variant, and the resultant velocity (if any). The database is then once again serialized, and stored for any later analyses. This concludes the process of key enabling subsystem allocation. The results of the thruster allocation procedure are presented in Table 7.4 and Figure 7.12.

Table 7.4: Results of thruster allocation.

Number of thrusters	Thruster model	Number of SSSBs
1	X19039000-01	737
1	X19039000-02	278
1	X19039000-03	97
1	X19039000-04	80
2	X19039000-03	20
2	X19039000-04	7

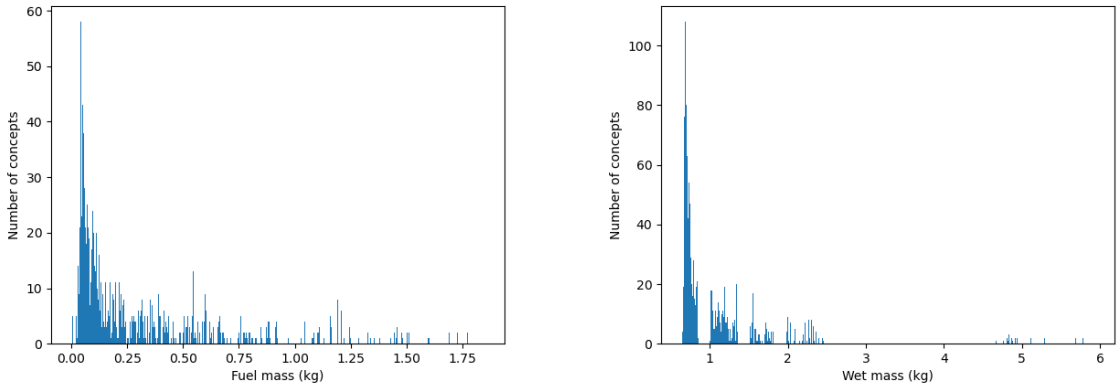

Figure 7.12: Distribution of the fuel mass (left) and wet mass (right) of the thruster allocations.

The results are conclusive, with clear separators in the wet masses due to the dry masses of the different models. The large majority of the SSSB missions require a single thruster, with only the more massive bodies requiring two. None of the SSSBs happened to exceed the maximum fuel capacity imposed by the maximum limit of two thrusters and the maximum capacity of thruster X19039000-04. For the large majority of SSSBs, the total thruster mass does not exceed 2.5 kg, with most being below 1.5 kg.

The immense majority of the thrusters allocated being the least powerful option. This implies that in fact, most of these thrusters are oversized, which requires a more thorough investigation. Figure 7.13 shows the distribution of fuel mass exclusively for the single X19039000-01 allocation. A large portion of the missions allocated with this thruster require less than 25% of the fuel capacity available. However, an alternative is hard to find, with the Standard MiPS being the lightest of the options presented in Figure 7.9 which still meet the status requirement as detailed in Section 7.2.2. Furthermore, it is to be expected that due to the allocation algorithm implemented, which always rounds up the fuel required to the next-largest fuel capacity, these concepts are significantly biased towards oversizing.

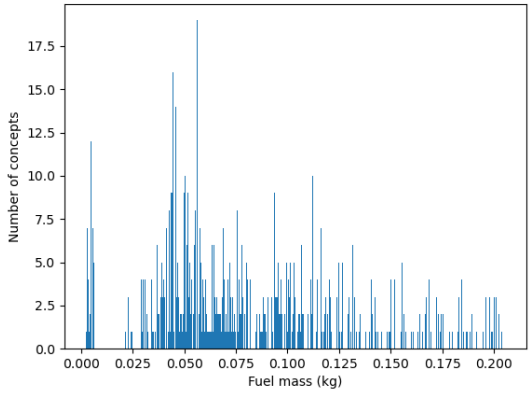

Figure 7.13: Distribution of the fuel mass for the single X19039000-01 allocation.

7.3. Remaining subsystems

The design of the key enabling subsystems is the focus of the thesis project. However, in order to verify the system as a whole, and ensure that its subsystems are also adaptable, each subsystem should be considered and evaluated. In an effort to limit the scope of the project, these subsystems are modelled after those outfitted onboard the original MASCOT mission unless explicitly indicated. Due to the limited mass and volume constraining MASCOT's design, most of these subsystems are relatively sparse compared to what would be typically present in a conventional spacecraft.

A distinction is made between environment- and payload-driven subsystems. Environment-driven subsystems, namely the structural, thermal, and guidance, navigation, and control subsystems, are sized based on the lander, impact, and SSSB characteristics. On the other hand payload-driven subsystems, namely the command and data handling, power generation, and communication subsystems are highly dependent on the scientific payload, as this drives the power required, data rate, and required processing power. Therefore, payload-driven subsystems are designed with a much lower degree of confidence, and detail, and are considered mission-dependent.

7.3.1. Structure

Rather than solid material plates forming its rectangular prism shape, such as those typically seen in satellites; MASCOT's structure follows a framework design. This design is implemented as a mass-optimized solution where the in-plane strength of CFRP is used for structural stiffness and adequate force distribution.

The main forces exerted on the structure are the preload used to secure the lander in place, and the impact. The preload is exerted on the frame through an attachment point. In order to distribute the preload through the structure, a set of diagonal beams make up a truss about the attachment location. The structure can be seen in Figure 7.14. Furthermore, a foam core is placed within the CFRP beams, making up a sandwich construction. Overall, this results in a lightweight design which provides additional impact dampening capabilities, which in fact would be sufficient for a number of SSSBs as detailed in Chapter 6 [86].

A middle wall separates two compartments, highlighted in red and yellow in Figure 7.14, with the yellow volume being available as payload. This wall is used to further distribute the preload, as well as providing for attachment points for the payload. The top (bottom in Figure 7.14) surface in the frame design has no beams. This is due to this surface being used for a thermal radiator [86].

MASCOT's structure, while tailored for its mission, is a highly replicable and adaptable design. The

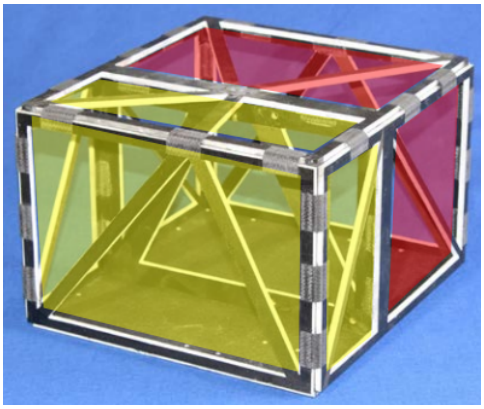

Figure 7.14: MASCOT's structure (from Lange et al. [86]).

placement of the middle wall would be the only parameter that would vary between iterations based on the subsystem and payload placement.

7.3.2. Thermal control

Thermal control can be a very complex subsystem to design and size. As showcased in Figure 7.15 it is highly dependent not only on the SSSB target itself, but also on the landing location. However, passive thermal control systems, provided that the day/night cycle of the SSSB and the payload requirements allow their use, are extremely versatile. For active operations, MASCOT makes use of a main passive radiator coupled with multi-layer insulation blankets, which limit heat transfer between subsystems and for the lander as a whole. Additionally, in order to regulate battery temperature while on-board Hayabusa-2, MASCOT is embedded with a smaller secondary active heater, which is only active pre-deployment.

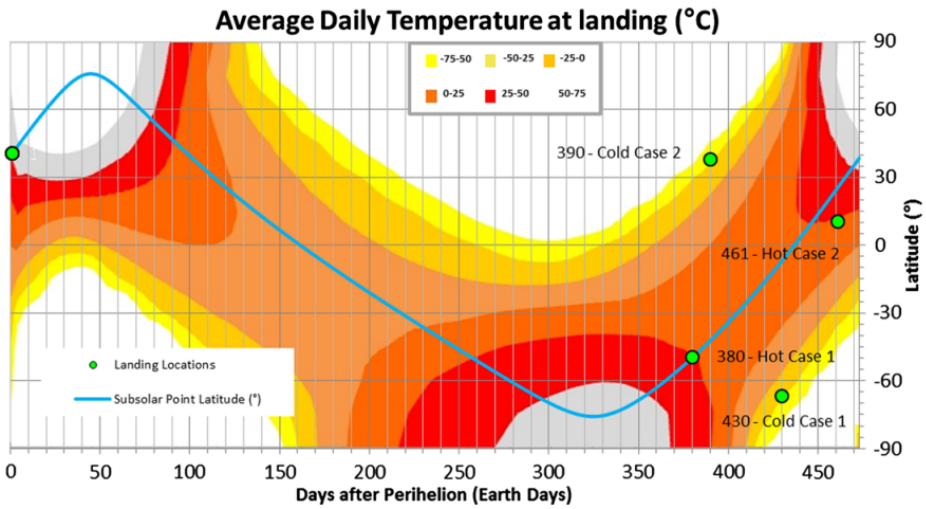

Figure 7.15: Seasonal variation of the latitudinal daily average temperature in Asteroid (162173) 1999 JU3 (from Grundmann et al. [16]).

The structural middle wall discussed in Section 7.3.1 is not only present for structural reasons. It separates the lander's payload into 'warm' and 'cold' compartments, housing the electronics and payload respectively. This design allows for good inter-component thermal insulation. Furthermore, a set of heat pipes connect the warm compartment to the main radiator, as this is the most thermally-dissipative system outfitted in the lander.

The main thermal control system implemented in MASCOT is highly adaptable, with the exception of the smaller active radiator, which is sized based on requirements from the electrical system. Grundmann et al. tested MASCOT's thermal values for the analyzed worst-case scenarios outlined in Figure 7.15, where these values never exceeded the acceptable limits [16]. Therefore we can conclude that the lander's operational range for average daily temperature without an enhanced thermal control system is 198-348 K.

7.3.3. Guidance, navigation, and control

In Chapter 5, design option trees were made splitting the key enabling technologies into active/passive, and orientation dependent/agnostic systems. This last distinction originated due to the specific adaptations required for a orientation dependent system, namely a flywheel.

Flywheels are mechanical systems used to store rotational energy via the principle of conservation of angular momentum. In spaceflight, they have been used for energy storage, as an alternative to batteries. However, their main use in space missions is attitude control, typically in a three- or four-wheel configuration such that full three-axis control can be achieved (with a possible redundancy) [87].

For the purpose of descent control, only a single flywheel is necessary, as it will store angular momentum in the plane parallel to the impact surface of the SSSB. This will allow for the lander to land pallet-first and therefore dampen the impact and suppress the rebound, via the key enabling subsystems, effectively.

Reaction wheels are sold commercially as COTS components. Grimm et al.'s lander design also necessitated the use of a flywheel. The reaction wheel selected for a 13 kg lander platform, is the CubeWheel Medium, providing 0.0108 Nms of momentum capacity [59] [82]. In the State-of-the-Art of Small Spacecraft Technology survey published by NASA, reaction wheels are included as part of the Guidance, navigation, and control section [82]. The relevant comparable reaction wheels are summarized in Table 7.5.

Table 7.5: Flywheel comparison (raw data from State-of-the-Art of Small Spacecraft Technology survey [82])).

Model	Mass [kg]	Peak Power [W]	Momentum Capacity [Nms]	Mass efficiency [Nms/kg]	Power efficiency [Nms/W]
CubeWheel Medium	0.150	2.3	0.0108	0.072	0.005
RWP015	0.130	1	0.015	0.115	0.015
RW-0.01	0.120	1.05	0.018	0.150	0.017
RWO	0.137	3.25	0.020	0.146	0.006

It is clear from Table 7.5 that among the current state-of-the-art, the CubeWheel Medium is actually the worst performer, having the lowest mass and power efficiencies (calculated using momentum capacity). The RW-0.01, manufactured by Sinclair Interplanetary, is the lightest reaction wheel while still generating the second largest momentum at the second lowest power requirement. Therefore, it is the clear winner, and thus the chosen flywheel for the lander design.

Following the discussion in Section 7.2.3, it was determined that an accelerometer will be required to trigger the firing sequence of the rebound suppression mechanism. For this selection, the State-of-the-Art of Small Spacecraft Technology survey was also used. The survey lists 96 different inertial sensors, which include gyroscopes, accelerometers, Inertial Reference Units (IRUs), and Inertial Measurement Units (IMUs). IRUs and IMUs are integrated components where IRUs are made up of sets of gyroscopes, and IMUs consist of a combination of accelerometers and gyroscopes. Furthermore, IRUs and IMUs, may be equipped with barometers and magnetometers, none of which are relevant for the trigger of the firing sequence [82].

The set of inertial sensors was evaluated using mass as the main criterion, as the deceleration impact should be significant enough that any of the accelerometers considered should reliably sense it. All IRUs and gyroscopes listed were filtered-out, leaving a remainder of 66 inertial sensors. Among the remaining options, IMUs were prioritized, due to the additional data generated, which could be used for scientific measurements. The lightest among these is the NavChip™ Series 3 Precision 6-Axis

MEMS Inertial Measurement Unit developed by Thales, in particular the class A option due to its lower acceleration bias [82].

MASCOT is an uncontrolled lander except for its mobility mechanism; therefore, it is relatively sparse in terms of guidance, navigation, and control systems. It is equipped with five optical position sensors and six photo-electric cells. Both of these sets of sensors are used to determine MASCOT's attitude, with the photo-electric cells being used for redundancy. The optical position sensors are made up of an infrared LED and a photo-diode couple, which, when given the command to switch on, can detect the presence of a surface via the reflected light of the LED. These sensors are very lightweight and can be simply integrated in the lander design [88].

7.3.4. Payload-driven subsystems

The design of the command and data handling, power generation, and communication subsystems is highly dependent on the on-board scientific payload. Therefore, any effort to size these systems before the payload is settled upon will be wasted. Instead, general guiding philosophies for the design of these systems can be provided.

The design of the communication subsystem is primarily determined based on the mothership's own communication subsystem, as any scientific data sent to Earth must be relayed by the mothership. Therefore, this will be the main determinant for the radio frequency band used. Orbital height of the mothership will determine the required power of the signal due to free-space losses; with the payload determining the required data rate. Due to the limited volume on-board the lander, a deployable antenna would be a great addition for the lander design. Optimally, redundancies should be implemented in the design of the communications system, as it is a critical subsystem.

The command and data handling subsystem is also considered a mission-critical subsystem. For this reason, implementing redundancies should also be heavily considered in the design of this subsystem. The only predefined capabilities that this subsystem must carry out in the lander are the detachment from the mothership, the activation and deactivation of the reaction wheel, and the trigger sensing and consequent firing of the thruster. All of the remaining functions of the system are related to the payload, and the communications and power management subsystems.

One of the main limitations of MASCOT's design is its short lifespan. Equipped only with a primary battery and no means of generating power, the lander could only gather useful scientific for a period of 16 hours. Optimally, the lander should be equipped with both secondary batteries and a power generation system which, provided it could generate enough power, would extend the mission's lifetime until the mothership went out of range, the lander system failed, or no more valuable scientific data could be obtained. Power should be generated via solar cells, distributed along the free surfaces of the lander. Additional mechanisms could also be added for a deployable solar array, further extending the power generating area. It is important to note that for each SSSB target, multiple factors would significantly affect power generation, mainly the rotational period of the SSSB and the distance to the Sun.

7.4. Scientific payload

The main purpose of a SSSB lander is to safely deliver a payload to the surface of the target SSSB, as well as supplying adequate power for its operation. As the objective of this thesis project is the development of a lander able to visit a wide range of SSSBs, it should also be able to accommodate a large number of payload systems. For this purpose, a list of possible payloads that the SSSB lander may house is showcased in Table 7.6.

Table 7.6: Possible payloads onboard the SSSB lander (adapted from Lange et al. [46]).

Instrument	Mass [kg]	Peak Power [W]	Avg Power [W]	Duty cycle [%]	Data volume [Mbyte]	Heritage
Stereo/PanCam	0.8	3.4	0.0017	0.05		PanCAM (MER, ExoMars)
Multi-Spectral Camera	0.41	6.4	1.8		2.1	MASCAM (MASCOT)
Instrumented Mole	0.9	3.5				HP3 (Insight)
MicroSeismometer	0.3	0.2	0.2	100		
Alpha-Particle X-ray Spectrometer	0.64	1.5	1.5	5	7.5	APXS(Philae)
Raman Spectrometer	1.22	12.7	12.7	3	0.34	ExoMars
Mossbauer Spectrometer	0.5	3	2	10	0.15	MIMOSII
Attenuated Total Reflectance spectrometer, optical microscope and thermal sensor	0.2	1.2	0.036	3	7.88	
Evolved Volatiles Ion Trap Analyzer	0.6	6	3		1.25	
Ion Laser Mass Analyzer	2.5	13.5	9	1	0.5	
Laser-induced Breakdown Spectrometer	1.2	9	7			
X-ray Diffractometer	2	12	5.1	1	0.25	
Optical microscope and IR spectrometer	2		12	40		MMEGA (MASCOT)
Radiometer	0.196		0.31		20 bits/s	MARA (MASCOT)
Magnetometer	0.24		0.5		1010 bit/s	MASMAG (MASCOT)
NewConsert	1.8	10			2	Consert

Instrument	Science goal
Stereo/PanCam	Multi-spectral geological mapping of landing site and surrounding
Multi-Spectral Camera	Multi-spectral geological mapping
Instrumented Mole	Subsurface science: depth resolved measurement of mechanical and thermal soil properties
MicroSeismometer	Surface layering, regolith processes, global body constitution
Alpha-Particle X-ray Spectrometer	Elemental composition heavier than C, elemental abundances
Raman Spectrometer	Identify mineralogical, inorganic and organic composition
Mossbauer Spectrometer	Fe mineralogy, mineral types
Attenuated Total Reflectance spectrometer, optical microscope and thermal sensor	Volatiles, mineral species, chemistry, texture, water
Evolved Volatiles Ion Trap Analyzer	Detect ionized evolved gases and activity
Ion Laser Mass Analyzer	Composition of solid and volatile samples: elements, molecules (mineral and organic) and isotopes
Laser-induced Breakdown Spectrometer	Elemental composition
X-ray Diffractometer	Mineralogy, organics, ices, hydrated/aqueous process, elemental composition
Optical microscope and IR spectrometer	Determine soil facies and structure, microscopic compositional heterogeneity wrt to mineralogy
Radiometer	Surface brightness temperature, surface inertia and spectral slope in the IR
Magnetometer	Magnetic field profile, global and local magnetiza tion
NewConsert	Internal structure, 3D tomography
Mobility mechanism	Allow for the exploration of multiple sites within an SSSB

7.5. Lander layout configuration

In order to ensure that all components fit within the enclosure of the lander, a mock-up of the lander was designed using *CATIAv5*. A render of the design showcasing its key enabling systems can be seen in Figure 7.16 and Figure 7.17

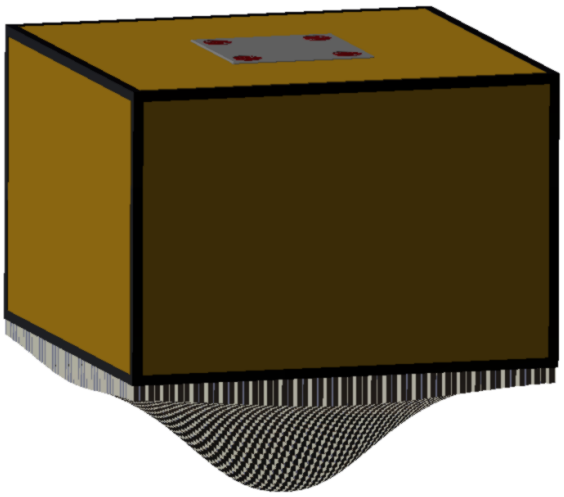

Figure 7.16: Render of the lander concept.

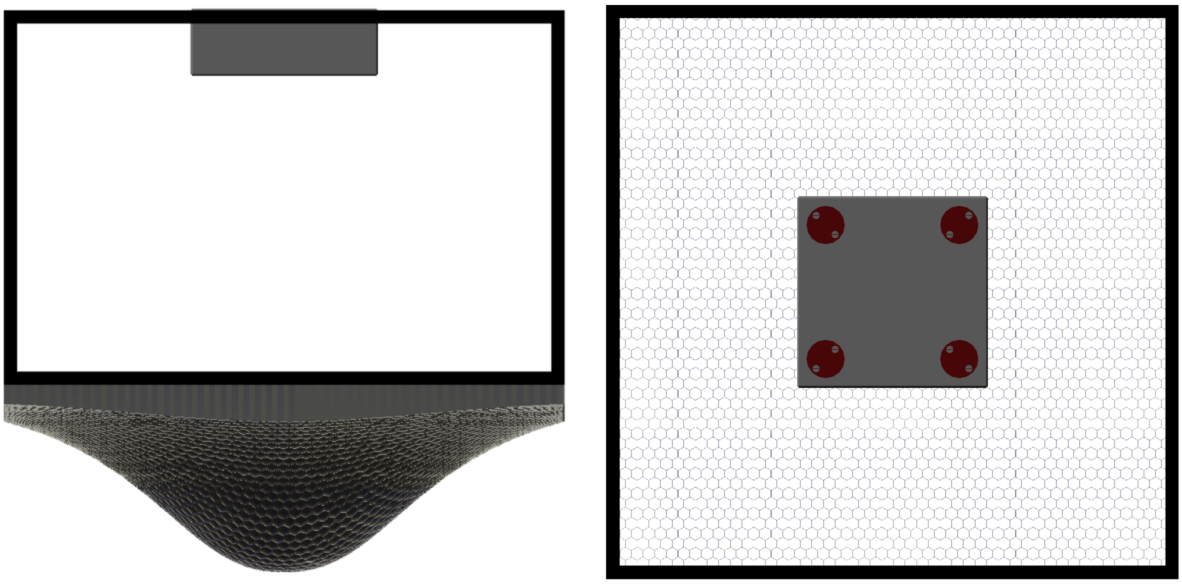

Figure 7.17: Renders of the lander concept without panels, front (left) and top view (right).

The key enabling subsystems, pallet and thruster, were modelled using the most commonly allocated configurations as discussed in Section 7.1.4 and Section 7.2.5. The pallet must be attached outside of the main lander body, as it is the only part which should come in contact with the SSSB surface. On the other hand, most of the thruster's volume is enclosed by the body of the lander, with only its top surface protruding from the insulating panels. This positioning follows the guidelines set by VACCO. Overall, this design results in minimal use of the body of the lander, allowing for most of the payload and subsystems to be housed there.

7.6. Scalability of key enabling systems

Adaptability is the main driving philosophy taken into account when carrying out the conceptual design of the lander. A truly adaptable concept should be also be scalable; allowing for larger and smaller payloads to be launched using the same conceptual design in a different scale.

In order to assess the scalability of the key enabling systems, the full design iteration, from the simulation in Chapter 6 to the pallet and thruster sizing in Section 7.1.4 and Section 7.2.5 has to be repeated. Due to the implementation of MBSE in the design, these ”models” are linked, and therefore, the relevant scripts must simply iterate over a range of masses, with minimal changes implemented. Furthermore, this analysis serves as a sensitivity study for the mass and volume of the lander, the constraining parameters used as part of the CDE paradigm used in the design.

While the implementation of this analysis throughout the relevant scripts is relatively simple, computational expense is an important consideration, particularly considering the need for redundant simulations to address the issues described in Chapter 6. Therefore, rather than using a linear scale for the scalability analysis, the lander mass is iterated using a logarithmic scale of base ten, with the mass indexes ranging from 0 to 4 in steps of 0.25. Effectively this results in a study that assesses the viability of the lander in a mass range of 1-10,000 kg. In order to further reduce the computational expense of this analysis, rather than repeating the simulations tenfold, a triple modular redundancy approach has been used, with three repetitions of each simulation and for each SSSB removing the simulation that was in non-agreement with the remaining two.

For each individual SSSB simulation, and consequent pallet and thruster allocation, an evaluation is made on whether the key enabling subsystems manage to both dampen the impact and suppress the rebound. If both the pallet and thruster succeed, the ”mission” is naturally considered a success. Another possibility is that even after dampening the impact and firing the thruster, the remaining velocity of the lander is below the SSSB’s escape velocity, thus remaining within the SSSB’s sphere of influence, but still experiencing a rebound. This, as discussed in Section 4.7, will make the location and orientation of the lander unpredictable; although these issues could be solved with the addition of a mobility mechanism as discussed in Section 5.4. If that scenario takes place, the mission is evaluated as a partial success. Lastly, the mission is marked as a failure if the remaining velocity exceeds the SSSB’s escape velocity, thus missing the target. The results of the scalability analysis can be seen in Figure 7.18.

As expected, the lander has issues with scalability; particularly when exceeding a total mass of 100 kg (index of 2), where the success rate drops from 95.28%, to 87.06% with a mass of 118 kg (index of 2.25). From then, the decline in mission success rate is obvious, with a relatively steady decline until a success rate of 5.37% is reached at a mass of 3162 kg (index of 3.5), where it begins to stabilize. Furthermore, the maximum success rate takes place for a mass of 10 kg (index of 1) with a total success rate of 99.19%. This is a very positive sign, as the lander was designed with this size in mind. This implies that the correct approach was taken towards the sizing of the lander and the design of the relevant subsystems.

Scalability should not only be evaluated from a mission success perspective, but also at the key enabling subsystem ”cost” to the mission, which is effectively its mass. The results of this study are displayed in Figure 7.19. Here the thruster mass is dominant, with relatively low panel masses. As expected, the mass efficiency of the key enabling systems increases exponentially with increasing mass index. When analyzing Figure 7.18 and Figure 7.19 together, it can be observed that the optimal size for these subsystems, in terms of mission success and mass, is for a total mass of 100 kg (index of 2). Here, the mass efficiency begins to settle around a value of 2.5% of the total mass, just before the drop in mission success rate.

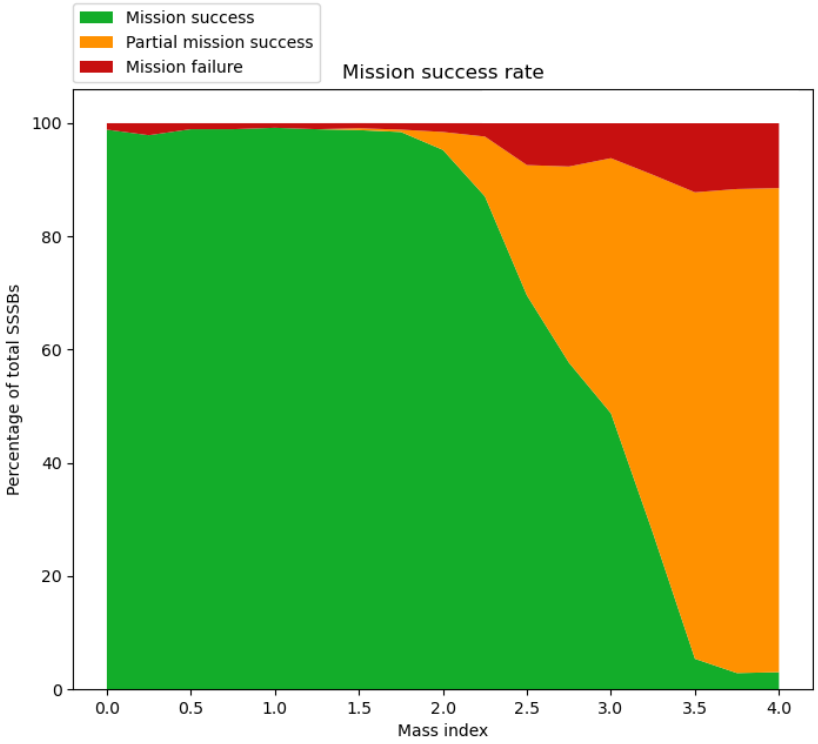

Figure 7.18: Stack plot of mission success rate with varying mass index.

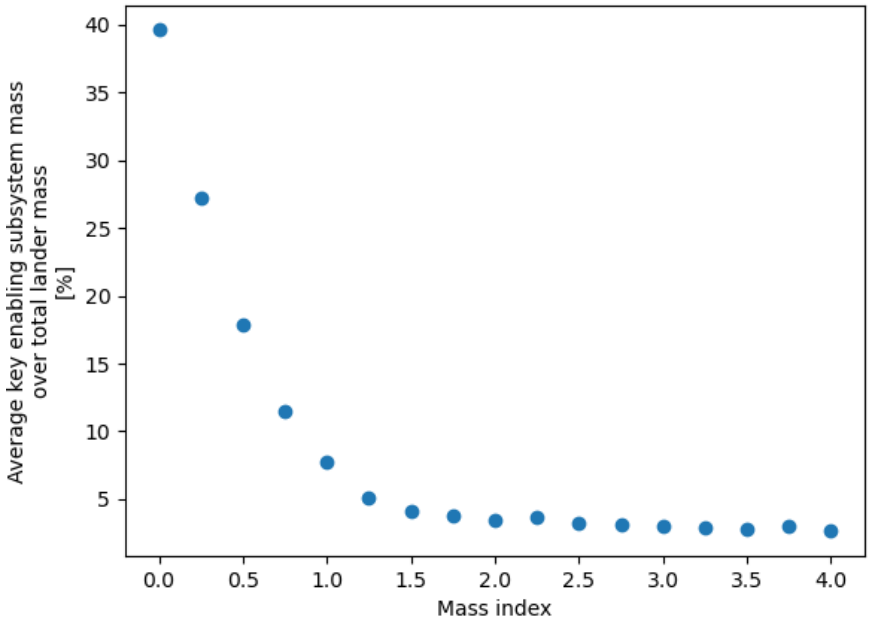

Figure 7.19: Average key enabling subsystem mass ratio with varying mass index.

8

Verification

Verification is fundamental in any engineering project; ensuring that the design meets the set requirements, and any methods used to generate results are implemented properly, thereby outputting correct results.

In the space industry, verification for space systems has been standardized by the ECSS; in particular, guidelines on verification are provided in handbook *ECSS-E-HB-10-02A*. Here, the verification process follows a three-pronged approach, with its objectives being:

- ”To demonstrate the qualification of design and performance, as meeting the specified requirements at the specified levels;”
- ”To ensure that the product is in agreement with the qualified design, is free from workmanship defects and acceptable for use;”
- ”To confirm product integrity and performance at particular steps of the project life cycle (e.g. launch, commissioning, mission events and landing).”

as defined by handbook *ECSS-E-HB-10-02A* [89]. While the fist and second points are achievable within the context of a conceptual design, the third point clearly falls outside of the scope of the thesis project, as its implementation requires the system to be evaluated at different stages of the project, preferably through testing.

The adaptable lander’s design follows the CDE approach, as detailed in Section 2.1. Therefore, the number of requirements that must be verified is low relative to most space systems projects, with the majority being functional or system requirements rather than specific performance parameters. These requirements were based on the original requirement diagram derived for the preliminary system model in Figure 2.5. The requirement verification table is displayed in Table 8.1. Here, levels of refinement are indicated with the ”>” sign, with the compliance, reasoning and source for each requirement being also provided. The ”FuncReq” and ”SysReq” nomenclature for functional and system requirements is instead replace by ”FR” and ”SR” for readability.

The initial constraints can also be evaluated. These constraints were volume- and mass-related, with an assumed envelope of 6U, and a mass in the order of 10 kg, following MASCOT’s design. While the full mass and volume of the lander can not be estimated due to the lack of a specific target, the ranges as calculated in Section 7.1.4 and Section 7.2.5 can be assessed.

With regards to mass, the pallet system falls well within the order of magnitude of a subsystem for a 10 kg lander. The large majority of pallets weigh below 0.05 kg, with a significant concentration in the 0.05 to 0.3 kg region. There are only a number of pallets exceeding 0.5 kg, with a maximum mass of

Table 8.1: Requirement verification table.

Requirement	Compliance	Reasoning	Source
FR_1	Partial	The lander remains on the surface across a majority of the SSSBs in the database	Figure 7.18
> FR_1.1	Compliant	All simulations assumed this deployment scenario	Chapter 6
> > SR_1	Not-verified	The push-off mechanism is considered a Mothership system, therefore not sized	-
> FR_1.2	Partial	An appropriate maximum deployment height was calculated for each SSSB	Figure 6.4
> > SR_2	Not-verified	Active descent control was only implemented for planar stability (flywheel)	Section 7.3.3
> SR_3	Partial	The lander remains on the surface across a majority of the SSSBs in the database	Figure 7.18
FR_2	Partial	The lander remains operational across a majority of the SSSBs in the database	Table 7.2
> FR_2.1	Partial	Specific payloads were not implemented, payloads studied should remain operational	Table 7.6
> > SR_4	Partial	The pallet's shock absorption capabilities satisfy a majority of the SSSBs in the database	Table 7.2
> SR_5	Partial	The lander's orientation is assured across most of the SSSBs in the database	Table 7.4
FR_3	Partial	The lander is operational across a majority of the SSSBs in the database	Table 7.2
> FR_3.1	Compliant	Several configurations of the key enabling systems are embedded in the design	Table 7.2, Table 7.4
> FR_3.2	Compliant	All configurations of the key enabling systems satisfy more than one SSSB	Table 7.2, Table 7.4

4.14 kg being a extreme outlier. On the other hand the large majority of thruster masses do not exceed 2.5 kg, with most being below 1.5 kg, and with a very small number of large outliers between 4.5 and 6 kg. On-board the original MASCOT mission, the total mass available for payload was 4.2 kg [14]. Therefore, the addition of theses subsystems still falls within a reasonable order of magnitude.

The volume constraint of 6U is clearly violated by the implementation of the pallet design. However, this is necessary in order to reduce the shock experienced by the payload, with a shorter column length leading to a larger shock. However, due to a combination of the variable column length, and the mass optimization carried out on the pallet, the actual volume of the system is significantly lower than the 12U that would be assumed from adding a 100 mm long pallet to the bottom of the lander. The thruster, on the other hand, perfectly complies with the volume requirements set, with the large majority of the thruster allocated being the smallest available size. A few outliers result in relatively large volumes with the allocation of dual thrusters.

In order to ensure that the thesis project is ”free from workmanship defects and acceptable for use” [89], the validity of the results reached has been assessed in a number of ways, with comparisons made to similar subsystems and sensitivity analyses conducted at different stages. All systems engineering methodologies employed followed the relevant standards as closely as possible, in particular INCOSE's definition of MBSE presented in Section 2.2 [18].The JPL database, detailed in Section 5.1 and used throughout the report, originates from NASA, the world leader in space exploration [61]. The concepts for the key enabling subsystems detailed in Chapter 5 were obtained from a number of qualified contrasting sources from literature. Both the killer requirement and the criteria weights presented in Section 5.6 and Section 5.7.2, were evaluated using sensitivity analyses. The simulations showcased in Chapter 6, were carried out using a reliable toolbox in Tudat which has been used in a number of published scientific papers[72]. Furthermore, the settings used for the simulation were evaluated and chosen using a number of sources from the literature gathered in Chapter 4. The detailed design of the lander, presented in Chapter 7 makes use of a number of COTS components; here, manufacturer's data was used as the only source and assumed to be reliable. Lastly, as detailed previously, this verification process itself followed ECSS standards set in handbook *ECSS-E-HB-10-02A* [89].

Validation is also a key procedure that must be carried out in any finalized project, ensuring that the customer's needs are satisfied by the product. In order to carry out the validation process, extensive discussions with customers must be held. According to handbook *ECSS-E-HB-10-02A*, validation is not mandated if the suitability of the product to fulfil its intended use is addressed by the system's requirements. However, it still allows for validation to be carried out if it is considered appropriate [89]. The aforementioned functional requirements were specifically set in order to ensure that the system fulfilled its needs. Therefore, a dedicated validation process falls outside of the scope of the project.

9

Conclusion

The goal of this thesis project was to answer the main research question:

What is a suitable design for an adaptable SSSB lander platform able to deliver a surface payload in a range of different operating environments?

In order to analyze the current state-of-the-art in SSSB landing platforms, research was conducted on all existing missions that have been carried out in the past. These missions have found mixed success with some of the landers succeeding, others never deploying, and others achieving partial success. After analysis of the current state-of-the-art, an opportunity for a new lander system was found, aiming to bridge the high reliability of MASCOT with Philae's extensive functionality and high-altitude deployment ability.

To help answer the main research question four sub-questions were drawn up. The first sub-question aimed to investigate which systems engineering methodology is best suited for the design of an adaptable SSSB lander. In order to allow for high adaptability in the design, an agile systems engineering methodology is required. Model-based systems engineering (MBSE) was selected due to its agile and structured concept development and iteration, as well as its heritage in the MASCOT lander mission. Following the standards for MBSE, a number of diagrams were created using SysML based on a theoretical lander concept. These diagrams included the block definition diagrams for both mothership and lander, as well as the requirements, use-case, and sequence diagrams. The MBSE methodology was not only used to generate these diagrams, but embedded in the different design phases of the project to enable agile iteration. Furthermore, a CDE approach was selected for the design of the lander based on MASCOT's volume and mass.

The second sub-question focused on investigating the range of possible operating environments for the SSSB lander. Following an in-depth study of SSSBs, and the approach and landing phases, the operational environment of the lander was fully defined. This included the analysis of the most relevant factors affecting the lander mission and its success. Furthermore, various modelling techniques for the different phases of the mission were analyzed and discussed. It was concluded that the key enabling systems for SSSB lander are an impact dampening and a rebound suppression subsystem.

In order to determine the answer to the third sub-question: *"Which are the optimal key enabling subsystems for a SSSB lander?"*, a number of suitable options were gathered for each of these subsystems from literature. These subsystems were then grouped, based on whether its use required control over the lander's orientation, using design option trees; these groupings were then expanded into 32 different concepts. To reduce the number of concepts to be evaluated a reliability-based killer requirement was introduced. In order to assess this a parameter was devised, which takes several factors into account in order to estimate the operational reliability of the concepts. Together with a minimum threshold,

and weighted criteria, the application of the killer requirement resulted in 15 concepts passing the filter. Furthermore, a sensitivity analysis was conducted on the effect of the different criteria weights and the minimum threshold in order to ensure a reliable output. The remaining concepts were then assessed on a number of criteria, namely: mass, operational range and reliability, adaptability, positional assurance and TRL. These criteria were weighted, where the weights were determined using the AHP. The winning concept combines a honeycomb pallet for impact dampening and a thruster for the rebound suppression. A further sensitivity analysis was conducted on the criteria weights in order to ensure the reliability of the results. Here, the previously selected concept consistently received the highest score.

Following the concept selection, numerical astrodynamics simulations were carried out using the software toolbox Tudat. Initially, the simulation was carried out for a single SSSB from a predefined deployment height. The script was then adapted such that the deployment height increased with every iteration, resulting in the maximum deployment height at which the lander would reach the SSSB surface with an uncontrolled approach, and the corresponding impact velocity. The script was then further extended to iterate over every SSSB in the database. Then, the results for maximum deployment height and consequent impact velocity were added to the database, such that they could be used to size the key enabling subsystems.

Once the relevant data was generated through the simulations, the sizing and allocation of the key enabling subsystems was made possible. This provides the answer for the final sub-question: *"How can the key enabling systems be adapted to extend the range of operating environments?"*. In order to reduce costs, increase system reliability, work with reliable data, and reduce the overall design effort a decision was made to integrate as many COTS components as possible in the detailed design. For the impact dampening subsystem the pallet's honeycomb is made up of aluminium alloys 5052 and 5056, with a standard hexagonal cell shape. Furthermore, pre-crushing is carried out in order to reduce the shock to the payload, and a mass optimization procedure is carried out for its shape. Based on the available COTS honeycomb cell sizes, an allocation procedure was carried out for each specific SSSB landing. This resulted in 19 different honeycomb configurations, each servicing a number of SSSBs. A cold gas thruster was selected as the thruster type; this was done to mitigate the lower reliability of an active rebound suppression subsystem, due to their relative simplicity and flight heritage. Specifically, the Standard MiPS by VACCO was selected, following an evaluation of the current state-of-the-art cold gas thrusters with flight heritage. The Standard MiPS features a modular design, and can therefore be easily adapted for each SSSB landing; furthermore, it is a fully integrated system, implements several redundancies, and features a complete data sheet. Additionally, a firing sequence trigger system for the thruster was outlined, complete with redundancies. Following that, an allocation procedure similar to that of the pallet, was carried out, resulting in 6 different configurations, with two of them employing two sets of thrusters. Overall, the pallet/lander configuration was found to service 99.19% of the SSSBs in the database. The remaining subsystems were then outlined, with a distinction made between those which are mostly payload-driven. A number of sample payloads was further provided, with the key enabling systems being presented in a CAD model.

A scalability analysis of the key enabling subsystems was also conducted. Here, the simulations and subsystem allocation were repeated for a range of masses. The results were conclusive, with the mission success percentage dropping significantly with a lander mass larger than 100 kg. On the other hand, the key enabling subsystems were increasingly mass-effective with larger lander mass, as expected. Overall a ”sweet spot” was found at the 100 kg lander mass, with high mission success rate at relatively low key enabling subsystem mass.

Lastly, the verification of requirements and constraints was outlined. The requirements were mostly found to be partially compliant, with the initial expectations being too ambitious or with some subsystems not being required. The mass constraints were on-par with the expected values of the original MASCOT mission, however the volume constraint was violated by the impact dampening subsystem.

10

Recommendations

The true in-depth design of a SSSB lander is a process that would take years of development for an experienced, multidisciplinary, team of engineers. Consequently, the work carried out in this thesis project is, by nature, incomplete and with a number of significant limitations. Therefore, specific shortcomings of the thesis project are outlined, addressed with relevant recommendations.

In Section 2.3, a preliminary system model was defined based on the initial expectation of the systems making up the lander. For this purpose, a number of system diagrams were included; but as detailed in Figure 2.2, these are only a fraction of all system models implemented in MBSE. Furthermore, the level of detail in these diagrams could be significantly improved. Therefore, future work in the systems engineering approach could involve the full definition and implementation of these diagrams following the MBSE standards.

The database presented in Section 5.1 was scrapped from a very reliable source in NASA. However, the number of bodies with the required parameters is but a fraction of the total number of SSSBs. Therefore, further investigations could be conducted on the expansion of this database, in order to have a more complete picture of the actual number of SSSBs that the different concept variants fulfill.

As detailed in Chapter 6 and Section 7.6, a number of simulations were carried out for each SSSB with varying lander masses. These simulations used spherical harmonics for the modelling of the SSSBs' gravitational field. As discussed in Section 4.2.1, the polyhedron model is superior in terms of truncation errors, convergence, and built-in collision detection. Future studies could aim to implement this gravitational field model to the simulations, and Tudat as a whole. Furthermore, the cold gas thruster used for rebound suppression could also be used for active decent control, extending the maximum deployment height and increasing the degree of certainty of the landing zone. Efforts should be directed into modelling this thruster acceleration, which could be solved as an optimization problem with Tudat, which has extensive documentation for this purpose.

Lastly, dedicated validation is not within the scope of the thesis project. However, investigations and experiments on the performance of both the key enabling subsystems should be carried out, ensuring that they perform adequately. For the impact dampening subsystem, this would involve testing the crush performance of the honeycomb, particularly with irregular impacts as described in Section 4.6. For the cold gas thruster both its firing sequence, and the rebound suppression effectiveness should be effectively modelled and tested. These systems, when embedded on a lander platform would also have to undergo the relevant integration testing. Further integration requirements with the mothership and launcher vehicle should also be evaluated.

References

[1] IAU. *RESOLUTION B5 Definition of a Planet in the Solar System*. IAU, Aug. 2006. URL: https://www.iau.org/static/resolutions/Resolution_GA26-5-6.pdf.

[2] Shane D Ross. “Near-earth asteroid mining”. In: *Space* (2001), pp. 1–24.

[3] David W Dunham et al. “Implementation of the first asteroid landing”. In: *Icarus* 159.2 (2002), pp. 433–438.

[4] Tetsuo Yoshimitsu, Takashi Kubota, and Ichiro Nakatani. “MINERVA rover which became a small artificial solar satellite”. In: *Proceedings of the Small Satellite Conference* (2006).

[5] J-P Bibring et al. “The ROSETTA lander (“PHILAE”) investigations”. In: *Space science reviews* 128.1 (2007), pp. 205–220.

[6] Tamás Baranyai, András Balázs, and Péter L Várkonyi. “Partial reconstruction of the rotational motion of Philae spacecraft during its landing on comet 67P/Churyumov-Gerasimenko”. In: *arXiv preprint, arXiv:1604.04414* (2016).

[7] Hermann Boehnhardt et al. “The Philae lander mission and science overview”. In: *Philosophical Transactions of the Royal Society A: Mathematical, Physical and Engineering Sciences* 375.2097 (2017), p. 20160248.

[8] Tetsuo Yoshimitsu, Takashi Kubota, Atsushi Tomiki, et al. “Current status and future plan of MINERVA-II rovers onboard Hayabusa2”. In: 2016.

[9] JAXA. *Hayabusa2 Information Fact Sheet*. 2018.

[10] Yuichi Tsuda et al. “Hayabusa2 mission status: Landing, roving and cratering on asteroid Ryugu”. In: *Acta Astronautica* 171 (2020), pp. 42–54.

[11] James Richard Wertz and Wiley J Larson. *Reducing space mission cost*. Microcosm Press Torrance, CA, 1996.

[12] ESA. *ExoMars suspended*. 2022. URL: https://www.esa.int/Newsroom/Press_Releases/ExoMars_suspended.

[13] Walter F Huebner et al. “A comprehensive program for countermeasures against potentially hazardous objects (PHOs)”. In: *Solar System Research* 43.4 (2009), pp. 334–342.

[14] Canhui Yin et al. “Technical progress in landing mechanisms for exploring small solar system bodies”. In: *Progress in Aerospace Sciences* 122 (2021), p. 100697.

[15] Jan Thimo Grundmann et al. “Small spacecraft in small solar system body applications”. In: *2017 IEEE Aerospace Conference*. IEEE. 2017, pp. 1–20.

[16] Jan Thimo Grundmann et al. “Mobile Asteroid Surface Scout (MASCOT)-Design, Development and Delivery of a Small Asteroid Lander Aboard Hayabusa2”. In: *IAA proceedings on-line-http://pdc. iaaweb. org/? q= ipc* (2015).

[17] Jan Thimo Grundmann et al. “One shot to an asteroid-mascot and the design of an exclusively primary battery powered small spacecraft in hardware design examples and operations considerations”. In: *ESA Special Publication* 719 (2014), p. 66.

[18] Sanford Friedenthal, Regina Griego, and Mark Sampson. *INCOSE Model Based Systems Engineering (MBSE) Initiative*. Jan. 2009.

[19] Ana Luísa Ramos, José Vasconcelos Ferreira, and Jaume Barceló. “Model-Based Systems Engineering: An Emerging Approach for Modern Systems”. In: *IEEE Transactions on Systems, Man, and Cybernetics, Part C (Applications and Reviews)* 42.1 (2012), pp. 101–111. DOI: 10.1109/TSMCC.2011.2106495.

[20] Emmanuel Ogunshile et al. “Application of model based systems engineering for an asteroid lander”. In: *Proceedings of the International Astronautical Congress, IAC*. Vol. 10. International Astronautical Federation. 2012, pp. 8445–8453.

[21] Michael Kretzenbacher et al. “Model Based Systems Engineering (MBSE) applied through a sysML model to the mascot asteroid lander”. In: *International Astronautical Congress (IAC) 2013*. International Astronautical Federation, IAF. 2013, pp. 8015–8022.

[22] Caroline Lange, Christian Ziach, and Tra-Mi Ho. “A model-based systems engineering approach to design generic system platforms and manage system variants applied to MASCOT follow-on missions”. In: *66th International Astronautical Congress* (2015).

[23] Daniele Gianni, Andrea D’Ambrogio, and Andreas Tolk. *Modeling and simulation-based systems engineering handbook*. CRC Press, 2014.

[24] Jochen Ludewig. “Models in software engineering–an introduction”. In: *Software and Systems Modeling* 2.1 (2003), pp. 5–14.

[25] SysML Partners. *SysML Open Source Project - What is SysML? Who created it?* 2022. URL: https://sysml.org/.

[26] Daniel Hestroffer et al. “Small solar system bodies as granular systems”. In: *EPJ Web of Conferences*. Vol. 140. EDP Sciences. 2017, p. 14011.

[27] Yang Yu. *Orbital dynamics in the gravitational field of small bodies*. Springer, 2016.

[28] David James Tholen. “Asteroid taxonomy from cluster analysis of photometry”. PhD thesis. The University of Arizona, 1984.

[29] Schelte J Bus and Richard P Binzel. “Phase II of the small main-belt asteroid spectroscopic survey: A feature-based taxonomy”. In: *Icarus* 158.1 (2002), pp. 146–177.

[30] George A Krasinsky et al. “Hidden mass in the asteroid belt”. In: *Icarus* 158.1 (2002), pp. 98–105.

[31] Paul R Weissman and Stephen C Lowry. “Structure and density of cometary nuclei”. In: *Meteoritics & Planetary Science* 43.6 (2008), pp. 1033–1047.

[32] Tatsuhiro Michikami and Axel Hagermann. “Boulder sizes and shapes on asteroids: A comparative study of Eros, Itokawa and Ryugu”. In: *Icarus* 357 (2021), p. 114282.

[33] Aaron Clauset, Cosma Rohilla Shalizi, and Mark EJ Newman. “Power-law distributions in empirical data”. In: *SIAM review* 51.4 (2009), pp. 661–703.

[34] Jennifer A. Grier and Andrew S. Rivkin. “Chapter 7 - The Creation of Regolith and Soils—Impact Cratering and Other Processes”. In: *Airless Bodies of the Inner Solar System*. Ed. by Jennifer A. Grier and Andrew S. Rivkin. Elsevier, 2019, pp. 143–164. ISBN: 978-0-12-809279-8. DOI: https://doi.org/10.1016/B978-0-12-809279-8.00007-X. URL: https://www.sciencedirect.com/science/article/pii/B978012809279800007X.

[35] Michael E Zolensky et al. “Physical, chemical, and petrological characteristics of chondritic materials and their relationships to small solar system bodies”. In: *Primitive Meteorites and Asteroids*. Elsevier, 2018, pp. 59–204.

[36] Dominique Bockelée-Morvan et al. “The composition of cometary volatiles”. In: *Comets Ii* 1 (2004), pp. 391–423.

[37] Jennifer A. Grier and Andrew S. Rivkin. “Chapter 10 - Volatiles: Origin and Transport”. In: *Airless Bodies of the Inner Solar System*. Ed. by Jennifer A. Grier and Andrew S. Rivkin. Elsevier, 2019, pp. 199–227. ISBN: 978-0-12-809279-8. DOI: https://doi.org/10.1016/B978-0-12-809279-8.00010-X. URL: https://www.sciencedirect.com/science/article/pii/B9780128092798000010X.

[38] Koji Wada et al. “Asteroid Ryugu before the Hayabusa2 encounter”. In: *Progress in Earth and Planetary Science* 5.1 (2018), pp. 1–30.

[39] Jens Biele et al. “The landing (s) of Philae and inferences about comet surface mechanical properties”. In: *Science* 349.6247 (2015).

[40] Jens Biele et al. “Experimental determination of the structural coefficient of restitution of a bouncing asteroid lander”. In: *arXiv preprint arXiv:1705.00701* (2017).

[41] Colin Thornton and Zemin Ning. “A theoretical model for the stick/bounce behaviour of adhesive, elastic-plastic spheres”. In: *Powder technology* 99.2 (1998), pp. 154–162.

[42] Daniel J Scheeres et al. “Scaling forces to asteroid surfaces: The role of cohesion”. In: *Icarus* 210.2 (2010), pp. 968–984.

[43] Dan T Britt et al. “Asteroid density, porosity, and structure”. In: (2003).

[44] Antonio Castellanos. “The relationship between attractive interparticle forces and bulk behaviour in dry and uncharged fine powders”. In: *Advances in physics* 54.4 (2005), pp. 263–376.

[45] K Rietema. *The dynamics of fine powders*. Springer Science & Business Media, 2012.

[46] Caroline Lange et al. “Exploring small bodies: Nano-and microlander options derived from the Mobile Asteroid Surface Scout”. In: *Advances in Space Research* 62.8 (2018), pp. 2055–2083.

[47] Christian Grimm et al. “The MASCOT Separation Mechanism-A Reliable, Low-Mass Deployment System for Nano-Spacecraft”. In: *CEAS Space Journal* 12 (2020), pp. 343–365.

[48] California Polytechnic State University The CubeSat Program. *Poly Picosatellite Orbital Deployer Mk. III Rev. E User Guide*. 2014.

[49] Planetary Systems Corporation. “2000785G MkII MLB User Manual”. In: (2018).

[50] Pablo Muñoz et al. “Rosetta navigation during lander delivery phase and reconstruction of Philae descent trajectory and rebound”. In: (2015).

[51] C Dietze et al. “Landing and mobility concept for the small asteroid lander MASCOT on asteroid 1999 JU3”. In: *61st International Astronautical Congress* (2010).

[52] Robert A Werner and Daniel J Scheeres. “Exterior gravitation of a polyhedron derived and compared with harmonic and mascon gravitation representations of asteroid 4769 Castalia”. In: *Celestial Mechanics and Dynamical Astronomy* 65.3 (1996), pp. 313–344.

[53] Robert A Werner. “The gravitational potential of a homogeneous polyhedron or don’t cut corners”. In: *Celestial Mechanics and Dynamical Astronomy* 59.3 (1994), pp. 253–278.

[54] Gregory L Light. “An introductory note on relative derivative and proportionality”. In: *International Journal of Contemporary Mathematical Sciences* 1.7 (2006), pp. 327–332.

[55] MohammadAmin AlandiHallaj and Nima Assadian. “Soft landing on an irregular shape asteroid using Multiple-Horizon Multiple-Model Predictive Control”. In: *Acta Astronautica* 140 (2017), pp. 225–234.

[56] Philip Heinisch et al. “Reconstruction of the flight and attitude of Rosetta’s lander Philae”. In: *Acta Astronautica* 140 (2017), pp. 509–516.

[57] Douglas J Rodgers et al. “Methodology for finding and evaluating safe landing sites on small bodies”. In: *Planetary and Space Science* 134 (2016), pp. 71–81.

[58] Silvio Schröder, Christian D Grimm, and Lars Witte. “A crushable shell for small body landers”. In: *CEAS Space Journal* 12.1 (2020), pp. 65–72.

[59] Christian D Grimm et al. “Size matters-The shell lander concept for exploring medium-size airless bodies”. In: *Acta Astronautica* 173 (2020), pp. 91–110.

[60] ESA. *ESA Science Technology - Technology Readiness Level (TRL)*. 2020. URL: `https://sci.esa.int/web/sci-ft/-/50124-technology-readiness-level`.

[61] NASA. *Solar System Dynamics JPL*. 2022. URL: `https://ssd.jpl.nasa.gov/`.

[62] Benoit Carry. “Density of asteroids”. In: *Planetary and Space Science* 73.1 (2012), pp. 98–118.

[63] D Pellegrinetti et al. “ExoMars 2016-Flight dynamics operations for the targeting of the Schiaparelli module entry descent and landing and the trace gas orbiter mars orbit insertion”. In: *AIAC18: 18th Australian International Aerospace Congress (2019): HUMS-11th Defence Science and Technology (DST) International Conference on Health and Usage Monitoring (HUMS 2019): ISSFD-27th International Symposium on Space Flight Dynamics (ISSFD)*. Engineers Australia, Royal Aeronautical Society. 2019, p. 1377.

[64] Shota Kikuchi et al. “Ballistic deployment of the Hayabusa2 artificial landmarks in the microgravity environment of Ryugu”. In: *Icarus* 358 (2021), p. 114220.

[65] H Lin, G Leisk, and B Trimmer. “Soft robots in space: a perspective for soft robotics”. In: *Acta Futura* 6 (2013), pp. 69–79.

[66] Thomas Djursing. *ESA skrev til danske raketbyggere om eksplosiv-problem på Philae | Ingeniøren*. 2014. URL: https://ing.dk/artikel/esa-skrev-til-danske-raketbyggere-om-eksplosiv-problem-paa-philae-172274.

[67] Aaron Parness et al. “Gravity-independent mobility and drilling on natural rock using microspines”. In: *2012 IEEE International Conference on Robotics and Automation*. IEEE. 2012, pp. 3437–3442.

[68] Claudio Bombardelli, Michael Broschart, and Carlo Menon. “Bio-inspired landing and attachment system for miniaturised surface modules”. In: *Proceedings 58th International Astronautical Congress*. 2007.

[69] Daniel R King et al. “Creating gecko-like adhesives for “real world” surfaces”. In: *Advanced Materials* 26.25 (2014), pp. 4345–4351.

[70] Liehui Ge et al. “Carbon nanotube-based synthetic gecko tapes”. In: *Proceedings of the National Academy of Sciences* 104.26 (2007), pp. 10792–10795.

[71] Thomas L Saaty. “What is the analytic hierarchy process?” In: *Mathematical models for decision support*. Springer, 1988, pp. 109–121.

[72] Tudat Space. *Tudat Space — tudat.space 0.3.1 documentation*. 2022. URL: https://docs.tudat.space/en/stable/.

[73] NASA. *SPICE Toolkit*. 2022. URL: https://naif.jpl.nasa.gov/naif/toolkit.html.

[74] Toshihiro Kubo-oka and Arata Sengoku. “Solar radiation pressure model for the relay satellite of SELENE”. In: *Earth, planets and space* 51.9 (1999), pp. 979–986.

[75] Erwin Fehlberg. *Classical fifth-, sixth-, seventh-, and eighth-order Runge-Kutta formulas with stepsize control*. National Aeronautics and Space Administration, 1968.

[76] HexWeb. “HexWeb ® CR III Corrosion Resistant Specification Grade Aluminum Honeycomb”. In: (2017). URL: https://www.hexcel.com/user_area/content_media/raw/HexWeb_CRIII_DataSheet.pdf.

[77] HexCel. “HexWeb ® Honeycomb Selector Guide”. In: (2017). URL: https://www.hexcel.com/user_area/content_media/raw/HexWeb_SelectorGuide_2017.pdf.

[78] HexCel. “HexWeb ® Honeycomb Selector Guide”. In: (2017). URL: https://www.hexcel.com/user_area/content_media/raw/HexWeb_SelectorGuide_2017.pdf.

[79] Björn Zakrisson. “Numerical simulations of blast loaded steel plates for improved vehicle protection”. PhD thesis. Luleå tekniska universitet, 2013.

[80] Yongqing Wang et al. “Surface quality improvement in machining an aluminum honeycomb by ice fixation”. In: *Chinese journal of mechanical engineering* 33.1 (2020), pp. 1–8.

[81] Jody Singer, Joseph Pelfrey, and George Norris. “Secondary Payload Opportunities on NASA’s Space Launch System (SLS) Enable Science and Deep Space Exploration”. In: *Space Operations: Contributions from the Global Community*. Springer, 2017, pp. 207–220.

[82] Bruce Yost et al. *State-of-the-art small spacecraft technology*. 2021.

[83] VACCO. *A Standard Micro Propulsion System for CubeSats*. 2020. URL: http://mstl.atl.calpoly.edu/~workshop/archive/2020/Spring/6%20-%20Subsystems/ChrisDay.pdf.

[84] Stefano Casini et al. “Towards the Use of Commercialoff-the-Shelf Small-Satellite Components for Deep-Space CubeSats: a Feasibility and Performance Analysis”. In: *SmallSat 2020-34th Small Satellite Conference*. 2020.

[85] VACCO. “Standard Propulsion System”. In: (2020). URL: https://cubesat-propulsion.com/wp-content/uploads/2020/04/Standard-MiPS-datasheet-042120.pdf.

[86] M Lange et al. “MASCOT-A Lightweight Multi-Purpose Lander Platform”. In: *EUROPEAN CONFERENCE ON SPACECRAFT STRUCTURES, MATERIALS AND ENVIRONMENTAL TESTING 2012* (2012).

[87] Vit Babuska et al. “A review of technology developments in flywheel attitude control and energy transmission systems”. In: *2004 IEEE Aerospace Conference Proceedings (IEEE Cat. No. 04TH8720)*. Vol. 4. IEEE. 2004, pp. 2784–2800.

[88] Federico Cordero. “MASCOT lander operational concept and its autonomy, general services and resource optimisation implementation in the on-board software”. In: *14th International Conference on Space Operations*. 2016, p. 2386.

[89] ECSS. *Handbook ECSS-E-HB-10-02A*. 2010.